# SUBCELLULAR LIGHT ACTIVATION, CONTROL AND MANIPULATION USING A DYNAMICALLY RECONFIGURABLE NANOPATTERNING SYSTEM

by

AMRUTA RAJIV JOSHI

Presented to the Faculty of the Graduate School of

The University of Texas at Arlington

And

The University of Texas at Southwestern Medical Center at Dallas

in Partial Fulfillment of the Requirements for

the Degree of

MASTER OF SCIENCE IN BIOMEDICAL ENGINEERING

THE UNIVERSITY OF TEXAS AT ARLINGTON

August 2008

I dedicate this thesis to the loving memory of my grandmother Aaji, who sadly passed away during the course of my thesis work.

ACKNOWLEDGEMENTS

I wish to take this opportunity to express my gratitude to all individuals who have helped me during this thesis work. I would like to thank my supervising professor Dr. Harold 'Skip' Garner, for being an extremely inspiring and encouraging mentor and providing me with invaluable advice in the course of my graduate degree. Special thanks to Dr. Michael Huebschman for his suggestions and insights into this project and for being a great friend, someone I could discuss any dilemma with.

I am extremely grateful to Dr. Hanli Liu and Dr. Jian Yang for their interest in my research work and for accepting the invitation to be my committee members. I also express my sincere gratitude to Dr. Danielle Miller, who taught me the basics of tissue culture, to Linda and Kay for all the administrative help and friendly encouragement they have showered me with, and to all the members of the Garner lab.

I also wish to thank my friend Rahul who has proofread my thesis and helped in every possible way in order for me to complete this thesis.

And most importantly, I am indebted to my family my parents Aai and Baba, and my brother Rahul dada, who have always been there for me. I would not have made it this far without their help, encouragement and support throughout my life. Thank you dada, for being my role model and my greatest pillar of support.

July 11, 2008

# ABSTRACT

## SUBCELLULAR LIGHT ACTIVATION, CONTROL AND MANIPULATION USING A DYNAMICALLY RECONFIGURABLE NANOPATTERNING SYSTEM

Amruta Joshi, M.S.

The University of Texas at Arlington, 2008

Supervising Professor: Dr. Harold “Skip” Garner

Cellular communication is the basis of all cellular activities and functions. Cell signaling is crucial in the processes of tissue maintenance, tissue development and homeostasis. Errors in transmission or interpretation of these signals can result in the onset of diseases like cancer. Efforts have been made to probe into the communication between cells, and the extracellular signals that cells transmit to each other. There is however, a necessity to understand cell communication within the cellular components themselves and to be able to perform a nanoscale analysis of the cell organelle behavior. Many cellular mechanisms involve processes at the subcellular level, and many disorders too, are organelle specific. Cell interaction with submicron structures in the cell has not been well understood due to a lack of methods to achieve precise submicron

resolution cell patterning, control and probing. Therefore an organelle level perturbation apparatus will be a boon to the investigation of how organelle specific disorders occur.

We constructed a nanopatterning system, as an application of nanotechnology to biology, born out of the need to study nanoscale subcellular events and manipulate individual cell organelles. This system is a photoactivated perturbation apparatus that allows for submicron control of the cell machinery. The Digital Micromirror Device from Texas Instruments coupled with an epifluorescence microscope, form the major components of this nanopatterning system. Ultraviolet light was directed to fall on the DMD surface, which generated digital light masks to specifically illuminate the cell organelles while not illuminating others and vice versa. This system thus enables photoactivated subcellular and localized control of the cell machinery.

This thesis work presents the design, optimization and characterization of the nanopatterning array system used to demonstrate the varying sensitivity of individual cell components to ultraviolet light. The desired environmental conditions, optimum dye concentrations used and the system resolution are discussed. Experiments investigating the severity of damage caused within a human fibroblast cell in response to local cytoplasm and local nucleus UVA irradiation, and a relation between these damage sites are then described. Our data demonstrates that the cell cytoplasm is about three times more sensitive to UVA damage than the cell nucleus. Experiments involving UVA light illumination of only the cytoplasmic membrane cause the fibroblast cells to sense and avoid the UV illumination by retracting their body from the site of

illumination. The average cytoplasmic membrane retraction velocity ranges from about 2.6 μm/min to 9.3 μm/min for a UVA intensity of 3.6mW/cm$^2$.

Our nanopatterning system provides new avenues for light activated organelle specific treatments for cases that call for localized targets. This technique can aid research in the treatment of diseases, in which the functions of an intracellular organelle are impaired and also those disorders in which interorganelle communication is defective.

TABLE OF CONTENTS

LIST OF ILLUSTRATIONS

LIST OF TABLES

LIST OF ABBREVIATIONS

UV…….....Ultraviolet

UVR.....Ultraviolet Radiation

UVA……...Ultraviolet A, long wave

UVB……Ultraviolet B, medium wave

UVC……Ultraviolet C, short wave

DLP……Digital Light Processing

DMD……...Digital Micromirror Device

DMEM…….……Dulbecco's Modified Eagle Medium

ECM……Extracellular Matrix

FBS…….…….……Fetal Bovine Serum

DAPI……..……..4',6-diamidino-2-phenylindole

PI……..……Propidium Iodide

RT……..…..….Room Temperature

$LD_{50}$…….....Median Lethal Dose

NADH…….. Reduced Nicotinamide adenine dinucleotide

NADPH…….Nicotinamide adenine dinucleotide phosphate

# CHAPTER 1

# INTRODUCTION AND BACKGROUND

Over the past few decades, cell organization and cell behavior to mimic tissue function have been widely researched as important aspects of tissue engineering. Placing groups of cells on biocompatible scaffolds and polymers in order to transform them into functional tissue structures requires a complete understanding of biochemical processes that determine parameters like the cell shape, function and viability. These biochemical processes are also fundamental for wound healing, normal cellular activity and tissue maintenance. Cell adhesion, cellular and sub cellular communication, as well as interaction between cells, organelles and the extra cellular matrix (ECM) are examples of such biological processes [1-4]. We require profound knowledge of how cells interact, with each other and with external signals in order for us to exercise spatial control over cells [5]. This would lead us to a better understanding of organ function and enable us to engineer organs that mimic natural organs.

## 1.1 Cell communication

Cellular communication is the basis of all cellular activities and functions. Cell communication involves transmission and receipt of cellular signals, and a desired response from the recipient cell. Accurate cell signaling is critical to normal tissue maintenance and homeostasis. Errors in transmission or interpretation of these signals

can significantly alter the cell function resulting in the onset of diseases like cancer and diabetes [6, 7]**.** There are two types of cell communication, intercellular communication and intracellular communication.

### *1.1.1 Intercellular communication*

Intercellular communication is the exchange of information between two or more cells, to regulate patterns of cell growth and differentiation. When a cell transmits signaling molecules, recipient cells receive this information through a class of proteins known as receptors. Although most of these receptors sit on the surface of the cell membrane, some are found inside cells. Receptor ligands, molecules that activate receptors, bind to the correct receptor for that signal, and render signal transduction complete. The entire set of cell changes induced by receptor activation is called a signal transduction pathway [7].

In some cases, cell to cell communication requires a direct cell-cell contact. This is called juxtacrine signaling and allows for very precise cell differentiation. Others form gap junctions to connect the cytoplasm of the two cells in order to communicate. Many cell signals are carried by molecules that are released by one cell and move to make contact with another cell. For example, endocrine hormones like estrogen, insulin, growth hormone, etc. are released by a cell and travel through blood to reach various target organs in the body. Another form of cell signaling is paracrine cell signaling, in which the target cell is in the local area as the signaling cell. Neurotransmitters are an example of paracrine hormones. The autocrine signaling, as the name suggests, involves

secretion of hormones that bind to receptors on the very same cell that secreted it [7, 8]. Intercellular communication has been extensively studied and distinct clinical fields like endocrinology have emerged from these studies.

### *1.1.2 Intracellular communication*

Although the segregation of cell structures into distinct cell organelles has increased the efficiency of cell function, it has also generated the need for effective communication pathways between these organelles to ensure normal metabolic regulation in cells. Intracellular signaling between organelles is a key cellular process responding to the internal cellular environments in eukaryotic cells. This communication is mediated by the exchange of signals within the cytoplasm and also by the direct transfer of components via vesicular and non-vesicular transport [9]. Just as intercellular communication is essential for the cell's growth and function, efficient communication between the organelles inside the cell is required for the cell's own endurance.

A vast number of vital cell processes involve this organelle communication. Regulation of DNA repair and replication, cell cycle, RNA transcription, protein translation and trafficking form a subset of the many intracellular processes. Physical communication between organelles and other cytoplasmic components is capable of affecting cell shape and function. Conrad et al. [10] have discussed the role of microtubules in the movement of a certain protein caveolin from the golgi complex to the plasma membrane thus demonstrating effective interaction between cellular

organelles. The cross talk between the nucleus and mitochondria required for mitochondrial biogenesis is another example of organelle communication [11]. Intracellular communication is also observed between the endoplasmic reticulum and other cell organelles by means of inter-organelle membrane contact sites [12].

Although it is essential to investigate this type of cell communication, studies related to molecular mechanisms underlying this interorganelle signaling are still in their infancy and need to be characterized.

## 1.2 Why is having subcellular targeting capabilities becoming increasingly valuable?

Eukaryotic cells are approximately 10-100 microns in diameter [13]. A cell has numerous organelles and other components inside it that carry out various functions so that the cell, as a whole can function smoothly. The dimensions of these organelles and other subcellular components range from nanometers to a few microns [14].

Intracellular signaling processes lay the foundation for cell survival and in order to study these, an apparatus which achieves a nanoscale resolution to perturb organelles is essential. What is it inside the cell that we want to study? Why is it so important to achieve sub cellular patterning capabilities?

### *1.2.1 To probe into mechanisms of organelle specific diseases and target drugs at the organelle level*

Many organelle specific pathological processes play critical roles in clinical indications such as mitochondrial cardiac myopathy, lyosomal storage diseases and

peroxisomal diseases. In these cases, functions of a subcellular organelle are rendered defective [15]. Adequate understanding of organelle organization, biogenesis and interaction pathways is required for studying the mechanisms underlying their defective functioning [15]. Currently, there are no completely effective treatments for mitochondrial specific ailments owing to the lack of successful mitochondria specific drug delivery systems and subcellular perturbation and interrogation techniques [16].

Nano-drug delivery is a rapidly growing field and it has potential applications like organelle specific disease targeting. Nanoparticles are used as drug loading materials and are then targeted to the correct cellular components for drug delivery [17]. Recently, micellar nanocontainers have been investigated to achieve selective delivery of drugs at the subcellular level. However, very little information is available about the micelle-cell interactions due to the lack of appropriate tools and techniques to localize their action [18]. Localized subcellular targets for drug delivery can open up new prospects for organelle specific diseases. This could be exploited to improve the efficacy of a drug. The mechanism of drug action may change in a positive way, if an organelle level manipulation apparatus enabling thorough determination of the defective organelle interactions is developed.

### *1.2.2 To investigate the target of action of chemotherapeutic agents and other light activated drugs*

Cancer, simply put, is uncontrolled division of defective cells. These cancer cells are not only unable to repair themselves but are also incapable of destroying

themselves by apoptosis. Such defective cells keep dividing and form a tumor [19]. Various chemotherapeutic agents are used for selectively destroying such cells. However, the exact target of these is not very accurate. Many times, these drugs destroy the normal non diseased cells, in the proximity of the cancer cells or anywhere in the body. Cancer drugs therefore are known to have side effects like massive hair loss, where cells in the hair follicle are destroyed. There is an urgent need to investigate which part of the cancer cell do these drugs target and how do they do so. This research could improve the destruction of cancer cells relative to the normal cells due to chemotherapeutic drugs. For example, researchers have investigated drugs that treat neurological illnesses and identified specific proteins within the brain as the target sites for these drugs. Knowledge of the exact target sites of these drugs enabled resynthesis of these drugs with a few modifications such that they now showed high specificity to the target proteins with few side-effects [20].

*1.2.3 To perform partial cell studies and to study other subcellular mechanisms*

Metabolic processes in cells are catalysed by enzymes and these enzymes are present in the cytosol and other cell organelles. Extensive studies about such processes require a suitable targeting method. Proteins, too, are integral components of cell function and in many cellular mechanisms; proteins get localized in particular sites within the cell [21]. It is extremely critical to understand a protein's properties like structure and localization. If localized protein content could be mapped and targeted, it would be possible to modify properties of this protein location over other locations in

the same cell. For example, there are certain light activable ion channels in neurons that can be switched on or off, with an external light pulse [22, 23]. Thus, a sub cellular manipulation technique would be able to target and activate some of these channels in one cell while maintaining others in an inactive state. This can then lead to an external switch to start or stop the ion intake into the cell.

There are other potential partial cell studies; partial nucleus manipulation [24], analysis of chromosome orientation in nuclei [25], and investigating whether certain biomolecules from one part of a cell get recruited to repair other parts [26].

## 1.3 Current cell manipulation techniques

Although mechanisms by which cells convert changes in cell geometry into different biochemical responses are still unclear, the discovery that cells respond to forced changes in their shape and orientation [27], lays the foundation for cell manipulation. The ability to build cell-surface interactions and to exercise spatial control over cells is essential in order to mimic natural tissues [28]. Surface modification is the most popular technique used to create cell patterns on surfaces and consequently control cell adhesion [29]. Selective cell adhesion can not only be achieved before the cell seeding but cell control can also be exercised after the adherence of cells on a surface. Prominent techniques used to perturb cells and organelles after cell adhesion focus on either contact methods like microinjection of cells using micropipette needles or on non-contact methods like electric field stimulated micromanipulation, magnetic manipulation or optical manipulation to perturb

organelles and cells. Some of the major states of art biomanipulation techniques are discussed below.

### *1.3.1 Surface modification techniques*

Surface modification is used to create cell patterns, which allow selective adhesion of cells to the pattern specific surface and thereby achieve spatial control over cell adhesion [30]. Following are the most common approaches to surface modification.

#### 1.3.1.1 Lithographic techniques

Photolithography has been conventionally used to create small scale integrated circuit patterns on a silicon wafer, which are then used in semiconductor electronics. Many radiation sources have been used ranging from UV mercury lamps, lasers, electron beams, and X rays. Various researchers have studied the use of photolithography to pattern surfaces for the alignment of cells. In the work by Revzin et al. [28], glass substrates were surface-modified and polyethylene glycol (PEG) hydrogel micropatterns were created using photolithography. More recently, other forms of lithography including immersion lithography and colloidal lithography are being used. Dalby et al. [31] cultured human fibroblast cells on nanocolumns produced by colloidal lithography techniques. This method utilized electostatically assembled monolayers of colloidal particles as masks for pattern transfer onto substrate materials [31].

Although photolithography as a form of light activated surface modification is capable of achieving high resolution and is already in use, a variety of other light

activated methods for cell patterning are popular. The prime reason for this is that photolithography is not feasible when numerous desired light patterns need to be projected in a short interval of time. It not only requires expensive chemicals and precise mask alignment, but it is also typically the most time consuming and labor intensive step.

#### 1.3.1.2 Inkjet printing

Inkjet printing is another surface modification technique and consists of depositing single, tightly-controlled microscopic droplets 10-100 micron in diameter onto a substrate. The drop-on-demand (DOD) printers eject single droplets on the substrate in response to a pressure impulse in the ink chamber. This pressure impulse is generated by a piezo-crystal that deforms in response to a voltage pulse, which in turn is computer controlled. Thus, by using appropriate software like computer aided design (CAD) packages, it is possible to fabricate desired patterns on the substrate [32, 33].

In another study by Roth et al [30], patterning of substrates was achieved using automated inkjet printing process. The entire substrate surface was coated with a cell repellent material. Collagen solution was introduced into the printer cartridge, and then used as the “ink” that was printed on the substrate surface to form collagen patterns on the substrate. Since collagen is a natural protein, it promotes specific attachment of cells in the collagen patterned regions thus achieving successful cell patterning [30]. Inkjet printing has the advantage that it creates a completely digital pattern which can be

stored and reprinted rapidly**.** However, it is capable of achieving a resolution of about 100 micron [34], which is not feasible for organelle level studies.

1.3.1.3 Photoactivated surface manipulation

These manipulation methods use light for the purposes of modifying the substrate. Use of light grants a precise and simple approach to targeting the surface of the substrate [35]. These techniques involve photochemically modifying the substrate properties so as to increase cell adhesion and achieve precise cell patterning. These methods have a clear advantage over conventional photolithography, since they need just one step light irradiation to cause a chemical change in the properties of the substrate [36]. Previously, Baac et al. [36] have used laser holographic methods to form cell culture substrates on photo-responsive azobenzene copolymers to achieve preferential adhesion of human astrocytes. Many other study groups also use UV or visible light polymerization techniques to pattern biomedical polymers. Another interesting method of using visible light photochemistry for cellular patterning by Luebke et al, describes the use of a digital micromirror array to obtain microscopic patterns of visible light on polyethylene glycol coated slides. They demonstrated selective cell adhesion on these slides in response to the light irradiation at a resolution of about 13 micron. Cell patterning by surface modification enables engineering applications like neural network organization [37], co-cultures of different cell types in vitro [38] and direct protein patterning for directed growth of cells [39]. However, since

most of these surface modification techniques cannot achieve a subcellular resolution; they cannot be used to facilitate organelle level studies.

### *1.3.2 Cell microinjection techniques*

Cell microinjection techniques usually involve the injection of a solution containing genes, proteins, DNA or fluorescent dyes into a cell through a glass capillary called the microneedle. The microinjection apparatus consists of a micropipette puller, an inverted microscope, a micromanipulator, and a microinjector. While the micropipette puller is required to fabricate consistent microinjection pipettes, the micromanipulator is needed to provide an interface between the microscope and the microinjector. The micromanipulator facilitates a smooth movement of the microinjector to target desired sites [40]. This technology has extensive applications including gene therapy, intracytoplasmic sperm injection (ICSI), *in vitro* fertilization (IVF), pronuclei DNA injections and other biomedical areas [41, 42]; but is very labor intensive thus low throughput. The delivery of the solution to a subcellular compartment may not always be precise due to the invasive nature of this technique.

### *1.3.3 Electric micromanipulation technique*

This technique is a non contact cell perturbation method and uses dielectrophoresis trap (DEP) and electrorotation phenomena to remotely manipulate suspended cells or particles**.** DEP involves the manipulation of dielectric particles using non uniform electric fields whereas electrorotation involves manipulation of electrically

polarizable objects like cells by controlling the phase and magnitude of electric fields [41].

This method involves modifying the charge of the DEP electrode tips to create electric field patterns. Cells can be guided to adhere in these patterned areas. This method has been used for the manipulation of many cell types as well as other biomolecules [43-45]. The work by Ho et al. [45], presents a design for a rapid liver cell patterning micro fluidic chip, which utilizes the dielectrophoresis (DEP) trap to build the pattern of liver cells. Stellate shaped electrode tips were used to apply radial electric field and thus create radial cell patterns. These radial patterns of live liver cells mimicked the lobular morphology of the real liver tissue. In a study brain functions by Prasad et al [46], gradient electric fields were set up using DEP and applied to a 5 x 5 microelectrode array system. Each microelectrode was 80 microns in diameter. Single neurons were then spatially positioned over these microelectrodes in order to map the changes in their electrical activity [46]. Lundqvist et al. [47] have devised a way to manipulate the content of cells and organelles based on electroporation of cell membranes by pulsed electric fields. Electroporation of cells and use of high voltage electric fields can, however, significantly reduce the survival time of the living cells and are not always desired.

### *1.3.4 Cell manipulation using magnetic principles*

Biomanipulation using magnetic forces can be used to study intracellular properties, determine mechanical properties of an individual cell, and separate certain

cells labeled with magnetic beads [41]. Micron sized magnetic particles can also be made to selectively attach to cells by the application of an external magnetic field for cell separation or purification [48]. In another technique for magnetic manipulation, Hultgren et al. [49] used ferromagnetic nickel nanowires to perform cell separation studies by magnetizing the nanowires parallel to their long axis and then releasing them into the cell culture. Sometimes, the magnetic particles are introduced into the cell via natural processes that do not involve forcible manipulation. For example [41, 50], the magnetic particles can be introduced into a living cell via endocytosis into preformed membrane compartments called magnetic endosomes. Under the influence of an external magnetic field, these endosomes can change their shape from circular to elliptical. The movement of magnetic endosomes guided by an external magnetic field within an individual cell can thus be achieved. Boukallel et al. [51] successfully manipulated a single DNA molecule magnetically by attaching one end of the molecule to a magnetic bead and immobilizing the other end of the molecule by attaching it to a surface like glass.

### *1.3.5 Optical biomanipulation*

Optical manipulation is a non invasive manipulation technique and involves the use of light to modify the properties, shape or the state of biomolecules. Light incident on a 'caged' compound can release it from its bound state and become active. Many studies [22, 23] have focused on stimulating photosensistive neurons with bursts of light

at different wavelengths while others have used masks to specifically target only desired cells [35].

1.3.5.1 Microbeam irradiation

One of the most commonly used methods of targeting subcellular components or certain selected cells, is the microbeam irradiation of the cells. Montgomery et al. [52] used an experimental setup consisting of an ultraviolet emitting scanner tube, a beam splitter and a 0.72 NA (Numerical Aperture) Polaroid grey reflecting objective to generate an ultraviolet microbeam at wavelengths from 240nm to 350nm and having a diameter of 0.5 micron. This microbeam was shaped to fit the cytoplasmic membrane of a liver cell and morphological changes in the membrane were observed as result of the UV irradiation. Similar microbeam apparatus based on the design by Uretz and Perry [53] was used by Zirkle et al. [54] to generate a focal hot spot of about 8 micron in diameter to irradiate the cell cytoplasm with ultraviolet light from 225nm to 300nm. Naruse et al. [24] studied partial nuclear irradiation in cells of eight animal species by producing microbeam spots of about 2 micron in diameter using this technique. In another approach for generating microbeams [55], a continuous wave argon-ion laser beam with a wavelength 514.5nm was passed through an ammonium dihydrogenphosphate (ADP) crystal to cause frequency doubling and to obtain a coherent continuous UV beam at 257.3nm. This UV beam was then transmitted through an irradiation microscope to a minimum spot diameter of 0.5micron to study the effect of UV light on the proliferation of Chinese hamster cells. It was found that the incident

energy required to cause a significant decrease in the cell proliferation was 30 to 60 times higher when the cell cytoplasm was specifically irradiated relative to the cell nucleus**.** Laser microbeam irradiation of the cell nucleus at 257nm was also used by Cremer et al. [25] to analyze the chromosome positions in the interphase nucleus. The diameter of the microbeam at the focal site was about 1-2micron. Many researchers use similar micromanipulation techniques to study the relative sensitivity of various cell organelles. Munro et al. [56] irradiated parts of Chinese Hamster cells with alpha particles using a polonium tipped microneedle and a 45X oil immersion objective at a resolution of 1-2micron in order to determine the relative radiosensitivity of the nucleus and the cytoplasm in those cells. Primary targets for alpha radiation induced cell death were found to be in the nucleus and the perinuclear region. Wu et al. [57] have demonstrated the induction of mutation in mammalian cells due to alpha particle irradiation of the cytoplasm by use of microbeams of almost 1micron diameter. Others investigated and demonstrated that chromosomes are the most sensitive targets for photodynamic therapy by employing submicron laser microbeams at 630nm to irradiate subcellular regions [58].

Such microirradiation techniques enable subcellular control equivalent to the spot diameter of the microbeam, however they have many disadvantages associated with them. In a microbeam experiment, the target is limited to the spot diameter and it is not possible to manipulate several organelles simultaneously. Also, the microbeam instrumentation does not provide a sharp boundary to the irradiated region and thereby does not offer accurate illumination of the desired components coupled with masking of

the rest of the components. In determining the biological effects of an organelle's local illumination, it is extremely critical to avoid illuminating any adjacent organelles. If a portion of the cytoplasm is targeted when trying to illuminate the nucleus, it would be impossible to correctly determine the effect of local nucleus illumination alone. Due to the lack of methods for accurately mapping randomly shaped subcellular components, a few study groups [57] have performed cytoplasmic irradiation by microirradiating two separate sites in the cell cytoplasm, each several microns away from the ends of the nucleus, to replace the whole cytoplasm irradiation.

1.3.5.2 Polycarbonate filter optical masking method

Many groups have used polycarbonate isopore membrane filters placed over the cells in a culture dish as irradiation masks to produce UV microbeams since this polycarbonate membrane does not transmit 254nm light. When UV light is incident on such a cell monolayer, portions of the cells that correspond to the location and the size of the filter pores are irradiated [26]. This method provides a resolution equal to the microfilter pore diameter and the most common pore sizes available are 3micron and 5micron [26]. This results in certain partially illuminated cell nuclei, which were used to investigate whether RNA synthesis from undamaged genes is affected by the presence of UV damage elsewhere in the same nucleus [59]. Katsumi et al. [26] have demonstrated that in normal cells, a certain nucleotide excision repair protein, PCNA, from the masked nuclear area gets recruited to the sites of DNA damage in the irradiated portion of the nucleus.

This method enables irradiation of a random confined area within individual cells and organelles but cannot be put to use when the requirement is to target whole organelles like the cytoplasm and the cytoplasmic membrane, which are much bigger than the membrane pore size and have distinct shapes that no membrane filter can selectively irradiate. Also, since some nuclei may always be partially masked, any study requiring targeting the entire nuclei would not be possible. Due to these limitations, this method of cell manipulation does not give the user sufficient control over the target of irradiation and cannot be used to compare organelle responses to the incident light.

## 1.4 The effects of UV radiation on biological material

Many optical biomanipulation techniques are used to study the cellular and organelle response to UV light, as described in section 1.3.5.

Ultraviolet light forms a part of the electromagnetic spectrum and ranges from approximately 200nm to 400nm. It has been categorized into subtypes depending on its wavelengths. These wavelength bands are referred to as UVA (315nm to 400nm), UVB (280nm -315nm) and UVC (200nm-280nm) radiation. UVA is the major component of the ultraviolet light from the sun reaching the earth's surface and accounts for about 95% of all the solar radiation while UVB only amounts to about 5% of it [60]. UVC is the most damaging of them all, but it never reaches the earth's surface because it is filtered out by the atmosphere's ozone layer. These subtypes of the UV radiation possess differential penetrative properties. UVA, UVB and UVC are shown to penetrate 30%, 10% and 1% respectively in a dermal layer of the skin [61].

Ultraviolet radiation can have beneficial as well as damaging effects on biological material.

### *1.4.1 Beneficial effects of UV radiation*

UVA has been extensively used in photodynamic therapy as a treatment for skin diseases like psoriasis, acne, vitiligo and erythema [62, 63]. This therapy involves the administration of an appropriate photosensitizer material to the patient followed by the illumination of the target area by a light of suitable wavelength. Excitation of the photosensitizer material results in formation of reactive oxygen species, (as discussed in 1.4.2.) causing the diseased cells to undergo apoptosis and die [62]. For example, psoralens is used as the photosensitizer in PUVA (Psoralens +UVA) therapies for the treatment of psoriasis [63]. As another example of the useful effect of UV radiation, a low dose of UVB is known to stimulate vitamin D production in the skin [64]. Vitamin D is one of the vital nutrients required for maintenance of calcium and phosphorous levels for bone formation in the body. No evidence is yet available as to the exact dose of UVB that would be low enough to produce vitamin D stimulation and not cause any harmful effects in the cells [62, 64].

### *1.4.2 Harmful effects of UV radiation*

UV radiation is long known to induce damage in tissue and cellular structures leading to several long term effects such as sunburn, photoaging, skin cancer and genetic mutations [60, 65-66]. There are two mechanisms of UV induced damage. The

first mechanism involves direct absorption of UV radiation (UVR) by cellular material resulting in chemical reactions that initiate apoptosis, by formation of photoadducts such as pyrimidine dimers, thymine dimers and cyclobutane pyrimidine dimmers. The second mechanism constitutes absorption of the UVR by means of a photosensitizer resulting in photosensitized reactions like generation of reactive oxygen species (ROS) causing oxidative damage [60, 65, 67-68]. Examples of the ROS are free radicals, singlet oxygen, superoxide radical anion, hydrogen peroxide etc [60, 67, 69]. These species cause uncontrolled oxidation of cellular material resulting in disrupting the redox equilibrium of the cell [64]. The photosensitizers can be endogenous or exogenous. For example, DNA in the cell nucleus is an endogenous chromophore and acts as a photosensitizer for UV radiation due to its absorption characteristics [65].

UVB induced damage is primarily mediated by the first mechanism of direct UVB absorption while the UVA induced damage occurs mainly due to its absorption by chromophores in the cell acting as photosensitizers [60, 66, 70]. It has also been established that UVA radiation induces an immediate apoptotic response in the target cells, while the UVB and the UVC induced delayed responses in cells [71-72]. At sufficiently high doses, UVB radiation is also hazardous to the eyes. Excessive exposure to UVB light is capable of causing eye conditions such as welder's flash, cataracts, pterygium, and degeneration of the macula in the retina [73-74].

## 1.5 Need for a dynamically reconfigurable subcellular biomanipulation technique

Many cell manipulation techniques have been devised; however, not all of these methods are capable of achieving a subcellular resolution. Although surface modification methods like photolithography and photoactivated surface manipulation can attain the subcellular scale, they need specialized infrastructure for their operation and can be very time consuming. The electric micromanipulation techniques can be automated for simple operation, but these cannot attain the high resolution required for accurate organelle level perturbation. Also, manipulation of cells using DEP and electrorotation involves applying an electric field to aqueous solutions and only suspended particles can be targeted [41]. Manipulation of cells by contact methods is a challenging task, as it requires not only a precise, controllable manipulator set-up but also a suitable end-effector which can be actuated to perform the desired tasks without damaging the cells. Cell manipulation using magnetic principles involves high power consumption and extended durations of manipulation can cause local heating, possibly damaging the cells, which is again not preferred [75]. Optical microbeam methods can target submicronal structures but do not employ any light masks to do selective local irradiation of cell portions or organelles. None of the optical methods provide any way to conform the light beam to irradiate organelles having arbitrary shapes. (E.g. the cell membrane). Other nanotechnology methods for subcellular patterning like micelle nanocontainers are under investigation and little is known about their capability to target specific organelles.

**There is a need for a biomanipulation technique that allows for simple operation, is non- toxic and capable of achieving a subcellular resolution, such that nanoscale analysis of cellular events can be accomplished. This technique should also have a provision to dynamically track and illuminate the target's position continuously and perform partial cell analysis of live cells in real-time.**

## 1.6 Research Problem and statement of the hypothesis

The primary goal of this thesis is to present the design, development and optimization of a dynamically reconfigurable nanopatterning system that successfully accomplishes individual organelle manipulation by light activation. The project also aims to provide a performance evaluation of the nanopatterning system by demonstrating subcellular scale patterns of ultraviolet light and studying the cellular response to such organelle specific illumination. **We hypothesize that the cell response to UVA radiation is dependent on the site of the illumination within the cell.** This thesis work aspires to observe and compare the difference in the cell survival rates when the UVA radiation is specifically targeted to the cell nucleus, and to the cell cytoplasm. It is also very important to investigate the targeted organelle's behavior, movement and cell to cell contact communication with neighboring counterparts in response to high resolution UVA illumination. Among these responsive behaviors is the characterization of the motion and the retraction velocity of the cytoplasmic membrane as a consequence of continuous ultraviolet light illumination incident on it. This project also aims to perform cell trapping studies to demonstrate the use of light to direct the movement of cells into

selected areas and also to alter their morphology establishing a foundation for advanced tissue engineering applications.

# CHAPTER 2

# MATERIALS AND METHODS

In the first section of this chapter, the design and development of instrumentation which forms the nanopatterning system is discussed with a detailed description of all its subsystems, components and specifications. This is followed by a description of the experimental conditions and the procedure for subcellular manipulation experiments, in the second section.

## 2.1 Nanopatterning system design

The nanopatterning system was constructed to enable real-time organelle level control over the cell. It employs the Digital Light Processing (DLP) technology devised by Texas Instruments to construct a digital mask for controlling illumination thereby giving us an ability to target specific areas inside a cell. It consists of a DLP based optical system coupled with an inverted epifluorescence microscope, the Olympus IX71. While the Digital Micromirror Device grants the capability to project “nano” or “micro” patterns, the epifluorescence microscope proves to be useful to observe, record and trace those “nano” changes in the cells in a real-time fashion and at the desired magnification.

A summary of the fundamental nanopatterning system specifications is given in Table 2.1 below. A detailed discussion of these system specifications is presented in chapter 3.

Table 2.1: List of Nanopatterning System specifications

| | |
|---|---|
| Pattern Size | 1024 pixels x 768 pixels |
| Optical Switching time between DMD frames<br><br>Mechanical Switching time between DMD frames | 2μsec<br><br>15μsec |
| Switching time between two patterns | 1-2 minutes* |
| Power Density | 0-3.65mW/cm$^2$ |
| System resolution | 0.45 ± 0.063 micron |
| Image Acquisition Resolution | 0.07micron |
| Input Wavelengths | 350-500nm |
| Sample Environment Control<br><br>• Temperature<br><br>• Blood Gas Flow rate | <br><br>22$^o$C-42$^o$C ± 1$^o$C<br><br>1200 ± 10cc/minute |

*Individual patterns were generated manually; future automated apparatus should enable sub-second time resolution.

The nanopatterning system is composed of four subsystems: the optical pathway, the epifluorescence microscope system, the environmental chamber and the image acquisition subsystem. The components of each subsystem are shown in the schematic and pictorial representation of the nanopatterning system depicted in Figure 2.1.

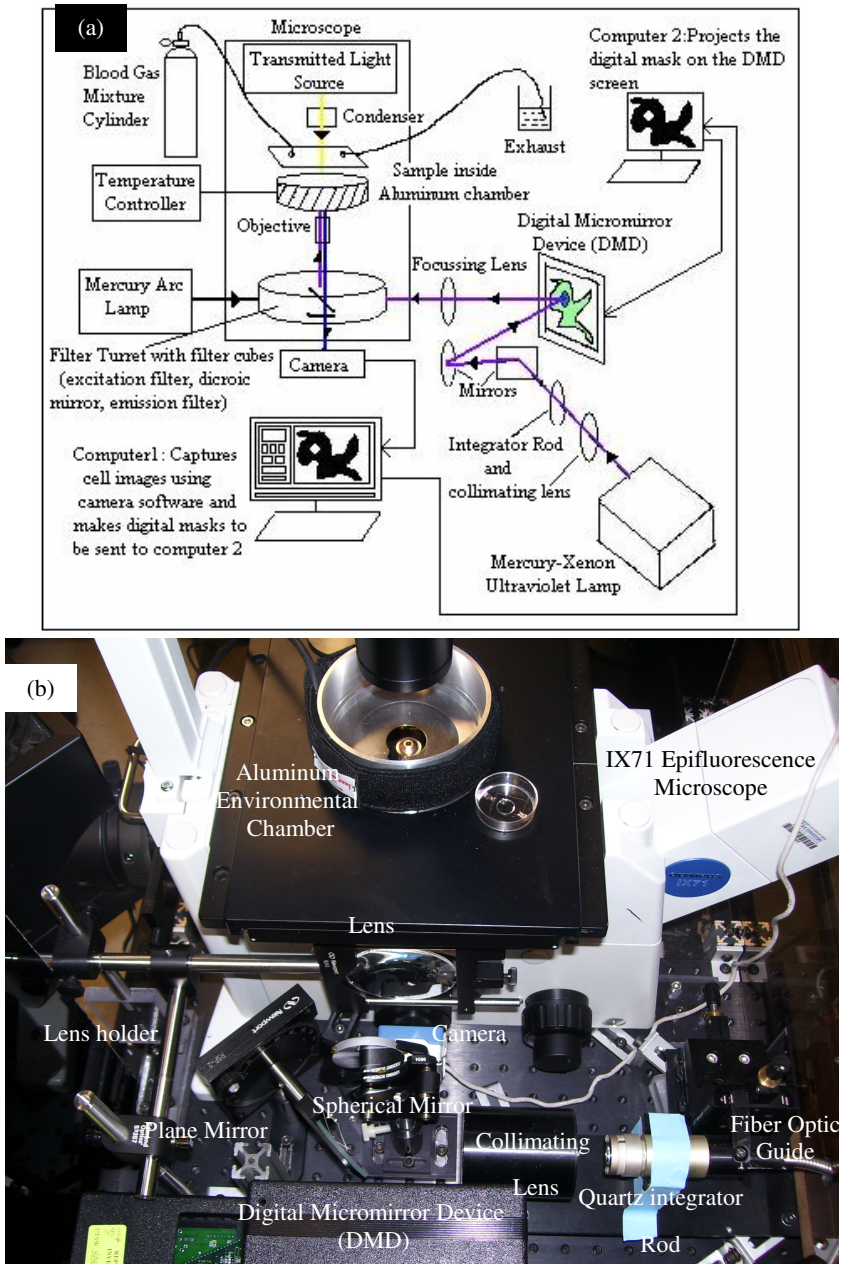


Figure 2.1: The Nanopatterning System Schematic Diagram. Figure (a) shows the schematic representation of the nanopatterning system. The two principal components are shown: the DLP based optical system and the epifluorescence microscope. A fiber optic guide passes the light from the UV lamp to an integrator rod, which relays it to the plane mirror. After reflecting from the plane and the spherical mirrors, the light is incident on the DMD screen. Depending on the pattern on the DMD screen, the now patterned light passes through a 15cm focal length double convex lens and hits the dicroic mirror of the modified U-MWU filter cube in the microscope filter turret. The patterned light is then reflected to hit the specimen. After the specimen fluorescences, the light passes through the emission filter and reaches the camera port. The specimen image is recorded by computer1 to create a digital mask of the target and this is sent to computer2. The DMD screen then projects the digital mask onto the selected filter cube. Also shown in figure is the second light source (mercury arc lamp), temperature and humidity control assembly. Pictorial representation of the nanopatterning system is seen in figure (b).

A detailed description of all the sub-systems is given below:

*2.1.1. The optical pathway*

The optical components that carry the ultraviolet light from the light source to the microscope form an integral part of the system. The exact positioning and orientations of these components is essential in order to correctly relay light patterns to the sample, which is the essence of the system. These components of the optical pathway are described below.

2.1.1.1 Light source: Ultraviolet light lamp

The ultraviolet light source used was the UV Spot Light Source from the LightningCure 200 series L7212-01 manufactured by Hamamatsu Corporation, New Jersey. Figure 2.2 shows the light source used. The lamp used was a 200W Mercury Xenon lamp (L6721). A built-in condenser reflector collects intense UV light emitted from the Mercury-Xenon lamp into a quartz fiber.


Figure 2.2: Hamamatsu LightCure UV Spot Light Source. It contains a 200W HgXe lamp and a reflector for the UV. The quartz fiber guide carries the UV light from the lamp to the next set of optical components.

The Hamamatsu UV lamp has a guaranteed lifetime of 2000 hours, during which the UV output intensity remains at 50% or more of the initial value. It has a radiant spectral range from 300nm to 500nm. It has a rotary-solenoid type of a shutter, which can be opened or closed in either of the two modes:

- Manual Mode: In this mode, the shutter is opened or closed using the ON/OFF (MANU) button.
- Automatic Mode: In this mode, the shutter can be opened using the AUTO button. The time for which it is required to be ON is then set on the front panel. After this period of time has elapsed, the shutter closes on its own. A 15 pin D-sub connector can be used with an external control device to turn the lamp on or off. The shutter can be remotely switched ON by an external control signal by shorting pins 12 and 15 for an instant.

The lamp needs to be switched ON and then stabilized for about 15 minutes, before it emits the maximum light intensity. In order to control the output light intensity, the source has a 'light control' knob on its front panel. The light source also has the capability to have a UV transmission filter installed into a specially made filter slot inside the unit.

2.1.1.2 The illumination system

The illumination system is shown in Figure 2.3. It consists of the quartz fiber optic guide, a quartz integration rod and the collimating lens. The light from the HgXe lamp is collected with the quartz fiber optic cable (A2873), and relayed to an integrator

rod. The integrator rod is also made of quartz so that a high transmittance of UV light is achieved. This integrator, as the name suggests, creates uniform light intensity across the image and maps the light to the same aspect ratio as the DMD.

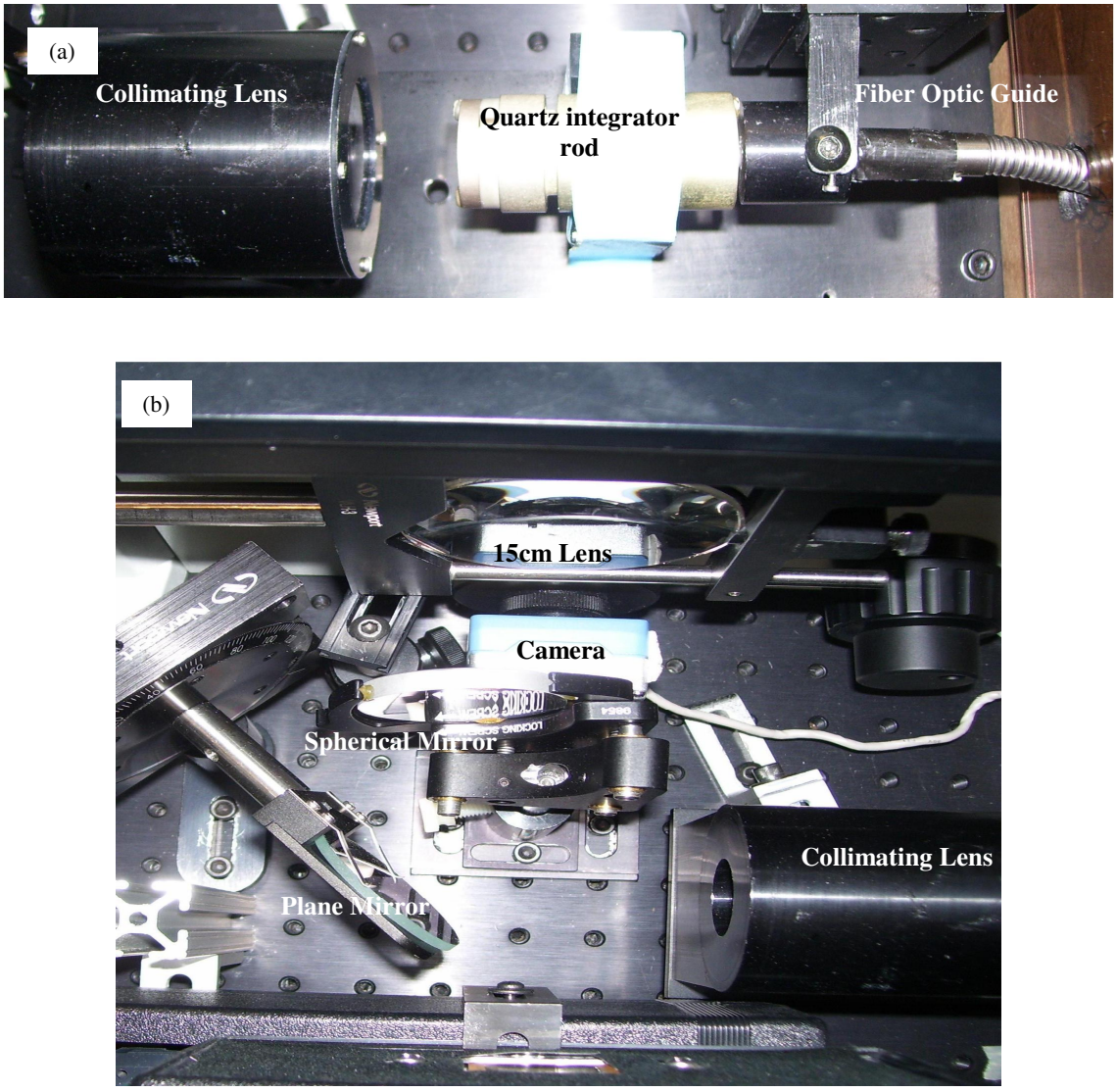


Figure 2.3: Illumination System used in the Nanopatterning System. Figure (a) shows the top view of the illumination system: Quartz fiber optic guide, integrator rod and the collimating lens barrel. Light from the collimating lens is seen falling on the plane mirror and onto the spherical mirror in figure (b). The spherical mirror focuses the imaged integration rod onto the DMD. The DMD is seen surrounded by a golden border at the bottom of the figure.

After this rod, the light passes through the collimating lens and then off a front surface mirror and a 50 mm focal length concave spherical mirror. Figure 2.3(b) shows the front surface mirror and the spherical mirror used to pass on the light from the magnification illumination lens to the DMD. The front surface mirror was mounted on an optical rotation mount (Newport Part RSP2), capable of turning by a few degrees, so that mirror could be positioned exactly to receive all the light from the collimating lens. The spherical mirror was mounted using OptiClaw (New Focus Part 9854-K) and is locked in the correct orientation with the help of a locking screw. This spherical mirror directs the light onto the DMD screen.

2.1.1.3 Digital light processor

The ability to project dynamic patterns of incident light at a subcellular level was achieved by using the digital light processor (DLP), a spatial light modulator manufactured by Texas Instruments Inc.

The DLP consists of four components:

- Analog video card
- Digital video driver card
- Video receiver card
- The Digital Micromirror Device (DMD)

In order to display the desired pattern on the DMD, the pattern drawn on the computer's monitor is first transmitted to the analog video card by a standard monitor cable. Since the analog video and the digital video driver cards are both interfaced with

the computer through a PCI slot, the pattern is then transmitted to digital video driver card via the computer. A connection is then made from this digital video driver card to the video receiver card, powered by a DC power supply. The video receiver card is connected to the DMD via a ribbon cable provided by Texas Instruments. The DMD surface can then recapitulate the exact image on the monitor.

The DMD is the key component of the DLP system. It is an array of almost 800,000 tiny individually addressable mirrors. Figure 2.4 shows the DMD screen surrounded by a golden frame. The XGA version was used for this project. This version of the DMD contains 1024 horizontal mirrors and 768 vertical mirrors. Each mirror is 16microns by 16 microns with one micron spacing between mirrors. Every microscopic mirror in this array is capable of tilting 10 degrees on either side of the normal.

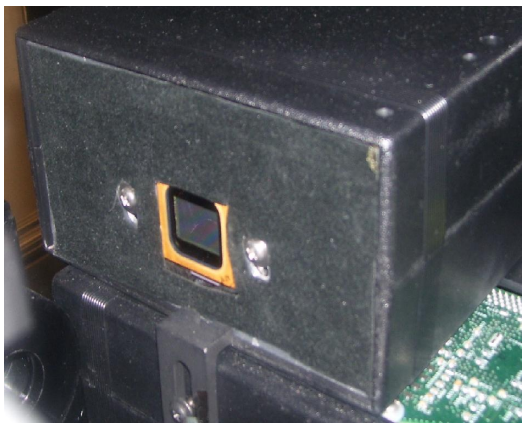

Figure 2.4: Picture of the Digital Micromirror Array (DMD). The Digital Micromirror array consists of 1024 x 768 tiny microscopic mirrors, each 16micron in length.

These two orientations are the two states of the mirror: ON and OFF. In the ON state, the mirror reflects the UV light to the target and in the OFF state; it reflects the UV light away from the target. By coordinated switching ON or OFF of specific mirrors, a unique digital pattern of light can projected from the DMD surface [76-77]. The DMD

thus, works as a digital light mask projecting patterns of light that enable partial cell studies.

The intrinsic properties of the DMD grant a set of unique cell manipulation abilities to the system. Every DMD mirror has a very short switching time between frames and can change its state from ON to OFF and vice versa in less than 21μs [77]. The optical switching time for the DMD is about 2 μs and the mechanical switching time for the mirrors to settle and latch is about 15 μs [76]. This offers a potential to reflect grayscale images by causing each mirror to cycle rapidly between the ON and OFF states, using a technique known as digital pulse-width modulation (PWM). If an individual mirror is turned ON longer than it is turned OFF within a given time interval, the reflected light from that mirror will appear brighter. Similarly, the reflected light will appear darker if a mirror is turned OFF longer than it is turned ON [76-77]. Using this technique, the DMD can reflect portions of a single mask at varying brightness levels. This allows for drawing varying grayscale patterns within the same digital mask enabling manipulation of parts of cells with different average doses of ultraviolet light.

In the past, the DMD has also been used for the generation of three dimensional views from two dimensional holograms [78]. Other DMD applications in biology include generation of rapidly customizable DNA and protein microarrays [79] and selective light activated epidermal growth factor activation for tissue engineering.

2.1.1.4 The focusing lens and the lens mount apparatus

The light pattern reflected by the DMD is captured by a 7.5cm diameter double convex lens of focal length 15cm (Edmund Optics). The optimum distance of the lens from the DMD is 16 ±1cm and from the dicroic mirror is 10.6 ±1cm. Figure 2.5 shows a schematic diagram of the relative distances of the DMD and the dicroic mirror from the focusing lens.

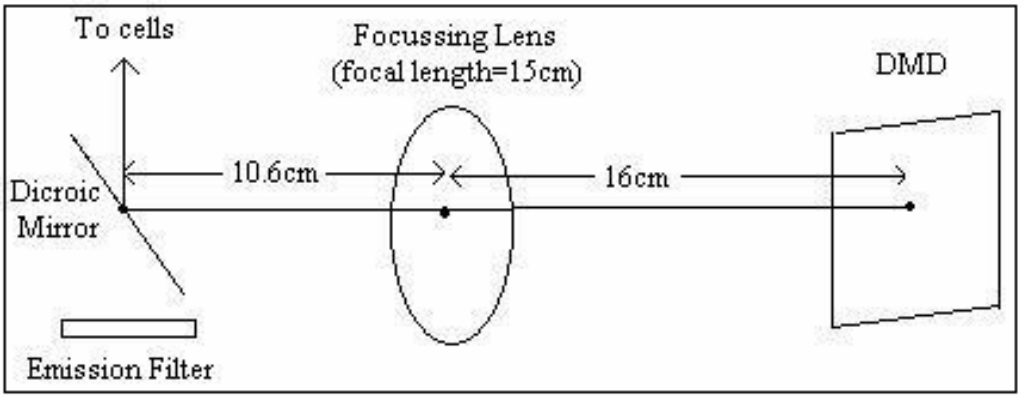


Figure 2.5: Relative distance of the Focusing Lens from the DMD and the Dicroic mirror. The center of the lens is aligned with the center of the dicroic mirror and that of the DMD.

The focusing lens is held in place by means of a custom made lens holder. This lens holder is capable of motion in the X-Y-Z directions and was constructed using standard optical posts, and a specially made plexi glass post holder. The lens is held in a metric Bar type holder purchased from Edmund Optics. The lens holder has a crossed V groove to hold the lens in place firmly. This crossed V-groove design also centers the optics vertically and horizontally. The lens holder is supported by stainless steel posts. A plexi glass post holder required for mounting the entire lens mount to the bench top was built and the post was fixed in it. The post holder was then mounted on a micro optical rail (Optosigma) so that when the post holder is moved across the span of the

micro rail, then the lens would move toward or away from the DMD. Figure 2.6 shows the lens held by the lens holder.

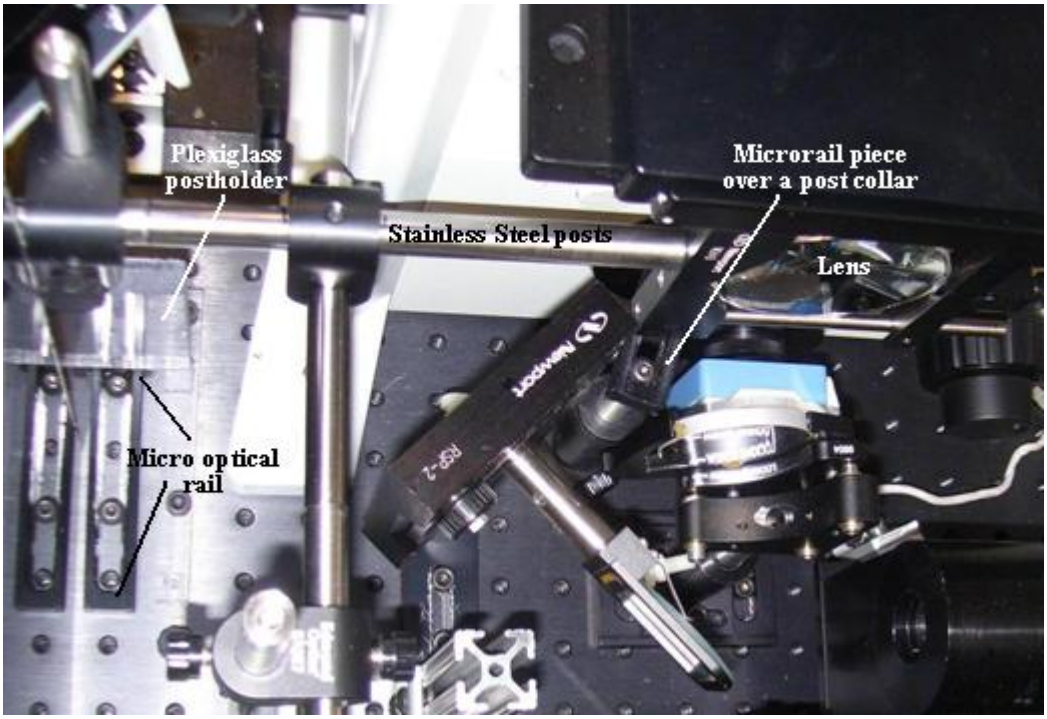


Figure 2.6: Picture of the Lens Mount Assembly. This figure shows the location and the construction of the entire lens mount assembly. After the patterned light is reflected from the DMD surface, it passes through the lens placed at 16cm from the DMD surface. The center of the lens is aligned with the center of the DMD screen and that of the dicroic mirror. A metric bar type lens holder holds the lens in place as shown. The stainless steel post supports the lens holder and another post right angled post is used to provide stability to the first post. The post is fixed in a plexi glass (seen toward the extreme left) post holder, which in turn is attached onto a microrail. Movement of the plexi glass postholder allows movement of the lens in X-Y-Z directions.

Since the lens and the lens holder assembly weigh a considerable amount, the post holding the lens holder was supported in the center by making it rest on a small microrail piece. This piece was placed over a post collar (Edmund Scientific Corporation). This post collar gives the flexibility to increase or decrease the height of the microrail and thus continue supporting the lens post even if the lens holder is lowered or raised. The lens holder is thus capable of accommodating lenses with different diameters, and allows three directional movement of the lens, which was

crucial in the experiments that determined the focal length of the focusing lens in the first place.

After passing through the lens, the light is transmitted to the filter cube in second subsystem, the epifluorescence microscope.

*2.1.2 Epi-fluorescence microscope system*

The next most important subsystem in the nanopatterning system is the epifluorescence microscope. The inverted epifluorescence microscope IX71 was purchased from Olympus. In an inverted microscope, the objective and the filter turret are situated below the stage and the specimen. Therefore, a petri dish containing growth medium and cells adhered to its bottom can be placed over the objective and live cells can be observed. This is unlike the conventional upright microscope where cells incubated in cell medium cannot be studied. The nanopatterning system is used for live cell imaging and hence an inverted microscope was selected.

The microscope subsystem has a provision for light from two light sources to enter the microscope from two different ports perpendicular to each other. Figure 2.1(a) shows the entire nanopatterning system. Also, shown are the two light sources for the system. The first light source is the conventional mercury lamp delivering a white light spectrum (U-ULS100HG from Olympus Optical Company) and the second source is the patterned light reflected from the DMD. The first light source is used when cell dyes excitable at various wavelengths in the white light spectrum are to be viewed in cells. The filters and the dicroic mirrors in the microscope are chosen to match the spectral

excitation and emission characteristics of the fluorophore used to label the specimen. For example when propidium iodide is to be viewed, a light of excitation 538 nm is needed. Therefore white light is projected on the 61002 triple bandpass filter cube (Chroma technology) and red image is observed. This source is only used to observe excitable dyes for improved cell component visualization.

The filter cassette in the microscope originally had only one opening in its cover, letting in light only from the mercury lamp white light source. In order to also project patterned light coming off the DMD surface through the 15cm focal length lens into the side port of the microscope, a square shaped hole was machined in the cassette by using a mill. The second light source projects desired organelle specific patterns of UV light on the cells. It is this light that can be manipulated to form virtual light masks to irradiate partial cells or organelles, etc. This light source plays a vital role in achieving subcellular targeting capabilities. This source requires the U-MWU filter cube placed into one of the slots in the filter turret of the microscope to receive the light from the DMD. Every filter cube consists of an excitation filter, which allows transmission of specific wavelengths of light; a dicroic mirror, which is a special mirror that reflects one range of wavelengths and allows another range of wavelengths to pass through and an emission filter, which is a long pass filter for higher wavelengths. The U-MWU cube was slightly modified by removing its excitation filter before it was used to project the UV light masks onto the cells. The excitation filter considerably decreased the UV power entering the microscope; therefore it was removed from the U-MWU filter cube. Removal of the excitation filter from the U-MWU filter cube did not alter

the incident light spectrum because the input light had a wavelength band of 350nm-500nm (discussed in section 3.1.1), which was a combination of the specific wavelengths passed by the excitation filter and some harmless visible light. The dicroic mirror in the U-MWU passes all wavelengths above 400 nm through it, and the emission filter is a long pass filter that passes all wavelengths above 420 nm. When the second light source is used, the light (350nm-500nm) reflected from the DMD passes through the lens and reaches the dicroic mirror in the U-MWU. After getting reflected from this mirror, the ultraviolet light reaches the cells through the objective lens. The cells can be targeted with UVA light in this way.

These two light sources can be switched depending on the need. When patterned light is to be projected on specific areas in cells, the second light source is used and the side port filter cube is selected. The first light source is used to view fluorescent dyes loaded in the cells or organelles by use of a suitable filter cube for that dye. After the light from either of the light sources is incident on the specimen, fluorescent light of a higher wavelength is collected by the objective lens and it passes through the dicroic mirror and the emission filter. The emission filter eliminates wavelengths higher than those of this fluorescent light, and thus gives a high light intensity. The light is then transmitted to the camera port (80% to the camera and 20% to the eyepiece) or the eyepiece (100% to the eyepiece). In epifluorescence microscopes, the objective not only focuses the excitory light on the specimen, it also collects the fluorescent light from the specimen. A 60X magnification objective lens

was used so that key subcellular components of the order of a few microns could be imaged clearly. In some experiments, a 10X lens was used to observe cells.

*2.1.3 Environmental chamber*

In order to maintain the optimum environmental condition for live cells, an environmental chamber capable of temperature, gas mixture and humidity control was constructed. The chamber was engineered onto the stage insert plate of the microscope. (Courtesy: Tom Leeds, UTA workshop). Figure 2.7 shows the environmental chamber. The diameter of this chamber is 10 cm and its height is 5 cm. A lid made of thick plexi glass, was made with a slight groove along its periphery, just enough to fit into the aluminum walls of the chamber. This lid enabled the chamber to be contained with the gas supplied to it.

- Temperature Control:

In order to exercise control over experimental temperature, a circular thermal heating pad was wound to the walls of the aluminum chamber. This pad was connected to a controller (part number 2001 Model VI), which has a circular dial from OFF; MEDIUM to HIGH allows selection of the desired modes of heating. Figure 2.8 shows the Kendrick Dew Remover System Controller.

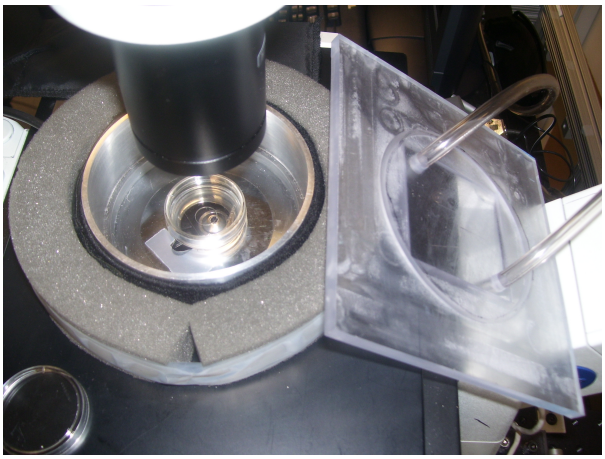

Figure 2.7: Picture of the Environmental Chamber. The thermal pad is wrapped around the aluminum chamber for efficient temperature control. Blood gas mixture is supplied to the chamber with the help of the tubing seen entering the chamber lid. This figure also shows the placement of the petri dish containing the cells.


Figure 2.8: Picture of the Temperature Controller. This Controller is used to regulate the temperature inside the environmental chamber. It has a dial to select OFF, MED, HIGH modes of temperature control.

This temperature apparatus can warm the environmental chamber from a room temperature of 22$^{o}$C to a maximum of approximately 42$^{o}$C. By correctly adjusting the controller settings, the pad can thus be heated to reach the desired temperature. For all cell experiments, the temperature apparatus was switched ON one hour before the start of an experiment so as to attain a stable temperature of 37$^{o}$C, as required by mammalian cells. The thermal pad and the controller were components of a dew removal system originally manufactured for amateur telescopes and were purchased from Kendrick astro instruments, Canada. The temperature can be checked by an infrared thermometer (Model Number: 0S-603, Omega Engineering Incorporated). It has a sensor that can be placed inside the environmental chamber to determine the temperature. The thermometer displays the temperature in the chamber in either Fahrenheit or Celsius digitally.

- Humidity control

In order to maintain the pH of the cell medium, a 5% $CO_2$ environment is required. A Blood Gas mixture cylinder was purchased from Airgas Incorporated (UN 1956). This gas mixture contains 5% $CO_2$ + 21% oxygen + 74% nitrogen. A gas regulator adjusts the gas flow rate at 5psig, just enough to maintain 5 % $CO_2$ in the chamber. Care was taken to ensure that the gas pressure was not too high to create turbulence in the cell medium. The flow rate was such measured by filling the gas in a balloon for 10 seconds and then submerging the inflated balloon in a measuring cylinder full of water. The volume of water displaced was equal to the volume of air inside the balloon and was found to be 200ml. In order to cross check this, volume was also calculated by finding a product of the area of the base of the cylinder and the increase in the water level. This was found to be 200.57cubic centimeter (cc). In order to find the flow rate per minute, this value was multiplied by a factor of 6, and the final flow rate was calculated to be 1200±10cc/min. Connecting tubing was used to carry gas from the cylinder into the chamber, through holes in the chamber lid. A second pike tubing was used to collect the gas from the chamber to the exhaust, bubbling into water in a beaker as a simple monitor of flow. Experiments were conducted to compare the cell survival rates in this chamber with those at room temperature without temperature and humidity control.

*2.1.4 Image acquisition subsystem*

The image acquisition subsystem consists of the Motic Moticam 2000 camera and the camera software for acquiring real time pictures of the cells. The Motic Images Plus Version 2.0 ML camera software was provided with the camera. The Moticam 2000 is a compact professional camera encased in light weight aluminum offering a resolution of 2.0 megapixels. Figure 2.9 shows the Motic Moticam 2000 camera.


Figure 2.9: Picture of the Motic Moticam 2000 Camera adapted from [80]. The Motic Moticam 2000 camera is encased in light weight aluminum and has a USB connecting cable to connect to the computer.

right below the 15cm lens. The USB 2.0 connecting cable permanently attached to the camera was connected to a computer, and the Motic Images Plus camera software was installed on this computer. Important specifications of the Moticam 2000 [80] are listed in Table 2.2.

Table 2.2: List of Motic 2000 camera specifications adapted from [80]

| Particulars | Moticam 2000 |
|---|---|
| Included Software | Motic Images Plus 2.0 , Multilanguage |
| Image Device | 1/2" CMOS |
| Lens | 16mm |
| Effective Pixels | 1600x1200 |
| Still Image Resolution | 1600x1200 |

Table 2.2 – continued

| | |
|---|---|
| Scanning System | Progressive scan mode |
| Max. Frame Rate | 10fps @1600x1200 , 40fps @800x600 |
| Data Transfer | 480MB / second |
| Minimum Illumination | 3 lux |
| Lens Mount | C-mount (12.5mm) |
| Shutter | Manual |
| Video Output | Transmission across Motic software direct into memory of PC |
| White Balance | Automatic / manual (control by software) |
| USB Output | Yes |
| USB Power Supply | 5V self-power from computer |
| Microscope Adaptors | 4 different sizes included |
| USB standard | 2.0 |
| Minimum system requirement | P3 1GHZ or higher, HDD 1G unused, RAM 256MB,<br>Display Memory 32MB, Windows2000 & XP |

When the Motic Images Plus 2.0 ML is run, the workspace is displayed. In order to view the specimen image in real time, the capture window button is clicked. A screenshot of the capture window is shown as in Figure 2.10. The control panel can be used to change the quality and effects of the preview image. The gain, exposure, sharpness operations can be adjusted through slider bars to obtain the best quality images. 'Capture' is used to capture the real time image in the preview window. This image is saved in a temporary folder. The user can then save it elsewhere permanently. The 'Autocap' confers upon the user the ability to automatically capture series of images at specified intervals of time for a given amount of time. The camera software also enables users to record a movie by clicking on 'Video'.

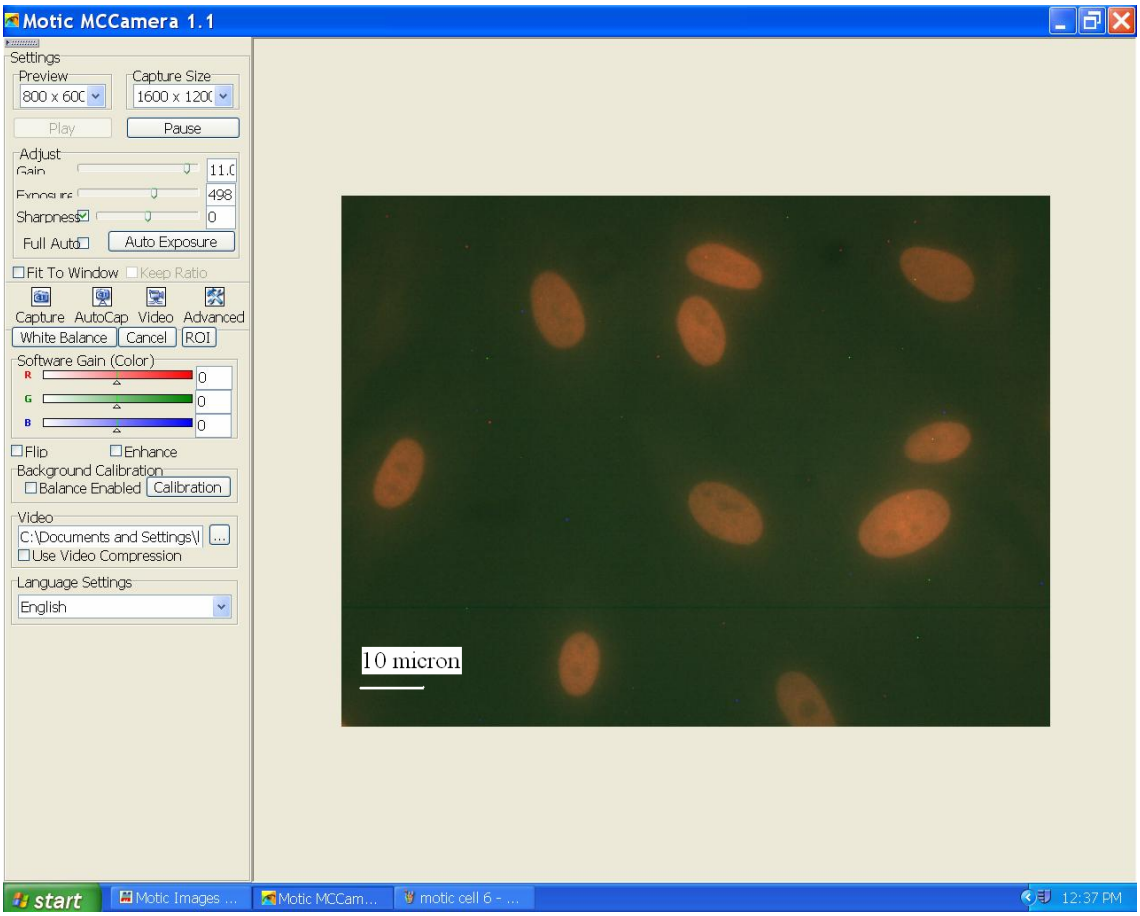


Figure 2.10: Screenshot of the Motic 2000 ImagePlus Software Workspace. Seen in the figure are the tile bar (top), control panel (left) and the image window (right). Cell nuclei were stained red with propidium iodide dye and this image was captured with a 60X magnification objective lens. (Scale bar: 10micron)

Motic 2000 camera also enables users to adjust the brightness, contrast and saturation of the images. If the brightness is adjusted or the specimen switched during observation, the Auto exposure and white balance commands can be used to adjust the image back. Background calibration should be done so as to ensure accuracy of the system's measurements. An ROI (Region of Interest) function is provided as well. The pixel pitch for this camera is 4.2micron [80]. When a 60X objective lens is used to view the specimen, the final resolution is 0.45 ± 0.06micron.

## 2.2 Cell culture

In order to perform experiments on human cells and subcellular components, and to determine their sensitivity to UVA light for research in human medicine; human skin fibroblast cell line ATCC CRL-2522 was used. Cell culture was performed in the tissue culture room (Division of Translational Research, UTSW). The cells were cultured in petri dishes (P35G-0-10-C Mattek Corporation, Ashland). These dishes have a diameter of 35mm, uncoated glass bottom, number 0 cover slip thickness, and 10 mm microwell diameter. The cells were cultured in Dulbecco's Modified Eagle Medium (DMEM) (1X), liquid (4.5 g/L D-glucose) supplemented with 10% Fetal Bovine Serum (FBS). The FBS was heat inactivated by heating to 56$^{o}$C for 30minutes prior to being mixed with the DMEM. This medium will be henceforth referred to as 'D10' for simplicity. DMEM (catalog number: 10313-021) and FBS (catalog number: 16000-077) were bought from Invitrogen Corporation. Trypsin-EDTA(catalog number: 25200-056, Invitrogen) was used for passaging the cells by aiding in the detachment of cells from the monolayer. Another medium called the defined medium was used to serum starve cells one day prior to the experiments as required by the experimental protocol (discussed in section 3.2.1). The defined medium consisted of RPMI 1640 without phenol red(catalog number: 11835-030 Invitrogen), SPIT(catalog number: S5791, Sigma Aldrich), Serum Replacement 1 (catalog number: S0638, Sigma Aldrich) at 1X concentration. This study was exempt from the IRB review for it uses commercially available anonymous cell lines. (IRB Number: 032008-029)

## 2.3 Probes and stains used to view cells and nuclei

Numerous dyes for staining cells and their organelles are commercially available. These stains have properties to bind to or react with different structures in a cell, offering a way to highlight such structures over others. Molecular probes may be specific to the cell nucleus, the cell membrane or any other cellular organelles. In our experiments, the nuclear stain DAPI (catalog number: D1306, Invitrogen) was used to visualize the viable cell nuclei. DAPI shows a bright blue fluorescence when it binds to DNA in the cell nucleus. Propidium Iodide (P-1304, Invitrogen) was used as the dead cell probe to determine the damaged dead cells during the experiments.

The serum starved cells were taken out of the incubator and incubated in 0.5μg/ml DAPI solution for 5minutes in dark, covered in an aluminum foil. After the incubation in DAPI, the cells were washed with the defined medium once and then were suspended in 1μg/ml of propidium iodide in the defined medium.

The 61002 triple bandpass filter set (Chroma Technology) is used to view fluorochromes DAPI and Propidium Iodide simultaneously. The modified U-MWU filter set was used to project UV light incident from the DMD screen to the objective lens and ultimately to the cells. Since the incident UV light on the cells was (350-500nm) with one peak at 365nm, no excitation filter was required. The modified U-MWU could also be used to view DAPI. The absorption and emission peak wavelengths and filter sets used to view these dyes in cells are summarized in table 2.3.

Table 2.3: Spectral characteristics of the fluorescent dyes DAPI and propidium iodide

| Molecular Probe | Excitation(nm) | Emission(nm) | Filter Cube |
|---|---|---|---|
| DAPI | 365 | 461 | Modified U-MWU (without excitation filter) |
| DAPI, Propidium Iodide | 538 | 622 | 61002 triple bandpass filter set |

A method of marking dead cells was adopted where the instant at which propidium iodide entered the cell body was recorded as the cell's time of death and this was recorded for each individual cell. Since DAPI is not used to tag dead cells, a cell's viability could be made based on whether its nucleus appeared red or blue.

Although a high dye concentration is an effective method to increase fluorescence intensity, it can cause cell damage and photobleaching interfering or complicating experiments. In order to determine the optimum dye concentration that would cause the least damage to the cells and at the same time ensure photostability of the cell staining, a series of experiments were conducted with varying concentrations of both the dyes used. Data from these experiments suggested that 0.5µg/ml DAPI concentration and 1µg/ml propidium iodide concentration fulfilled our requirements for limited cell damage, reduced photobleaching and a clear readout of the cell status. These were therefore selected as the optimum dye concentrations for all further experiments. In all further chapters, these concentrations 0.5µg/ml for DAPI and 1µg/ml for propidium iodide will be referred to as 1X dye concentration. Therefore 0.1X concentration of dyes would mean a concentration of 0.05µg/ml for DAPI and 0.1µg/ml for propidium iodide and so on.

## 2.4 Experimental procedure

The experimental procedure adopted for all the cell experiments was:

(1) First, the cells were serum starved and placed in the defined medium in the incubator for 4-24 hours before the start of the experiment as described in the section 2.2 on Cell Culture.

(2) An hour before the start of the experiment, the temperature apparatus was switched ON. This allowed the temperature inside the environmental chamber to reach 37$^{o}$C, as required by human cells used in all experiments. (Discussed in section 2.1.3)

(3) To begin an experiment, serum starved human skin fibroblast cells were taken out of the incubator and incubated in DAPI working solution (0.05μg/ml in PBS) in dark. After 5 minutes of incubation, the cells were rinsed once with defined medium and then propidium iodide working solution (0.1μg/ml in defined medium) was added to them.

(4) Following this, the cells were placed in the prewarmed aluminum environmental chamber. All experiments were performed at 37±1$^{o}$C and 5% $CO_2$ (with a flow rate of 1200cc/min) conditions.

(5) An experimental cell was picked to accurately map the subcellular component to be targeted. In order to mark the cell nuclei, cell cytoplasm or the cytoplasmic membrane boundaries, a software program was written in Interactive Data Language (IDL)(Courtesy: Dr. Michael Huebschman). This program permitted the user to select and mark any target region in a cell. This image of the marked areas

within a cell was then resized according to the DMD dimensions to create digital light patterns on another computer, which in turn is interfaced to the DMD.

(6) The DMD then recapitulated these patterns and projected them as digital light masks to irradiate the desired cellular target using the nanopatterning system as described in system design. The modified U-MWU filter cube was used to irradiate ultraviolet light on partial cells.

(7) Since the nanopatterning system requires the user to manually capture the image of cells and update the digital patterns on the DMD screen according to the cell and organelle movement, images of cells were taken in 5 minute intervals. This enabled observing the cells at short intervals of time and also provided adequate time for the user to adjust and update the projected pattern.

(8) Just before recording an image, the filter cube was switched to the 61002 triple passband filter cube to view the dead cell marker entering damaged cells, and a picture of cells was captured. The cube was then changed back to the modified U-MWU cube for the light pattern to target the partial cell between every two consequent images. This procedure was repeated until all the cells died, which marked the end of the experiment.

(9) After each experiment, the number of dead cells between two consecutive captured images was counted periodically in order to obtain cell survival curves. Graphpad Prism Statistical Analysis software (GraphPad Prism version 5.01 for Windows, GraphPad Software, San Diego California) was used to perform Kaplan Meier

survival analysis in order to obtain the cell survival curves and to analyze the data further. A flowchart diagram of the general experimental procedure is shown in Figure 2.11.

Varying UV dosage experiments were performed for each of the categories: nucleus alone, cytoplasm alone and entire cells. For control experiments, no UV light patterns were used and cells were observed in the absence of any UV light. Experiments involving specific illumination of the cell nucleus and the cell cytoplasm at various UV intensities were conducted in this manner. Other experiments specifically illuminating the cell membrane were also performed to calculate the membrane velocity in response to UV light.

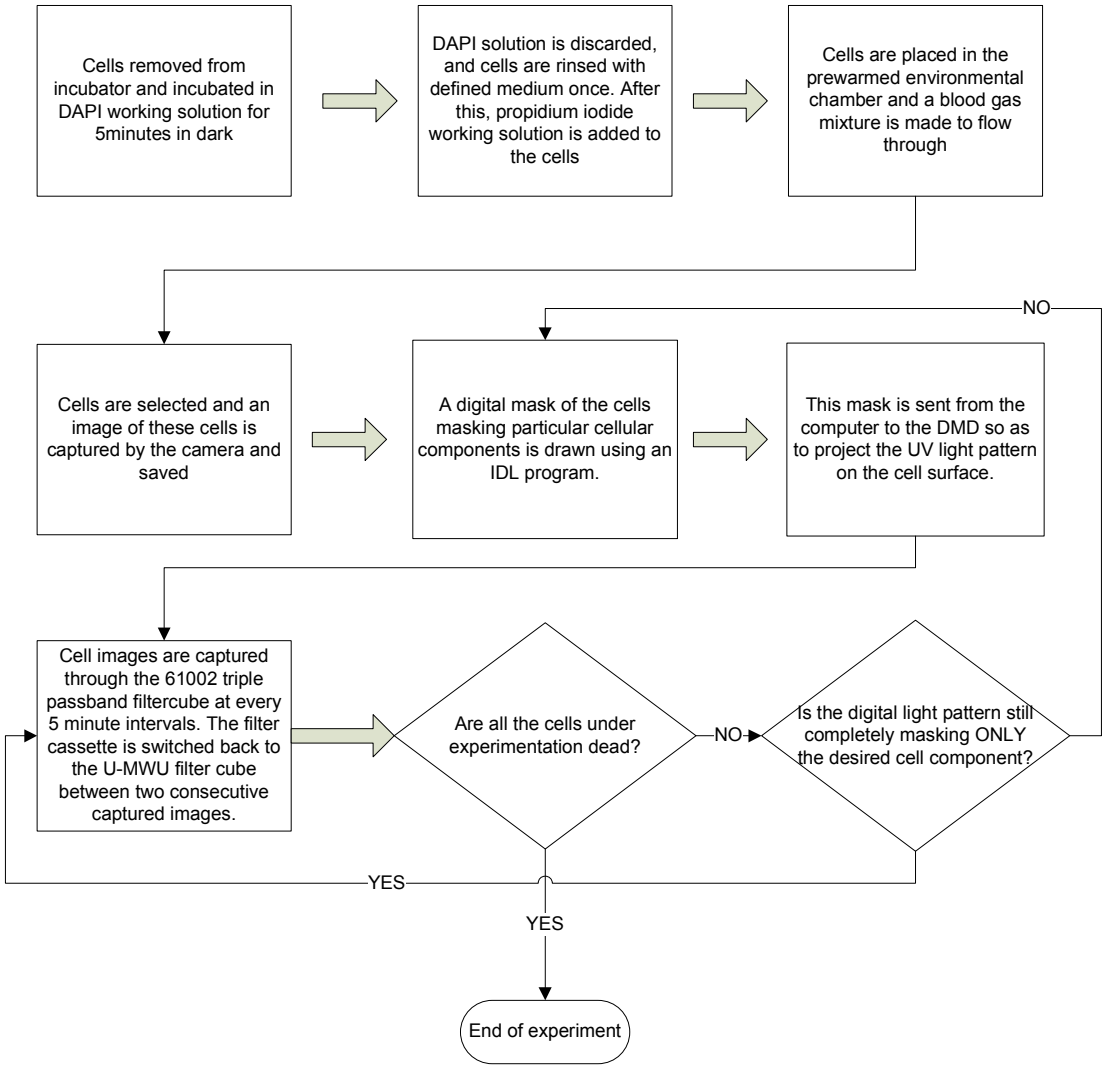


Figure 2.11: Flowchart diagram showing all the steps of a standard experimental procedure. This experimental procedure is to be used when DAPI and propidium iodide are used.

# CHAPTER 3

# SYSTEM PARAMETERS AND OPTIMIZATION

The overall goal of this chapter is to discuss system parameters and optimization, knowledge of which is essential to effectively use the nanopatterning instrument to conduct successful biology based research experiments. This chapter is presented as two sections. In the first section, characterization of the nanopatterning system parameters is discussed. The second section deals with results pertaining to optimization of system parameters to achieve the best system performance.

## 3.1 Determination of system parameters

A number of criteria are critical to the operation of the nanopatterning system. It is important to establish the parameters: input wavelength, sample temperature and flow of the blood gas into the environmental chamber, the size of the projected pattern, the switching time of the DMD and the switching time between two patterns for acquiring highly accurate data. Parameters including system resolution, image acquisition resolution and the range of available power density values that the system can output, are also important for data analysis.

*3.1.1 Determination of the input wavelength of light*

In order to find the final input spectrum for the nanopatterning system, the wavelength spectra of all individual system optical components were determined by use of a spectrophotometer. The UV lamp delivers the range of wavelengths from 300 to 500 nm with three excitation peaks at 365nm, 403nm and 436nm. The other optical path components like the integrator rod are made of quartz, which transmits all wavelengths of UV light. The wavelength scan for the focusing lens showed that it passes all wavelengths above 320nm. The objective lens also lies in the path of the light and was observed to transmit all wavelengths above 350nm. The base of the petri dish was the final component that the light passes through before reaching the sample and its wavelength scan displays the transmittance of all wavelengths above 280nm.

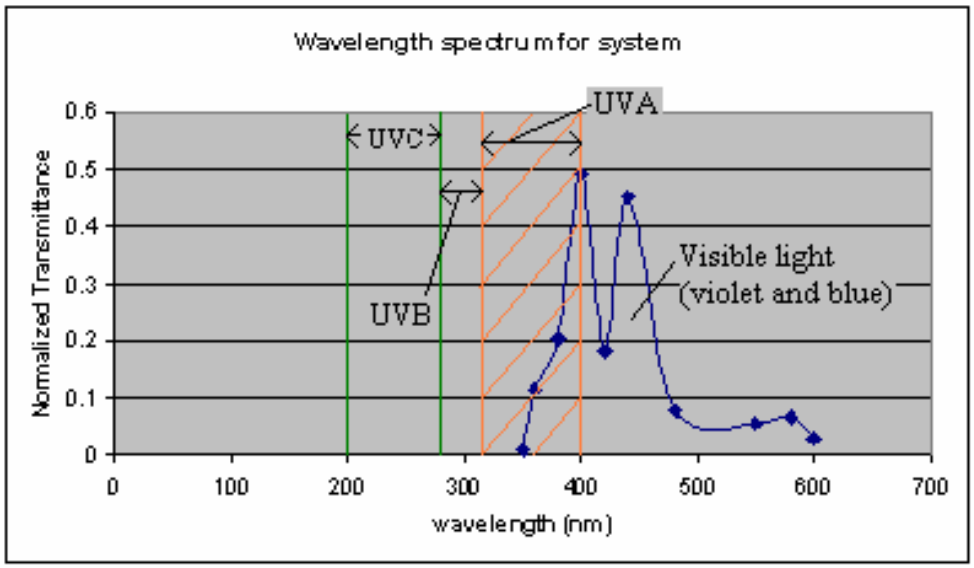


Figure 3.1: Wavelength Output Spectrum of the Nanopatterning System. The wavelength spectrum for the nanopatterning system is represented by the blue curve in this figure. The range of UVA wavelengths is marked in orange, while the UVB and UVC ranges are seen as green lines. The nanopatterning system also transmits violet and blue light which fall under the visible light spectrum.

The wavelength spectra of each individual component were combined and normalized to obtain an overall input wavelength spectrum for the system. Therefore, the system as a whole can primarily deliver 350nm to 500nm patterned light at its objective tip. Figure 3.1 shows this spectrum as a blue curve. A large portion of the light reaching the objective tip falls in the UVA category (315-400nm). As seen from the figure, the nanopatterning system does not transmit any of the UVB (280-315nm) or UVC (200-280nm) radiation to the sample. Violet (purple) and blue light having the wavelengths of 380-450nm and 450-495nm also form a large part of the input wavelength for the system.

*3.1.2 Determination of the range of operation of temperature and flow rate of the blood gas mixture*

At room temperature, the environmental chamber temperature is about 22 $^{o}$C. The temperature control apparatus is capable of warming the environmental chamber to a maximum of about 42$^{o}$C. The range of operation for the system therefore, is about 22$^{o}$C to 42$^{o}$C. The chamber temperature can be maintained at 37$^{o}$C ± 1$^{o}$C, as required by mammalian cells, by correct adjustment of the temperature controller. In order to reach the temperature of 37$^{o}$C, the heating apparatus needs to be switched ON for an hour.

In order to maintain the pH of the cell medium at the optimum value and to prevent any turbulence caused inside the chamber and the petri dish, the blood gas

mixture flow rate was adjusted to 1200±10cc/min inside the environmental chamber, the gas was continuously supplied to the chamber at a pressure of 5-10psig.

### *3.1.3 Determination of the projected pattern size*

The DMD screen is made up of 1024 x 768 pixels, each pixel corresponding to a tiny mirror. The pattern projected from the DMD is therefore composed of 1024 x 768 pixels. The capture window captures the image of the sample and the size of this capture window is 1600 x 1200 pixels. The IDL software program mentioned in Chapter 2, resizes the dimensions of the marked areas (ROI) in a sample to the size of the DLP.

### *3.1.4 Determination of the switching time for the DMD and the switching time between two patterns*

The DMD optical switching time is the time required to change the state of a mirror from ON to OFF or vice versa and thereby rapidly turn the light ON and OFF. This switching time is given as 2μsec [76]. The mechanical switching time of the DMD is the time required to settle and latch the mirror in its ON or OFF state and is about 15μsec [76]. The switching time between two patterns is considerably higher because the system is manually operated and requires the user to change the projected patterns with respect to the movement of the cells. This time is currently about 1-2minutes.

*3.1.5 Determination of the system resolution and the image acquisition resolution*

One of the key system parameters is its resolution. After the nanopatterning system was engineered, the overall resolution of the system was measured. The pixel pitch for the Motic Moticam 2000 is given as 4.2 micron x 4.2 micron [80]. Because a 60X objective lens was used, every pixel on the camera screen would correspond to 4.2/60 = 0.07micron. Therefore, the image acquisition resolution of the system is 0.07micron. For example, if six pixels are counted on the camera screen, it would correspond to (6*0.07) micron.

In order to find the resolution of the nanopatterning system, a pattern consisting of three lines each of one mirror width with a mirror wide spacing between the lines was projected from the DMD screen. The corresponding UV pattern was then recorded on the camera. Each pixel on the DMD screen corresponds to 'x' number of pixels on the camera capture window. However, for the one mirror wide lines, it was not possible to distinguish between the lines because the acquisition and projection size scales were approximately the same. Therefore, the same procedure was repeated with lines each two mirrors wide with a spacing of two mirrors between them. Figure 3.2 (a) shows the screenshot of the UV pattern projected when three lines each two mirrors wide, were placed alongside each other with a two mirror spacing between them. In the magnified portion of this figure (seen in figure 3.2(b)), the lines in the pattern could be distinguished from one another. A profile plot for this magnified image was drawn in Image J software (available online at *http://rsb.info.nih.gov/ij/*). Three peaks and two troughs in the grayscale value are visible in figure 3.2(c), and these represent the three

lines and the two spaces respectively. The number of camera pixels corresponding to the width of each line and that of the space between the lines was counted as 6,5,7,7 and 7 camera pixels respectively. The number of pixels were counted manually or the profile plot can also be used to infer these values. The number of microns each of these lines corresponded to was calculated as the number of camera pixels in the line width * 0.07, as explained above. These values were found to be 0.42, 0.35, 0.49, 0.49 and 0.49 microns respectively. The average for these values computed as 0.45 micron. Therefore, the average value of a line width in microns equal to 0.45 micron was accepted as the system resolution. The standard deviation was calculated as 0.063 micron.

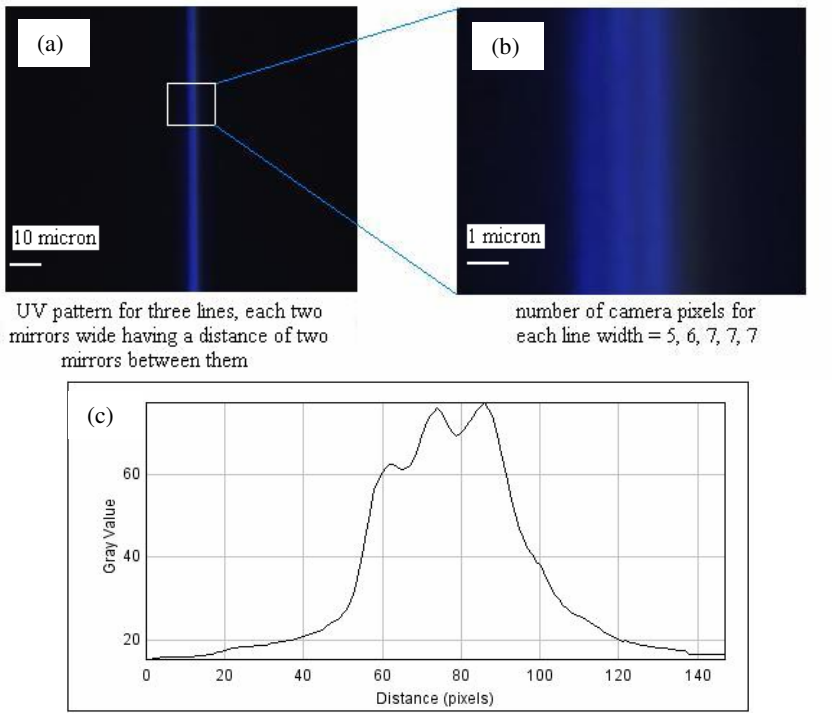


Figure 3.2: Calculation of the Nanopatterning System Resolution. Figure (a) shows the image of the projected three lines, each two mirrors wide, having a spacing of two mirrors between them. In figure (b), a small portion of figure (a) is magnified. The number of camera pixels that each of the three lines and the two spaces represented, is also mentioned. In figure (c), a profile plot for figure (b) is shown. This profile plot was drawn in ImageJ software. Three peaks are observed corresponding to each of the projected lines. Number of camera pixels corresponding to each line can also be inferred from figure(c) and are required to calculate the resolution for the system. (Scale bar: Figure (a) 10micron, Figure (b) 1 micron)

Subcellular patterns of UV light (Demonstration of submicron scale patterning)

Mammalian cells are about 10-100 microns in diameter. Sub cellular structures are even smaller in dimension. A cell nucleus normally measures about 11-22microns in diameter [13]. The nanopatterning system allows for subcellular patterning at this scale. The ability to target partial cell nuclei is demonstrated from the images below in which certain alphabets, letters, or shapes have been patterned inside a cell's nucleus stained with DAPI.

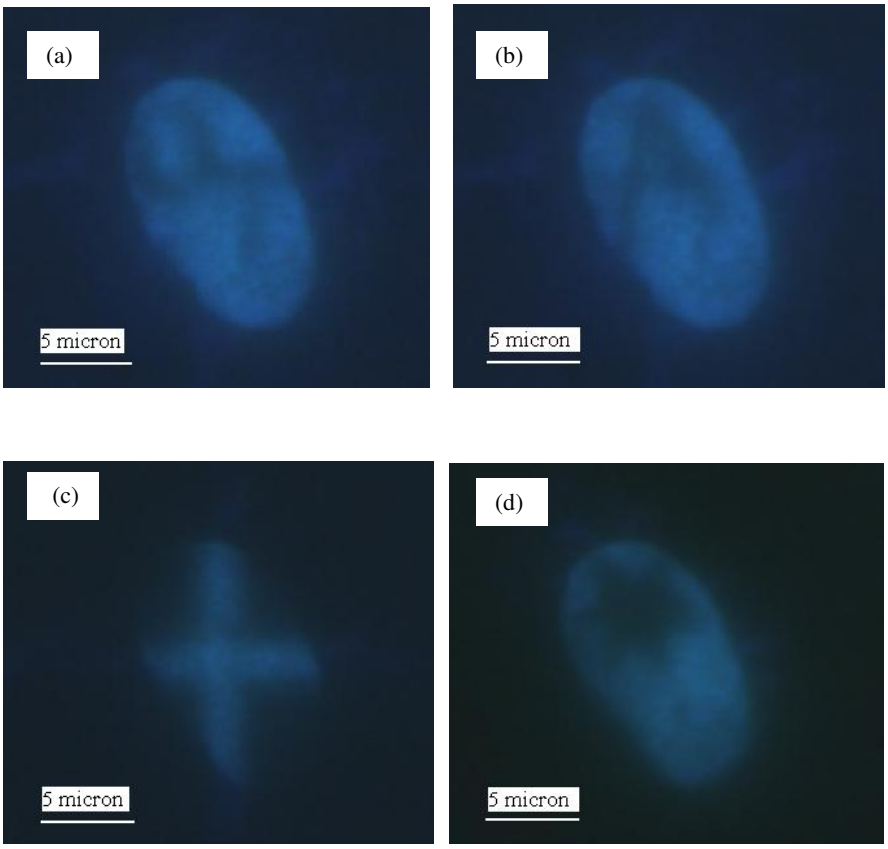


Figure 3.3: Ability of the Nanopatterning System to specifically illuminate submicronal structures in a cell nucleus. Letters 'UT', the alphabet 'A', a plus sign and a 'star' are patterned inside the cell nucleus as seen in figures (a), (b), (c) and (d) (Scale bar: 5 micron)

Figure 3.3(a) shows the letter 'UT' patterned inside the cell nucleus. Similarly, figure 3.3 (b), (c) and (d) show the letter 'A', a plus sign and a 'star' shape respectively. These

images are indicative of the system's high resolution (0.45micron) and flexibility of manipulating partial cell nuclei.

### *3.1.6 Determination of the output power density*

The range of the UV light intensity available at the objective tip was determined by the use of a UV power meter. (OAI-106 U.V. Powermeter, Optical Associates Inc., California) The power meter probe has a small sensor, which was placed over the objective lens in order to read the output power density. The power meter is designed to read the intensity at 365nm. The nanopatterning system has an input spectrum of 350 to 500nm. Therefore, only a part of the actual power density is read by the meter. The power density range for the nanopatterning system when all the pixels projected from the DMD were turned ON was 0 to 3.65mW/cm$^2$ when a 60X objective lens was used. When a grayscale image was projected, the average power density could be made lower than 3.65mW/cm$^2$.

## 3.2 Optimization of system performance

The performance of the nanopatterning system depends on a number of criteria such as the kind of the cell medium used, the concentration of the molecular dyes used, and the temperature and humidity conditions provided by the environmental chamber. Determination of suitable settings of each of these criteria is essential in order to achieve the most optimum results.

*3.2.1 Selection of the defined medium as the optimum cell medium for all cell experiments*

It is important to select the right cell medium for use during all cell experiments. The cell medium that promotes maximum cell survival and has the least toxic reaction with the added fluorescent dyes would be a suitable medium to use for experimentation involving live cells. Two cell media were tested for use with fluorescent dyes for experiments aiming to achieve optimum experimental conditions in the environmental chamber. These two media were:

- DMEM with phenol red, a pH indicator, and supplemented with 10% FBS (D10).
- Defined medium free of phenol red and mitogenic factors

In the beginning of this study, the goal was to study the effect of light activated growth factors on cells. For this, it was required to use the defined medium with cells to remove the mitogenic factors. However, over a period of time, the study was modified to study the effect of UV light only without any additional agents and use of defined medium was no longer required. For use in our experiments, we compared the defined medium with the D10 medium, which was the medium the cells were normally incubated in.

In order to assess the cell viability in these media, the fluorescent dyes DAPI and propidium iodide were added in the concentration 1X, 0.1X and 0.02X to each of these media. (0.5µg/ml for DAPI and 1µg/ml for propidium iodide are considered as 1X concentration as mentioned in section 23.) DAPI was used as a nuclear stain while the

propidium iodide dye was used as a dead cell marker. Since this experiment pertained only to the selection of a suitable medium for the cells, it was performed without any ultraviolet light illumination. During each experiment, the number of dead cells was counted periodically in order to obtain survival curves for each medium at each concentration. Graphpad Prism Statistical Analysis software was used to perform Kaplan Meier survival analysis in order to obtain the cell survival curves. Figure 3.4 shows these survival curves for the two media at the three dye concentrations with the percentage of live cells on the Y axis and the time in minutes on the X axis. As seen in the figure, survival curves for experiments where D10 was used as the cell medium indicate that 50% of the cell population was dead by 50min, 80min, 85min at 1X, 0.1X and 0.02X dye concentration, respectively.

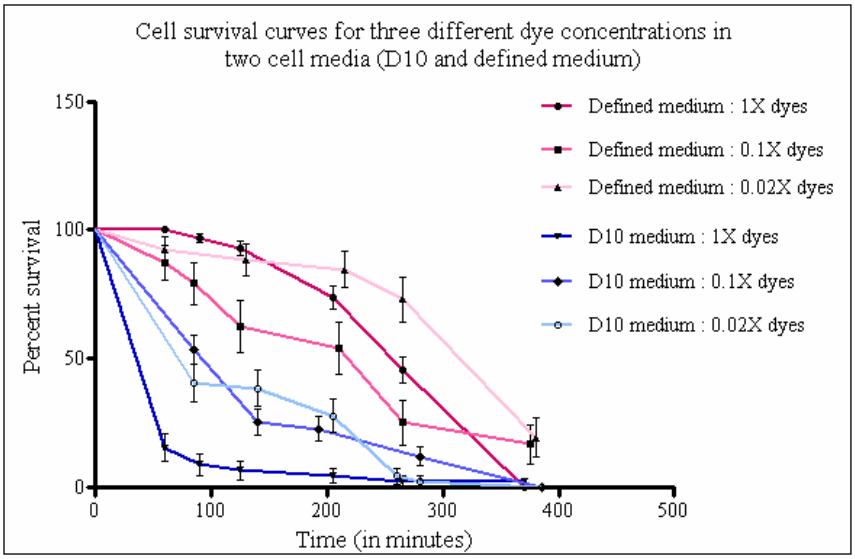


Figure 3.4: Graph of cell survival curves (percent survival Vs time) for three different dye concentrations in two cell media, for selection of the Optimum cell medium. Kaplan Meier survival curves for cells incubated in D10 and for those in the defined medium were plotted using the Graphpad Prism software Kaplan Meier analysis. Figure shows the cell survival curves for three dye concentrations (1X, 0.1X and 0.02X) for each of D10 and defined medium. All experiments were performed at 16X magnification and in optimum environmental conditions: 37$^{o}$C and 5%$CO_2$ conditions provided by the environmental chamber.

Cells in the defined medium on the other hand live longer and 50% of the cell population was dead by 220min, 200min and 300min for 1X, 0.1X and 0.02X dye concentration respectively. Clearly, cells in D10 died much earlier than those in the defined medium. The rapid death of cells in the D10 medium can be attributed to a chemical reaction between the cell dyes and the serum in this medium or between the cell dyes and the phenol red in the medium or both. The defined medium contains neither phenol red nor serum and therefore cells in the defined medium showed a higher survival rate. It was therefore used as the cell medium during all future cell experiments. Cells were cultured in D10 and then serum starved in defined medium 4 to 24 hours before the experiment so that they would get acclimatized to the medium and would stabilize before the experiment is conducted on them.

*3.2.2 Evaluation of environmental chamber performance*

The environmental chamber was constructed to maintain optimum temperature and humidity conditions for cells under experimentation. It was warmed for an hour to reach a temperature of 37$^{o}$C before the start of each experiment, so that the cells could be maintained at the optimum temperature required for their survival. The blood gas consisting of 5% $CO_2$ was released into the chamber at a flow rate of 1200±10 cc/min for maintaining the humidity and the pH of the cell medium. In order to evaluate the improved environmental conditions due to the use of the environmental chamber, cell survival experiments were performed at 5% $CO_2$ conditions at 33$^{o}$C and at 37$^{o}$C. To serve as a control, cell experiments were conducted at room temperature without any

temperature regulation and without any gas or humidity control. These experiments were first performed without any UV light and then with UVA light of intensity 3.65 $mW/cm^2$ at three above mentioned environmental conditions, namely,

- Category 1: at room temperature (RT) without any humidity control
- Category 2: at 33$^oC$ with humidity control and
- Category 3: at 37$^oC$ with humidity control

A 1X dye concentration in the defined medium was used. Graphpad Prism Statistical Analysis software was used to perform Kaplan Meier analysis and survival curves in each of these categories were plotted.

3.2.2.1 Comparison of survival curves in the absence of UVA light

Figure 3.5 shows the plot of the cell survival curves for cells in the environmental chamber in the absence of any UV light. It was observed that the percentage of cell survival dropped rapidly when the cells were at room temperature without any humidity control. In this case, 50% of the cells were dead by 87 minutes and all the cells were observed to die by about 150 minutes into the experiment. As the temperature was raised to 33$^oC$ and the cells were supplied with 5% $CO_2$, the cells showed a better survival rate with 50% of the population dead at 107 minutes and all the cells dead by 175 minutes. The cell survival time clearly increased with the temperature and the humidity control. When a survival experiment was performed at 37$^oC$ with humidity control, the cells appeared to live the longest amongst the three survival curves, and 50% of the cells lived until 150 minutes and the cells died by 208 minutes.

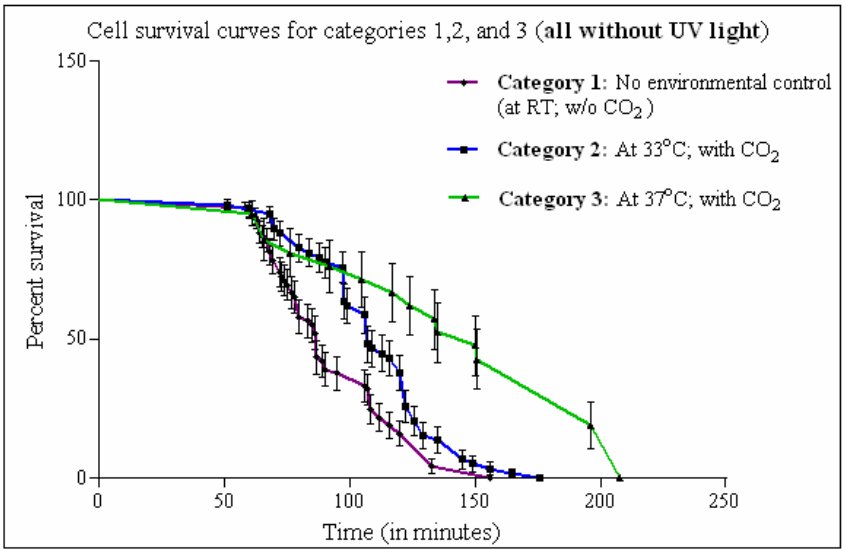


Figure 3.5: Graph of cell survival curves (percent survival Vs time) for three Environmental Conditions for Evaluating the Environmental Chamber Performance (in absence of UVA light). Kaplan Meier survival curves for the categories of (a) no environmental control (b) At 33°C with 5% $CO_2$ and (c) At 37°C with 5% $CO_2$ when no UVA light was illuminated on cells were plotted. All experiments were performed at 60X magnification and the dyes (DAPI and PI) were administered in defined medium at a 1X concentration.

Two statistical tests, the log-rank test and the Gehan-Breslow-Wilcoxon test were used to test the null hypothesis that there is no difference between the three cell populations in the probability that cell death occurs at any time point and thereby determine if the experimental curves are significantly different from one another. The null hypothesis was rejected if $p<0.05$. The Gehan-Breslow-Wilcoxon test gives more weight to deaths at early time points while the log-rank test gives equal weight to all time points. Also, the former is considered more suitable if several of the subjects were censored in the beginning. In our experiments, the occurrence of censored subjects was randomly distributed throughout the experiment duration. Therefore, both the tests were performed and reported for the data. Graphpad Prism software offers these two statistical tests to do curve comparison. These tests were applied to the data obtained to determine if any of these three curves were significantly different from one another.

Table 3.1 shows the 'p' values obtained by the Log-rank (Mantel-Cox test) and the Gehan-Breslow-Wilcoxon tests and also shows the median survival.

Table 3.1**:** Results of the Log-rank (Mantel-Cox) and the Gehan-Breslow-Wilcoxon statistical tests to compare cell survival curves at three different environmental conditions in order to evaluate the environmental chamber performance in the absence of UV light

| **Comparison of Survival Curves (UVA Absent)** | **RT and 37$^{o}$C** | **33$^{o}$C and 37$^{o}$C** |
|---|---|---|
| Categories compared | 1 and 3 | 2 and 3 |
| **Log-rank (Mantel-Cox) Test** | | |
| P value | < 0.0001 | < 0.0001 |
| P value summary | *** (extremely significant) | *** (extremely significant) |
| Are the survival curves sig different? | Yes | Yes |
| | | |
| **Gehan-Breslow-Wilcoxon Test** | | |
| P value | 0.0003 | 0.0075 |
| P value summary | *** (extremely significant) | ** (very significant) |
| Are the survival curves sig different? | Yes | Yes |
| | | |
| **Median survival** | | |
| Category1:RT and ***Category2: 33$^{o}$C*** | 87.00 | ***107.0*** |
| Category 3: 37$^{o}$C | 150.0 | 150.0 |

In both the curve comparisons, i.e. RT and 33$^{o}$C, and RT and 37$^{o}$C, it was observed that the p value was <0.0001 and all the curves were significantly different from each other by the Log-rank test. According to the Gehan- Breslow-Wilcoxon test analysis for the curve comparisons, the p values were 0.003 and 0.075 respectively, and the curves were significantly different too. Clearly, the improved survival of cells in category 3 over category 2 was because of the increase in temperature from 33$^{o}$C to 37$^{o}$C. Comparison of the curves for no environmental control (category 1) and optimum environmental control (category 3: 37$^{o}$C with humidity control) also yielded these two

curves to be significantly different. This difference clearly means that the temperature and the humidity control provided by the environmental chamber enabled longer survival rates of the cells and also maintained the cells at the most optimum environmental conditions.

3.2.2.2 Comparison of survival curves in the presence of UVA light

Another set of experiments was performed at the three environmental conditions stated above, this time in the presence of UVA intensity of 3.65 $mW/cm^2$. From figure 3.6, it is evident that the survival curves for cells at $33^oC$ and at $37^oC$ with humidity control are very similar and overlap over each other. Also, the median cell survival for both these conditions was 18 minutes and all the cells were dead by 25 minutes. Both the statistical tests applied the log-rank (Mantel-Cox) and the Gehan-Breslow-Wilcoxon test results deem these two curves not significantly different due to obtained p values of 0.3698 and 0.9438 respectively. Therefore, cells in category 2 and category 3 behaved exactly similar, in presence of UVA light. This indicates that although the temperature is increased from $33^oC$ to the optimum temperature required by mammalian cells ($37^oC$), the cells show no significant increase in their survival times. This observation is attributed to the presence of UVA light in this experiment because the same experiment when performed in absence of UVA light showed a significant improvement in the cell survival time.

Table 3.2 shows a summary of the statistical test analyses.

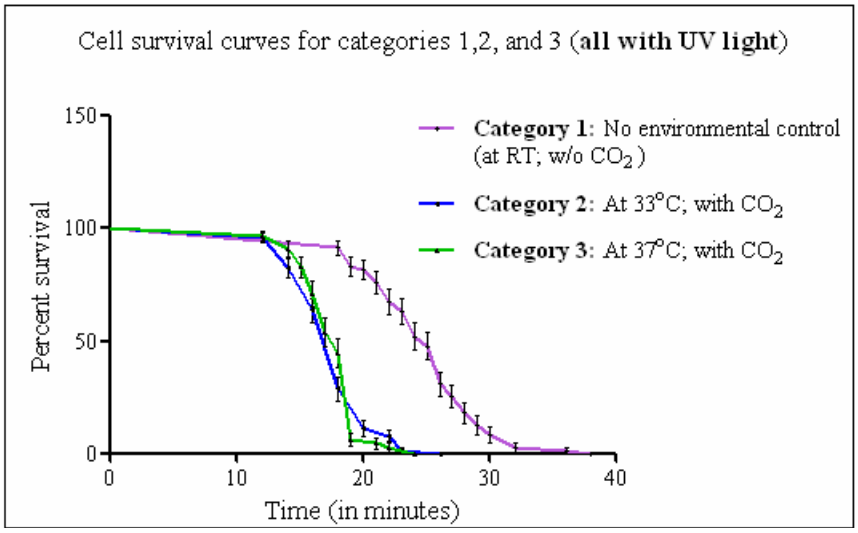


Figure 3.6: Graph of cell survival curves (percent survival Vs time) for three Environmental Conditions for evaluating the Environmental Chamber Performance (in presence of UVA light). Kaplan Meier survival curves for the categories of (a) no environmental control (b) At 33°C with 5% $CO_2$ and (c) At 37°C with 5% $CO_2$ in presence of UV light with intensity=3.65mW/cm$^2$ were plotted. All experiments were performed at 60X magnification and the dyes (DAPI and PI) were administered in defined medium at a 1X concentration.

Table 3.2**:** Results of the Log-rank (Mantel-Cox) and the Gehan-Breslow-Wilcoxon statistical tests to compare cell survival curves at three different environmental conditions in order to evaluate the environmental chamber performance in the presence of UV light

| **Comparison of Survival Curves (UVA present)** | **RT and 37°C** | **33°C and 37°C** |
|---|---|---|
| Categories compared | 1 and 3 | 2 and 3 |
| **Log-rank (Mantel-Cox) Test** | | |
| P value | < 0.0001 | 0.3698 |
| P value summary | *** (extremely significant) | ns (not significant) |
| Are the survival curves sig different? | Yes | No |
| | | |
| **Gehan-Breslow-Wilcoxon Test** | | |
| P value | < 0.0001 | 0.9438 |
| P value summary | *** (extremely significant) | ns (not significant) |
| Are the survival curves sig different? | Yes | No |
| | | |
| **Median survival** | | |
| Category1:RT and ***Category2: 33°C*** | 25.00 | ***18.00*** |
| Category 3: 37°C | 18.00 | 18.00 |

Comparison between the survival curves for cells at room temperature without 5% $CO_2$ and for cells at 37$^{o}$C with room temperature, yields that the curves are significantly different by both the log rank and the Gehan-Breslow-Wilcoxon tests. The most interesting observation in this set of data is that the cell survival was higher at room temperature (about 22$^{o}$C) than at the optimum cell temperature (37$^{o}$C) when UVA light is incident on all the cells. This may be due the surface heating caused by UVA light. Therefore, we conclude that UVA light affects the cells in a way such that an increase in the temperature decreases the cell survival rate.

The cells are observed to live longer at lower temperatures if UVA light is incident on them. However, higher cell survival does not always ensure an effective functioning of the enzyme systems within cells. Mammalian cells need to be maintained at 37$^{o}$C for maintaining their metabolism efficiently. Therefore, although lower temperature promotes higher cell survival in presence of UVA light, all further cell experiments with UVA light were performed at 37$^{o}$C.

*3.2.3 Comparison of cell incubator and environmental chamber*

In order to compare the performance of the engineered environmental chamber with that of a standard cell incubator, cell experiments were performed such that one set of cells was placed in the chamber and another in the incubator, and their survival rates were then compared. Two different concentrations of the dyes DAPI and propidium iodide (1X and 0.01X) in defined medium were used for each set of cells to compare the survival rates of cells in both conditions and thereby assess the chamber's performance.

Images were captured at 16X magnification so as to accommodate a higher number of cells in the camera capture window. As seen in figure 3.7, survival curves for cells in the chamber show that these cells at 1X, 0.1X dye concentration die by about 310 minutes. The cells that were placed in the incubator between two subsequent images die by around 400 minutes. The cell survival rates in both the chamber and the incubator are found to be similar, with the cells in the incubator surviving for slightly longer time.

Control experiments were also performed in which both the dyes were added to the cell medium and an image of the cells was captured. Immediately after this, the defined medium with the dyes was replaced by fresh defined medium devoid of any dyes. The cells were then placed in the incubator for two hours, when the medium was again replaced by defined medium with dyes and another cell image was captured. This ensured the minimum effect of the dyes on the cells and at the same time allowed for visualizing dead cells, if any. The curve representing this control experiment shows that almost all the cells survived for more than 19 hours. The last measurements were made at 19 hours, after which the experiments were terminated. The difference in the cell survival between this curve and all other curves in the figure, where the dyes stayed in the cell medium during the experiment proves that the presence of dyes indeed is the prime reason for cell death. The fluorescent dyes are chemicals and alter the survival characteristics of the cells.

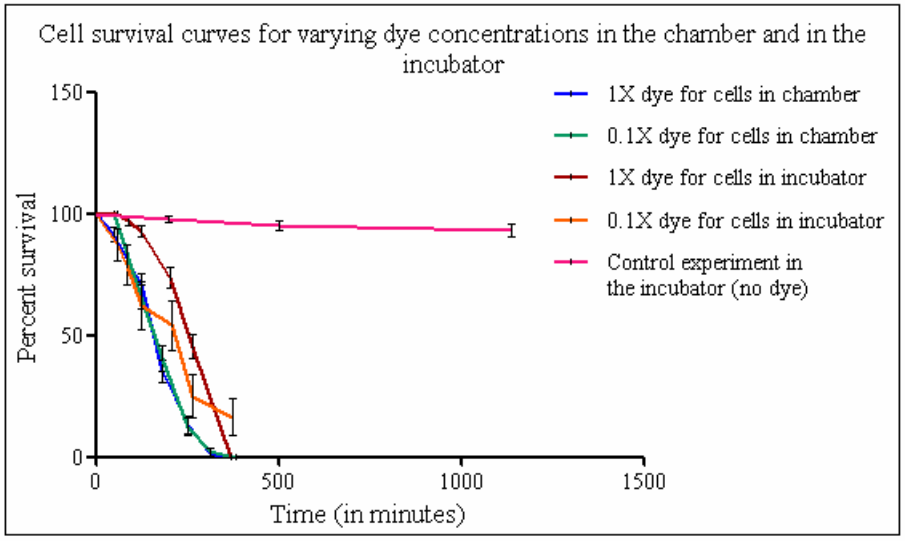


Figure 3.7: Graph of cell survival curves (percent survival Vs time) for varying dye concentrations in the environmental chamber and in the cell incubator for comparing the chamber with the incubator. All experiments were performed at 16X magnification and the dyes (DAPI and PI) were administered in defined medium at two different concentrations (1X and 0.1X). The cell incubator provided optimum environmental conditions of 37°C with 5% $CO_2$. The environmental chamber too was warmed to a temperature of 37°C and the cells were supplied with 5% $CO_2$ so as to compare the survival rates provided by the two instruments. No UV light illumination was used in these experiments. A control experiment with minimum amount of dyes was also performed in the incubator and was ended at 19 hours, as seen by the pink curve which shows almost complete cell survival.

This plot demonstrates that although some cells were placed in the standard cell incubator, which enables total cell survival, they still died at about 400minutes, just like the cells placed in the chamber. This suggests that the presence of dyes in both these sets of cells causes them to die, and that if the cell experiments could be performed without the dyes, the cell survival in the chamber would be better and maybe comparable to that in the incubator. However, the presence of the dyes in the medium is mandatory for the nature of experiments performed: to be able to detect cell death as soon as it occurs. Therefore, all further experiments have been performed with dyes unless explicitly mentioned. This experiment is instrumental in demonstrating that for the experimental condition of presence of the fluorescence dyes in the medium, the

chamber behaves like the cell incubator. The environmental chamber can therefore be considered a close match to a standard cell incubator.

*3.2.4 Determination of optimum dye concentration*

Fluorescent probes, DAPI and propidium iodide, were used to label the cell nuclei and cells which have lost their membrane integrity respectively. It was critical to select an optimum dye concentration for our experiments such that the dye concentration was low enough to be least toxic to the cells and at the same time high enough such that clear readout of the dye was possible. Four different concentrations of the dyes were administered in the cells with defined medium and images of cells were recorded every hour. In this experiment too, the images were captured at 16X magnification so as to accommodate a higher number of cells in the camera capture window and the temperature was adjusted to 37$^{o}$C with a 5%$CO_2$ humidity condition. Figure 3.8 shows the survival plot for the cells at all four dye concentrations. The curves for 1X, 0.1X and 0.02X seem to follow a trend where the cell survival slightly increases as the concentration decreases.

The curve representing the 0.005X dye concentration demonstrates that all the cells die around the cell death times of all other dye concentrations. However, this curve seems to reach its 50% survival much before even the 1X curve which would mean that at a lower concentration of 0.005X, the cells died at a faster rate than at a higher concentration (1X, 0.1X and 0.02X). The reason for this inconsistent data for the

0.005X dye concentration curve was that the dyes were not clearly visible at such a low concentration and this led to errors in the dead cell counting procedure.

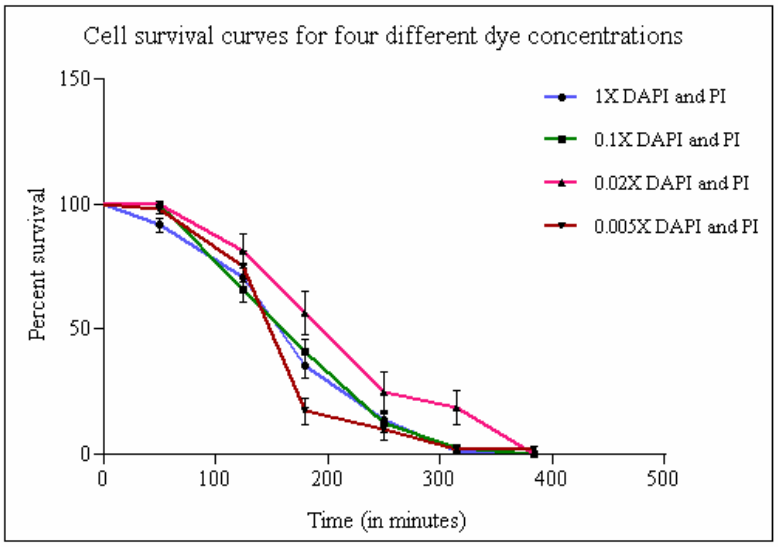


Figure 3.8: Graph of cell survival curves (percent survival Vs time) for four different dye concentrations to determine the optimum dye concentration. Kaplan Meier cell survival curves are shown when the dyes (DAPI and PI) were administered in defined medium at four different concentrations (1X, 0.1X, 0.02X and 0.005X). The cells were placed in the environmental chamber with optimum environmental conditions of 37°C with 5% $CO_2$ and all experiments were performed at 16X magnification. No UV light illumination was used in these experiments.

Since the 0.005X dye concentration was demonstrated to be low enough to produce inconsistent data, the optimum dye concentration was to be selected among 1X, 0.1X and the 0.02X. In order to ensure the least dye toxicity to the cells and a sufficient readout of the dye, the 0.1X was selected as the optimum dye concentration. However, at this concentration, the dyes underwent photobleaching during the course of a few initial cell experiments. Therefore 1X was selected as the optimum dye concentration for all further cell experiments.

# CHAPTER 4

# RESULTS AND DISCUSSION

In this chapter, experimental results including the selective cell manipulation experiments, analysis of differential organelle sensitivities to UVA light, determination of cytoplasmic membrane retraction velocity and other partial cell analysis are presented and discussed. Specific experimental conditions for each set of experiments are presented in each section.

## 4.1 Digital mask dependent cell manipulation

Once the nanopatterning system parameters were optimized for their performance, the nanopatterning system was used to demonstrate selective cellular manipulation. The dyes DAPI and propidium iodide were added to the defined medium in the 1X concentration, the temperature inside the chamber was maintained at 37$^{o}$C and the blood gas mixture was supplied to the cells at a flow rate of 1200±10 cc/minute. Various patterns of UVA light were projected on a monolayer of cells, and pattern dependent manipulation of cells was achieved.

### *4.1.1 UVA pattern: left half of the DMD screen*

A dish with adhered cells was placed in the environmental chamber to investigate the cell response to total UVA illumination. In this experiment, UVA light

was projected on the entire left half of the pattern window by drawing a mask as shown in Figure 4.1(a). The cells in the illuminated region are visualized by DAPI excited due to the UV light, while those outside the pattern are not and are therefore not visible in Figure 4.1(a). The cells lying below the left UV half of the pattern window, were continuously illuminated with UVA light of intensity = 3.65 mW/cm2, while the cells in the right half were masked from any UV light. Figure 4.1 (b), (c), (d) , (e) and (f) below show a series of pictures captured at 12min, 25min, 30min, 46min and 62min respectively after the start of the experiment show the entry of the dead cell dye only into those cells that were exposed to ultraviolet irradiation. It was observed that cells on the right side that was masked from the UVA light did not uptake the dead cell marker red dye and remain alive until about 30minutes. In figure 4.1(d), a definite half and half pattern is visible where all the UVA targeted cells on the left half appear red, while the ones on the right side appear blue. Some cells were located at the edge of the UVA pattern and as a result may have only a part of their cell body illuminated with the UVA light. In case of such cells, propidium iodide was seen entering the cells from the illuminated side suggesting that local UVA illumination can induce local damage in cells which may spread into the entire cell with time. (Fig 4.1(e))

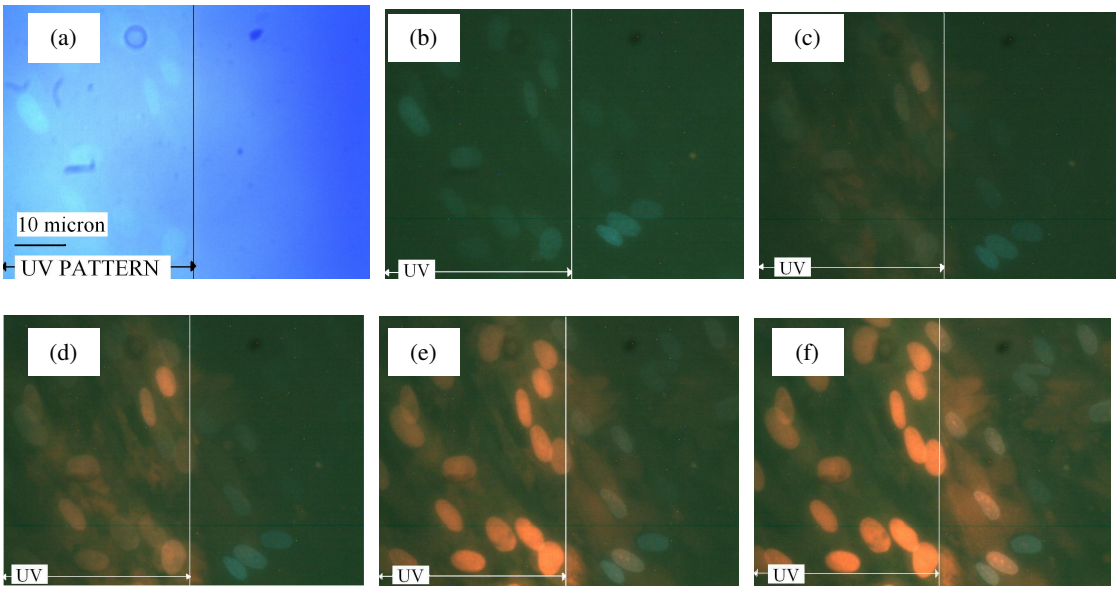


Figure 4.1: Digital mask dependent cell manipulation: Left half of the DMD screen as the UVA pattern. Figure (a) shows UV light projected from the left half of the DMD screen causing excitation of the DAPI stain in the nuclei in this area. No DAPI stained nuclei are visible in the right side of the image because DAPI stain remained unexcited due to the lack of excitory UV light. The pattern of UV light is marked with a line across all images. Figures (b), (c), (d), (e) and (f) are images captured at 12min, 25min, 30min, 45min and 62 min into the experiment respectively, using the triple passband filter cube that enables visualization of both DAPI and PI. Damaged or dead cells were marked red by PI, while the viable cells were marked blue by DAPI. Maximum cell damage occurs in the cells positioned at the site of the UV illumination. This experiment was performed at 37$^{o}$C with 5% $CO_2$ at 60X magnification. The dyes were administered at a 1X concentration in defined medium and UV intensity =3.65mw/cm$^2$ was used. (Scale bar:10 micron )

Although propidium iodide is seen staining the entire cell body at the start, once it binds to the DNA in the nucleus, its fluorescence intensity increases many fold and all of the propidium iodide appears to have entered the nuclear area. A very little amount of the red propidium iodide is then visible in the cell cytoplasm as the experiment nears its end. (visible in 4.1(d) to 4.1(f)). Eventually some of the completely non-illuminated cells on the right side of the field of view also start dying. The reason for this may be that these non-illuminated cells were in contact with the illuminated cells that are undergoing damage, and this proximity to dead damaged cells may induce communication between these two cell categories. The above images clearly show the

penetration of the dead cell marker propidium iodide in the UV targeted cells and thus demonstrate selective manipulation of cells by projecting UV light masks on those cells.

### *4.1.2 UVA pattern: Selective cell nuclei envelopes*

In another demonstration of selective cell manipulation, an experiment was performed where four randomly selected cell nuclei were locally illuminated using a digital mask enveloping each of these nuclei. Images from the experiment taken at 0 min, 6 min, 20min and 36min are shown below in figure 4.2.

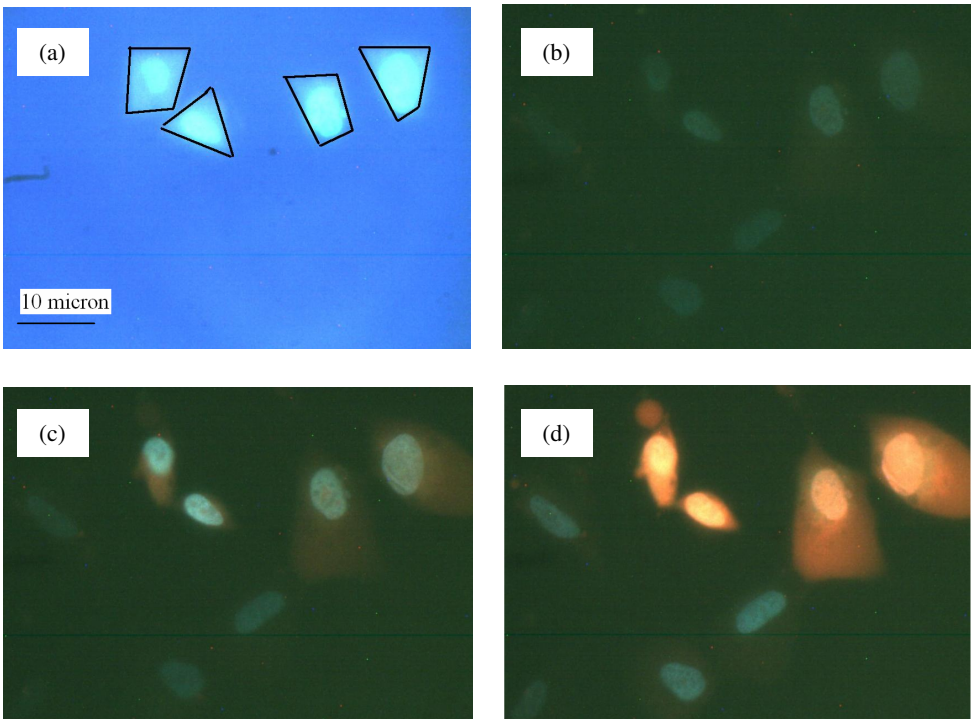


Figure 4.2: Digital mask dependent cell manipulation: Envelope around selective cell nuclei as the UVA pattern. Figure (a) shows four cell nuclei being illuminated by patterns of UVA drawn around them, depicted by black marks. Note that this experiment is not an example of specific nucleus illumination since a portion of the cytoplasm too was illuminated by UVA light, in this case. Also seen are few other cell nuclei without any illumination. Figures (b), (c), and (d) are images captured at 6min, 20min, and 36min from the start of the experiment respectively, using the triple passband filter cube that enables visualization of both DAPI and PI. In figures (c) and (d), penetration of PI into the four cells whose nuclei were illuminated with UVA light, is observed. This indicates death of these cells relative to the non illuminated cells. This experiment was performed at 37$^{o}$C with 5% $CO_2$ at 60X magnification. The dyes were administered at a 1X concentration in defined medium and UV intensity =3.65mw/cm$^2$ was used. (Scale Bar: 10 micron)

It was observed that only the illuminated four cell nuclei undergo damage before any other cell in the field of view. At 20min, propidium iodide is seen entering the cells with the targeted four nuclei. By 36min, propidium iodide enters these cells completely and then binds to the DNA in the nucleus as explained earlier. The ability to locally manipulate selective cell nuclei was first demonstrated in this experiment.

### *4.1.3 UVA pattern: Rectangular block in the center of the DMD screen*

For the purpose of demonstrating the manipulation of cells as well as partial cells by projecting a specific UVA mask on the cells, a rectangular block of UVA light was projected as the digital mask from the DMD screen. Figure 4.3 (a) shows the central rectangular pattern illuminating cell nuclei stained with the nuclear stain DAPI. Cells in the illuminated region are visualized by the excitation of the DAPI dye while those outside the UVA pattern are not visible. This demonstrates that the UVA scatter is low enough to not excite the DAPI stain in the non-illuminated areas. Some of the nuclei are partially illuminated by the pattern. Figure 4.3 (b) shows the cells at 38min of UVA illumination.

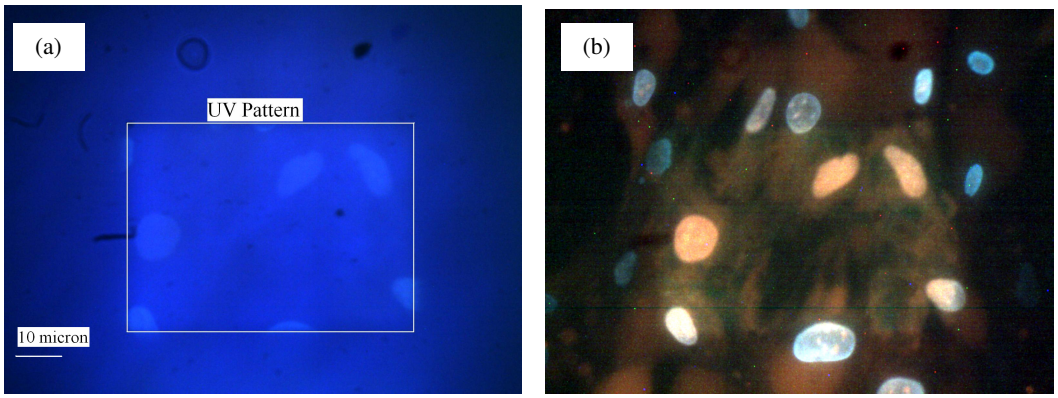


Figure 4.3: Digital mask dependent cell manipulation: Rectangular block in the center of the DMD screen as the UVA pattern. The projected UVA pattern in this experiment was a rectangular block in the center of the pattern window, as shown in figure (a). The cell nuclei in the illuminated region are visualized by DAPI excited due to the UVA light, while those outside the pattern are not and are therefore not visible in the figure. Figure (b) shows the image taken at 38 min of continuous UV illumination. This experiment was performed at 37$^{o}$C with 5% $CO_2$ at 60X magnification. The dyes were administered at a 1X concentration in defined medium and UVA intensity =3.65mw/cm$^2$ was used.

The three nuclei that were totally illuminated by UVA light appear completely red indicating cell death. Other nuclei that were partially illuminated show interesting morphologies. These nuclei appear to have up taken the dead cell dye from the side they were illuminated and therefore appear as partial red and partial blue colored nuclei. This observation suggests that cell nuclei can have various levels of damage depending on which part of the nucleus was exposed to the harmful UVA light. All the nuclei outside the square pattern remained unexposed, however they do show some amount of the red propidium iodide in them over time. The possible reason for this could be contact between the illuminated and the non illuminated cells, again suggesting cell communication leading to some damage in the masked cells. Also, since only the cell nuclei are visible in these images and the whole cell bodies are not, it is possible that a portion of these non illuminated cells was in fact under illumination and responsible for some of the damage caused in them.

## 4.2 Evaluation of relative sensitivities of nucleus and cytoplasm to UVA light

The capability of the nanopatterning array system to selectively illuminate desired portions of cells at a submicron scale allows us to target specific organelles and investigate the sensitivity of these organelles to ultraviolet light. Using the nanopatterning array system to perform local UVA illumination of organelles can also help determine the independent roles of cell organelles like the nucleus and the cytoplasm in contributing to cell death due to UVA damage. For all these experiments, the dyes DAPI and propidium iodide were added to the defined medium in the 1X concentration, the temperature inside the chamber was maintained at 37$^{o}$C and the blood gas mixture was supplied to the cells at a flow rate of 1200±10 cc/minute.

### *4.2.1 Entire cell illumination*

In order to serve as a standard in the measurement of organelle sensitivities, entire cell illumination was performed at varying UVA intensities. At extremely low UVA intensities, membrane blebbing, which is bubble formation on the membrane surface as a result of UV induced damage, was observed in some cells. In many cases, sites within the cell nucleus appeared to turn red before the rest of the nucleus indicating that certain areas within the nucleus maybe more UVA sensitive than others. Eventually, propidium iodide entered the entire nucleus uniformly and the amount of the dye in the cytoplasm appeared to reduce. The number of dead cells was counted at every image capture and cell survival curves for all intensities were plotted using the Kaplan-Meier analysis (Graphpad Prism Statistical Analysis software). A control

experiment with no UV light illumination to the cells was also performed. Figure 4.4 shows the survival analysis for entire cell UVA illumination for varying UVA intensities.

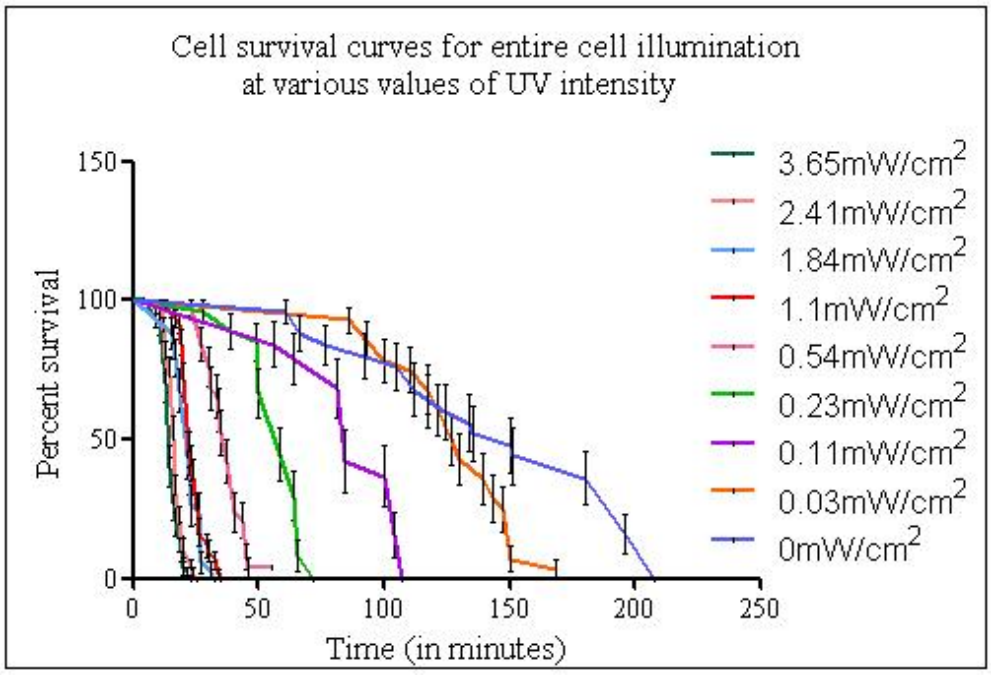


Figure 4.4: Graph of cell survival curves (percent survival Vs time) for entire cell illumination at various values of UVA intensity. These curves were obtained after performing Kaplan Meier analysis using Graphpad Prism statistical analysis software, on this experimental data. It is observed that the cell survival time decreases with an increase in the intensity of the UVA light used. However, any increase in the intensity beyond 2.41mW/cm$^2$, does not reduce the cell survival times significantly as seen by overlapping survival curves for 3.65mW/cm$^2$ and 2.41mW/cm$^2$. On the right side, the legend for the various UV intensities is presented. All the experiments in this group were performed at 37$^o$C with 5% $CO_2$ at 60X magnification. The dyes were administered at a 1X concentration in defined medium.

It was observed that as the UVA intensity was increased from 0mW/cm$^2$ to 1.1mW/cm$^2$, cell survival times decreased considerably. With any further increase in the UVA intensity, the cell survival times dropped insignificantly, indicating saturation. At maximum intensity of UVA light, all the cells died by about 18minutes. For the control experiment, without any UV light, the survival curve (shown in blue color), the cells died by 208minutes.

*4.2.2 Local UVA irradiation of the nucleus*

In order to determine the independent role of a UVA irradiated nucleus in causing cell death, cell nuclei were locally irradiated. For doing this, a picture of the cells was captured and was modified in Adobe Photoshop using the 'Autolevels' function for better visualization of cells as shown in figure 4.5 (a). This image was then opened using the IDL program (discussed in chapter 2), which allowed the user to selectively mark portions of cells and create a digital mask. Such a mask to specifically mark the cell nuclei was drawn (figure 4.2(b)) and was projected from the DMD screen such that only the cell nuclei were illuminated by UVA light and all other portions of the cell body remained masked. Figures 4.5 (c) shows an image of the projected UVA mask as seen by the camera and (d) shows the UVA pattern overlapping with the cells in the brightfield mode respectively. Images were captured every 5minutes after the start of the experiment.

In some of the local nuclei illumination experiments, cell membrane blebbing, which is a sign of UV induced damage, was observed only at high UVA intensities unlike the entire cell illumination where it occurred at extremely low intensities. Also, the cells condensed and shriveled up towards the end of the experiment in such a way that the digital mask would cease to illuminate the nucleus specifically. A portion of the pattern would now illuminate the cytoplasm as well, which was undesirable. In such cases, a new mask was drawn to accommodate the shift in the cell position.

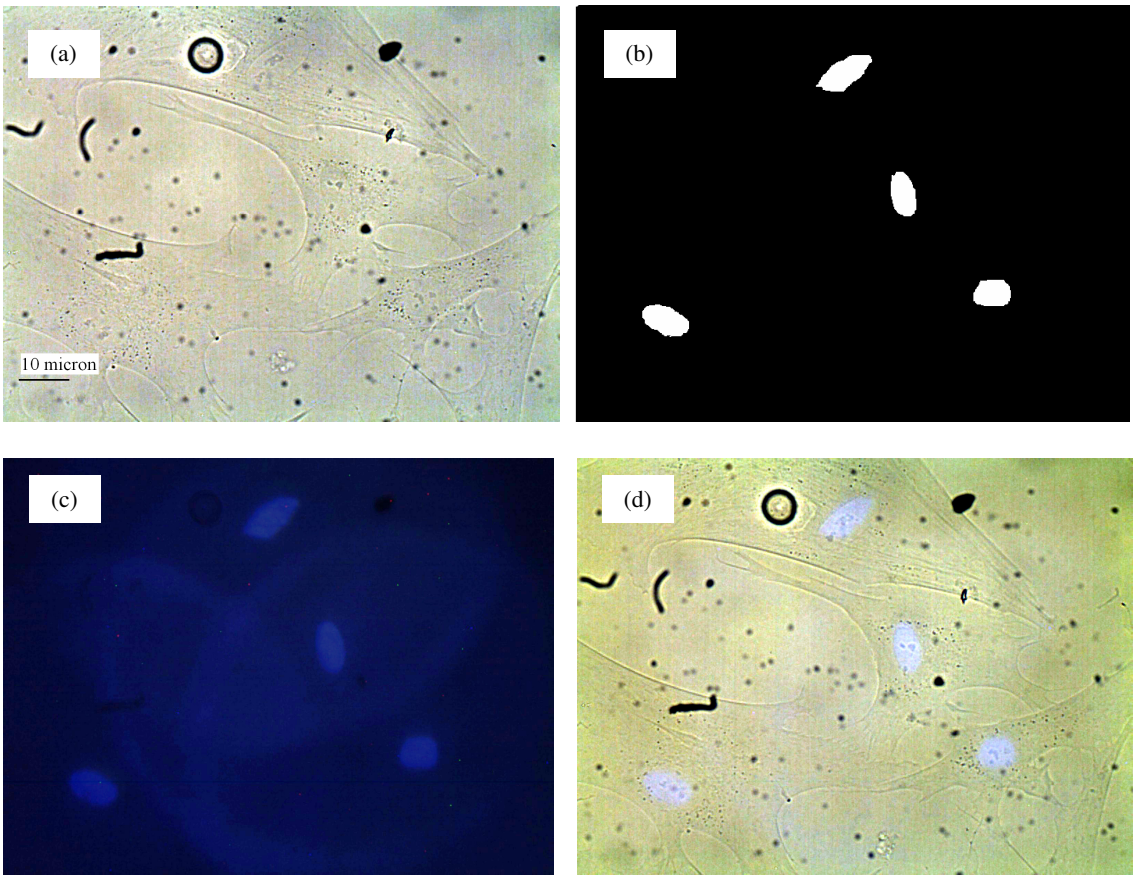


Figure 4.5: Demonstration of local nucleus illumination. Figure (a) shows a brightfield image of the cells captured at 60X magnification, was modified by performing 'Autolevels' in Adobe Photoshop for better visualization of cells. Figure (b) shows digital mask projected from the DMD screen, resized to the capture window dimensions. The mask is seen to specifically illuminate the cell nuclei. Seen in figure (c) is the actual UVA light pattern seen in the camera capture window. Figure (d) shows the cells in the brightfield mode with the overlaying locally illuminated cell nuclei pattern. (Scale bar: 10 micron for all figures)

Local nucleus illumination experiments were performed at various UVA intensities ranging from 0 to 3.65mW/cm$^2$. Survival Analysis was performed on this data and the plot is shown in Figure 4.6.

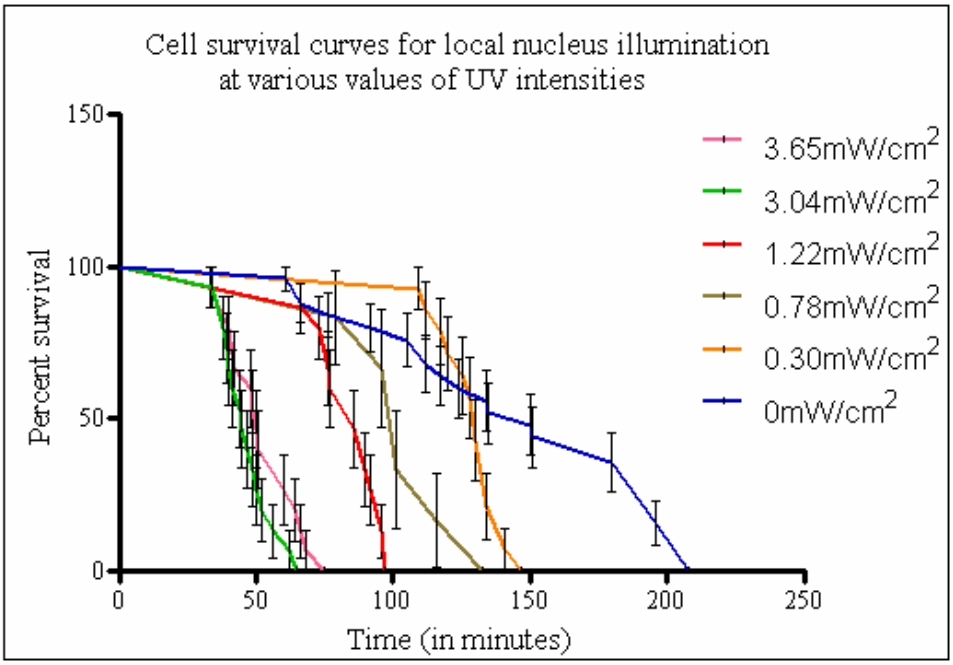


Figure 4.6: Graph of cell survival curves (percent survival Vs time) for local nucleus illumination at various values of UVA intensity. Figure shows a series of cell survival curves for local nucleus illumination experiments performed at various UVA intensities. These curves were obtained after performing Kaplan Meier analysis using Graphpad Prism statistical analysis software, on this experimental data. It is observed that the cell survival time decreases with an increase in the intensity of the UVA light used. On the right side, the legend for the various UVA intensities is presented. All the experiments in this group were performed at 37°C with 5% $CO_2$ at 60X magnification. The dyes were administered at a 1X concentration in defined medium.

From the plot, it can be seen that the survival curves corresponding to UVA intensities of 3.65 and 3.04 mW/cm$^2$ are similar. All other curves for experimental intensities are significantly different. It is also seen that for an intensity of 3.65mW/cm$^2$, all the cells died by about 75 minutes when only the nuclei of the cells were illuminated. This time is much higher than the time required for all the cells in the entire cell illumination category to die, which is only 18 minutes. (Figure 4.4)

*4.2.3 Local UVA irradiation of the cytoplasm*

After the local nucleus illumination experiments, only the cell cytoplasm was locally illuminated at various UVA intensities with the nuclei masked. In a procedure similar to the local nucleus illumination experiments, a picture of the cells was captured and was modified in Adobe Photoshop using the 'Autolevels' function for better visualization of cells as shown in figure 4.7 (a). This image was then opened using the IDL program (discussed in chapter 2), which allowed the user to selectively mark portions of cells and create a digital mask. Such a mask to specifically mark the cell cytoplasm was drawn (figure 4.7(b)) and was projected from the DMD screen such that only the cell cytoplasm were illuminated by UVA light and all other portions of the cell body remained masked. Figures 4.7 (c) shows an image of the projected UVA mask as seen by the camera and (d) shows the UVA pattern overlapping with the cells in the brightfield mode respectively. Images were captured every 5minutes after the start of the experiment.

In almost all the local cytoplasm experiments, the cells rapidly shrunk in volume and moved from their original position such that the cytoplasm pattern no longer only illuminated the cytoplasm. Unlike the local nucleus experiments where this occurred only when the experiment neared its end, in local cytoplasm experiments the cells immediately responded by moving and continued to do so throughout the course of the experiment. Due to the shift in the cell's position, the original digital mask would not perfectly mask the cell nuclei and illuminate the cytoplasm anymore. In such cases, a new mask was drawn to accommodate the shift in the cell position and continue to

illuminate only the cytoplasm. This cell displacement due to UVA illumination was much more pronounced in the local cytoplasm illumination experiments than in the local nucleus illumination experiments and required constant adjustments in response to the cell's movement.

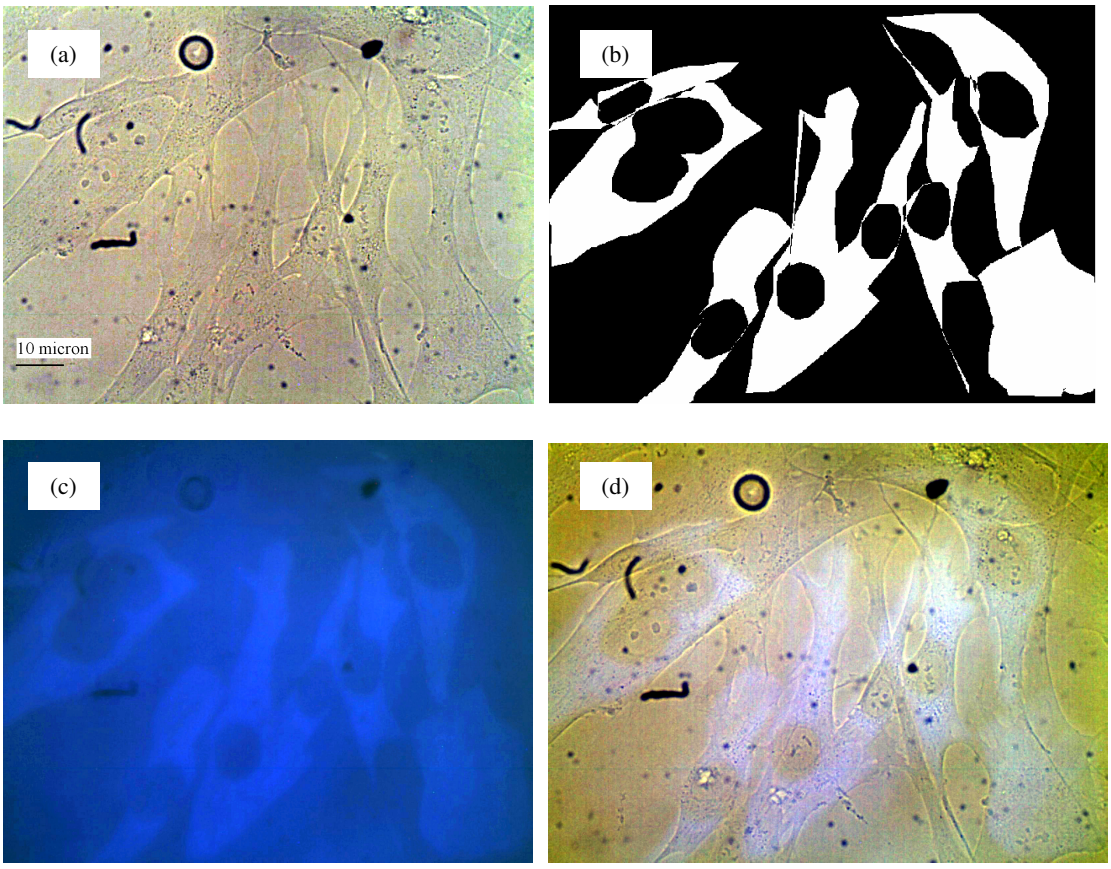


Figure 4.7: Demonstration of local cytoplasm illumination. Figure(a) shows a brightfield image of the cells captured at 60X magnification, was modified by performing 'Autolevels' in Adobe Photoshop for better visualization of cells. Figure (b) shows digital mask projected from the DMD screen, resized to the capture window dimensions. The mask is seen to specifically illuminate the cytoplasm of the cells. Seen in figure (c) is the actual UVA light pattern seen in the camera capture window. Figure (d) shows the cells in the brightfield mode with the overlaying locally illuminated cytoplasm pattern. (Scale bar: 10 micron for all figures)

Figure 4.8 shows the survival plot for local cytoplasm illumination. From the survival plot, it is seen that for an intensity of 3.65mW/cm$^2$, all the cells died by 38minutes when only the cytoplasm of the cells was illuminated. It is observed that in local cytoplasm

illumination experiments, the cell death occurs more rapidly than in local nucleus illumination experiments and slower than in entire cell illumination experiments at the same intensity.

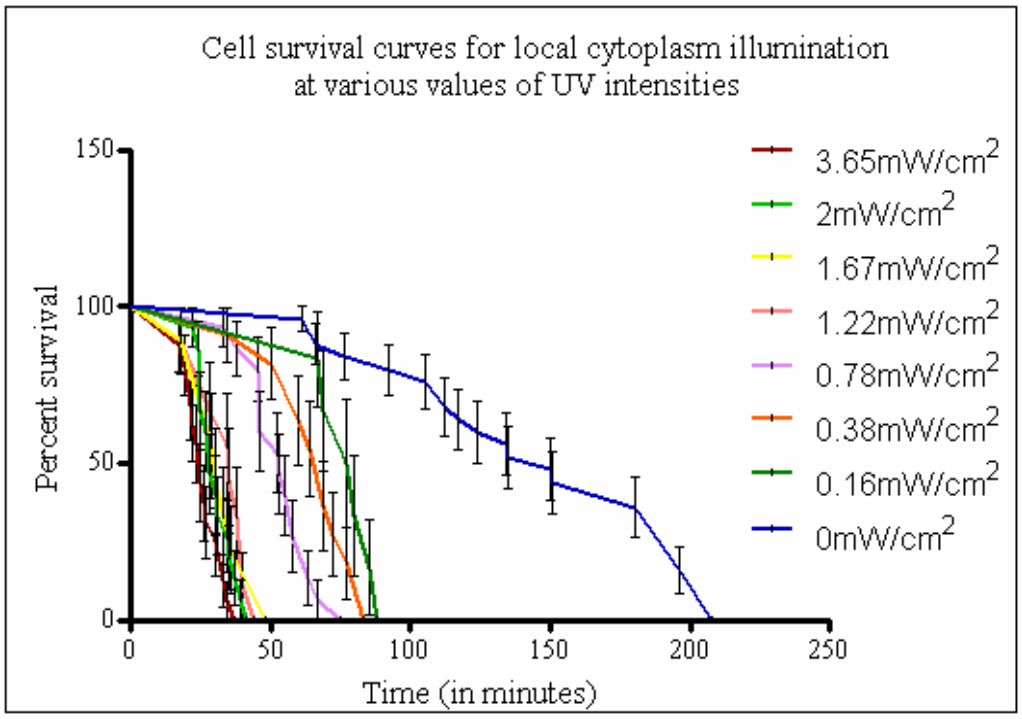


Figure 4.8: Graph of cell survival curves (percent survival Vs time) for local cytoplasm illumination at various values of UVA intensity. These curves were obtained after performing Kaplan Meier analysis using Graphpad Prism statistical analysis software, on this experimental data. It is observed that the cell survival time decreases with an increase in the intensity of the UV light used. Any increase in the intensity beyond 1.22mW/cm$^2$, does not reduce the cell survival times significantly as seen by overlapping survival curves for 3.65mW/cm$^2$, 2mW/cm$^2$, 1.67mW/cm$^2$ and 1.22mW/cm$^2$. On the right side, the legend for the various UVA intensities is presented. All the experiments in this group were performed at 37$^o$C with 5% $CO_2$ at 60X magnification. The dyes were administered at a 1X concentration in defined medium.

As the intensity increases from 0.16mW/cm$^2$ to 1.22mW/cm$^2$, the cell survival times keep decreasing. However, once the intensity is increased above 1.22mW/cm$^2$, the cell survival times do not decrease significantly. Also, it can be seen that the survival curves for intensities 3.65mW/cm$^2$, 2mW/cm$^2$, 1.67mW/cm$^2$ and 1.22mW/cm$^2$, are very similar. Similar trend was observed for entire cell illumination experiments, where any

increase in the intensity beyond 1.1mW/cm$^2$, caused very little decrease in the cell survival time.

*4.2.4 Analysis of local UVA illumination data*

After obtaining the survival plots for entire cell illumination, local nucleus illumination and local cytoplasm illumination, a dosage plot was drawn shown in Figure 4.9. The exposure time required to reach lethal dose for 50% ($LD_{50}$) of the cell population was calculated for each of the experimental intensities. All the UVA doses were calculated as a product of each UV intensity and its corresponding time to reach the $LD_{50}$ state. This value was also multiplied by a factor of 0.06 to convert the dose in J/cm$^2$.All the data points for each of the entire cell illumination, local nucleus illumination and local cytoplasm illumination categories were plotted with time to reach the median lethal dose ($LD_{50}$) on the Y axis and the corresponding UVA dose (in J/cm$^2$) on the X axis and are shown as yellow, blue and pink points respectively. These data points for each type of illumination were then fitted to a standard exponential trendline. The squares of correlation coefficients obtained for entire cell illumination, local nucleus illumination and local cytoplasm illumination were 0.9321, 0.9043, and 0.8695 respectively. The equations for the three sets of data points are displayed on the graph in Figure 4.9 which shows the dosage plot. This dosage plot shows that the site of illumination in the cell indeed determines the cell's response and its death. The data points also clearly demonstrate that the UVA induces a higher level of rapid damage in the cell cytoplasm relative to its nucleus. In order to find the relative sensitivity of each

component to UVA, the average time to reach $LD_{50}$ was calculated from the equation for each category of illumination. For example, for the entire cell illumination group, the curve equation is $y=152.55e^{-1.6133x}$. Therefore from the plot in figure 4.9, the UVA dose corresponding to 76min (=152/2) is found to be 0.4J/cm$^2$. Similarly, the UV doses corresponding to the average time required for reaching $LD_{50}$ state for the local cytoplasm and local nucleus categories are 2.2 J/cm$^2$ and 6.4J/cm$^2$. These values clearly demonstrate that the cytoplasm is about three times more sensitive to UVA radiation than the nucleus.

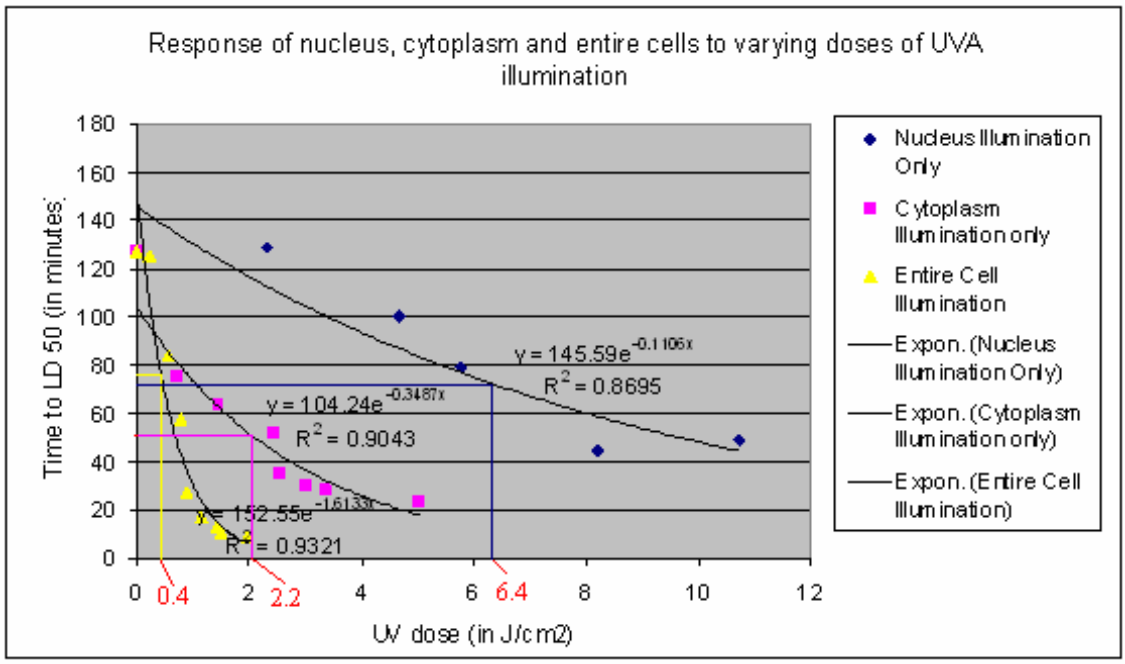


Figure 4.9: Graph of time to $LD_{50}$ Vs UV dose to demonstrate the response of nucleus, cytoplasm and entire cells to varying doses of UVA light. UVA intensity dependent cell survival curves for entire cell, nucleus only, cytoplasm only illumination were obtained as shown in figures 4.4, 4.6 and 4.8. The $LD_{50}$ time for each curve in each of these figures was obtained. UVA dose for each survival curve was calculated as a product of the UVA intensity used and the $LD_{50}$ time for that curve. In this graph, the LD50 times for all the data points were plotted versus the corresponding UV doses. A trendline was drawn for all data points in each of the three groups, and the three equations are displayed on the graph. Also, shown are three $R^2$ values, for all three groups.

Data was collected for about 250 cells in each illumination category. Approximately 25 experiments were performed for each of the local nucleus, local cytoplasm and entire cell illumination groups. On an average, data for about 10 cells was collected from each experiment.

*4.2.5 Discussion*

It is generally accepted that DNA is the primary target for the damaging effects of the UV radiation due to its UV absorption characteristics. However, UV radiation can also have a detrimental effect on other subcellular components in the cellular cytoplasm and the membranes depending on the wavelengths of UV radiation used. In order to identify the prime molecular targets of the UVA radiation and understand their independent roles in contributing to UVA induced damage, we targeted the cell nucleus and the cell cytoplasm individually. This data was then compared to the entire cell illumination and a control group of no UVA illumination. The cells illuminated entirely died most rapidly due to combined organelle damage caused in all parts of the cells. In cells with local UVA irradiation of the nucleus alone, cells lived longer than the completely targeted cells. The cytoplasm was masked in this group of cells and therefore no UVA induced cytoplasmic damage occurred. The difference in the exposure times to reach the $LD_{50}$ in these two groups of cells indicates that the cytoplasm is indeed a target for UVA induced damage and contributes significantly to cell death along with the nuclear damage. The data for the cytoplasm specific illumination suggests that these cells were subject to cell death faster than those that

were under nucleus specific UVA radiation and slower than the entire cell illumination. When the nucleus was masked, the cells died faster than when the cytoplasm was masked, suggesting that the cytoplasm contributes to a higher level toward UVA induced damage in a cell than the nucleus does.

The cell cytoplasm is a highly organized network consisting of cytoskeletal filaments, lysosomes, mitochondria, ribosomes, proteins and a variety of other membrane bound organelles tethered in a highly viscous gel [81]. Therefore, any cytoplasmic damage can be considered to be a combination of damage caused to these cytoplasmic components. Damage to the cytoskeletal microtubules due to the action of UVA and UVB has been previously reported by Zamansky et al. [82]. The cytoskeleton is responsible for providing a distinct shape and structure to the cell. UVA illumination of the cytoskeleton results in disruption of the microtubules, microfilaments, the intermediate filaments and other fibers in cells. When human cells receive different doses of UV, the integrity of the cytoskeleton is lost, cells lose their functionality, and they tend to enter apoptosis [83]. This might be the reason why the fibroblast cells were observed to shrivel rapidly when the cytoplasm was targeted with UV light. In case of local cytoplasm illumination experiments, this cytoskeletal damage made it necessary to continuously map the cytoplasm location so as to not illuminate the nucleus accidentally. Complete cell shrinkage was also observed in local nucleus illuminated experiments but that is attributed to the UV induced apoptosis due to nuclear damage and not cytoskeletal damage. Along with disruption of the microtubules and the microfilaments, UVA and UVB irradiation has also been reported to induce a wide

spectrum of other micromorphological changes like retraction and rounding up of various cell types, membrane ruffling, changes in the number and size of microvilli, retraction of pseudopods and development of blebs on the cell surfaces [84-86]. Membrane blebbing has been long considered as a sign of cell injury and was observed frequently in local cytoplasm experiments. Membrane blebbing due to local nucleus illumination was observed at extremely high intensities only, which indicates that a higher dose of UVA radiation is required for apoptosis to occur by local nucleus illumination. Another interesting UVA induced morphological change observed in all the illumination experiments was the occurrence of bright spots in the cytoplasm around the nucleus. This data was consistent with Somosy et al. [86], who reported the formation of similar bright spots in the cytoplasm around the nucleus in fibroblast cells in response to X-ray radiation. These structures were identified as the proteins P58 bound to the Golgi apparatus, which became scattered in the cytoplasm as an effect of the radiation.

Many study groups have reported findings suggesting the nature of cytoplasmic damage induced by UVA radiation. Beer et al. [87] have previously demonstrated that UVA can induce non-nuclear damage and cell death in three strains of mouse lymphoma cells. In their results, they observed that UVA has a high potential to cause damage to the cytoplasm, organelles and the cell membrane; and lysis in irradiated cells and that in all three strains of these cells, the plasma membrane and the cytoplasmic organelles were much more sensitive to UVA (340-400nm) than to UVB or UVC radiation. UVA has also been demonstrated to cause oxidative damage and generation

of reactive oxygen species at several cytoplasmic sites such as the mitochondrial membrane [61], microsomal membrane [69], lysosomes [69], proteins [88] and the cell membrane [68, 88-90]. In a first report of identifying cellular RNA as a cytoplasmic target for photooxidation damage due to UVA radiation, Wamer et al. [91] have demonstrated that the extent of oxidative damage caused to RNA in the cytoplasm of the fibroblast cell is in fact higher than that to the DNA in the cell nucleus. These findings suggest that there might be cytoplasm specific chromophores that serve as targets for UVA absorption and lead to a higher UVA induced damage in the cytoplasm of cells [87]. The absorption spectra of chromophores found in the cytoplasm will determine the sensitivity of the cytoplasm to various wavelengths. Cytoplasmic chromophores for all wavelengths are still unknown [92], however several cytoplasmic chromophores for UVB have been identified, such as proteins like melanin, tyrosine and tryptophan [64-65, 93]. Chromophores absorbing UVA radiation on the other hand are under still investigation [91]. Several groups have proposed chromophores for UVA such as the enzymes NADH and NADPH [65, 68, 70, and 87], porphyrins [65, 68, and 70], riboflavin [65, 87] and other flavins [68]; all of which are located in the cell cytoplasm and the cell membrane. Tyrell et al. [69] also reported the role of free heme and iron molecules, which are released from heme-containing proteins on the microsomal membrane into the cytoplasm in response to UVA radiation, as photosensitizers for UVA. Our experimental data is based on the UV illumination from 350nm to 500nm which comprises mainly of UVA radiation and some visible light, and indicates that the sensitivity of the cytoplasm to UVA and that the photobiological

consequences initiated as a result of local cytoplasmic illumination are greater and more significant than that of the local nucleus illumination. We thus conclude that the cytoplasm is three times more sensitive to UVA absorption than the nucleus is and that the cell response to UVA light depends on the site of illumination in the cell.

## 4.3 Determination of the cytoplasmic membrane velocity in response to its local UVA illumination

Inspired by the results in which the cell morphology was seen to shrink and also that the cells would move to apparently avoid UVA illumination, experiments were devised to selectively illuminate only the cell periphery, the cytoplasmic membrane. The nanopatterning system was used to selectively illuminate the cytoplasmic membrane of the cell in order to study the membrane illumination sensitivity characteristics and response to UVA light. The temperature inside the chamber was maintained at $37^{o}$C and the blood gas mixture was supplied to the cells at a flow rate of 1200±10 cc/minute. No dyes were added to the defined medium for these experiments because the sole effect of UVA light on the cytoplasmic membrane morphology and motion was desired to be studied. By excluding the dyes in the medium, no adverse effects of the dyes would be caused to the cell.

### *4.3.1 Results*

Several experiments were performed where only the cytoplasmic membrane was illuminated with UVA light of intensity 3.65mW/cm$^2$ and the cell response to this was

studied. Figure 4.10 shows a series of images of one experimental cell, the digital mask used to pattern its membrane, and images of the cell at 7min, 12 min and 27 min into the experiment.

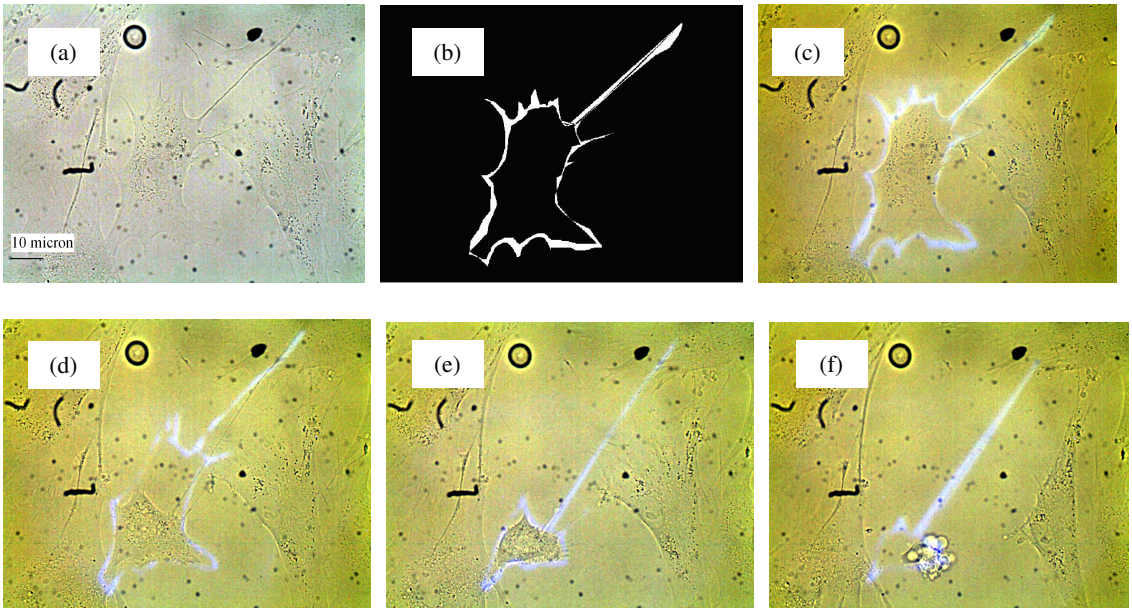


Figure 4.10: Demonstration of local UVA illumination of the cytoplasmic membrane. Figure (a) shows a brightfield image of the cells captured at 60X magnification, was modified by performing 'Autolevels' in Adobe Photoshop for better visualization. Figure (b) shows digital mask projected from the DMD screen, resized to the capture window dimensions. The mask is seen to specifically illuminate the cytoplasmic membrane. Figure (c) shows the cells in the brightfield mode with the overlaying locally illuminated cytoplasmic membrane pattern. Figures (d), (e), and (f) are images captured at 7min, 12min and 27 min into the experiment respectively. Due to the local cytoplasmic membrane illumination, the cell membrane appears to retract in order to escape the UVA light until the cell is maximally shrunk. The cell is seen to have detached itself from the petri dish surface at 27 min. A new digital mask was made to account for every retraction in the membrane and three different masks and be seen in figures (c), (d) and (e).This experiment was performed at 37$^{o}$C with 5% $CO_2$ at 60X magnification. The defined medium was used as the cell medium, no dyes were administered and UVA intensity =3.65mw/cm$^2$ was used. (Scale bar: 10 micron for all figures)

It is observed that the cell shrinks in response to the specific membrane illumination by as early as 7minutes. Another digital mask was quickly drawn so as to correctly trace the cell membrane's current position and illuminate it. As the cell continued to shrink inwards, new masks were created and projected to respond to its movement. In spite of the decrease in the size of the cell and an inward pull within the

cells periphery, it can be observed that the filopodium, a long extension of the cell, still maintained its connection to an adjacent cell. By 27minutes, the cell had reached a minimum size and further illumination of the membrane resulted in the cell detaching from the petri dish surface. The cell was then seen to be freely floating around in the cell medium as condensed mass. In some experiments where the cell under experimentation was attached to another cell on one side, a tendency was seen where the cell maintained the connection with the other cell for as long as it could and also showed a definite preferential direction for shriveling from its opposite end. Almost all cells exhibited a non-uniform motion of the membrane.

To be able to assess the membrane behavior, the membrane velocity for few cells was calculated. The distance that the cell membrane moved between every two time intervals was found by counting the number of pixels in the image and multiplying it by the resolution. This distance divided by the time over which the cell was displaced to obtain the velocity of the cell membrane in response to UVA irradiation. Figure 4.11 shows a scatter plot of the membrane velocity between every time interval for five cells.

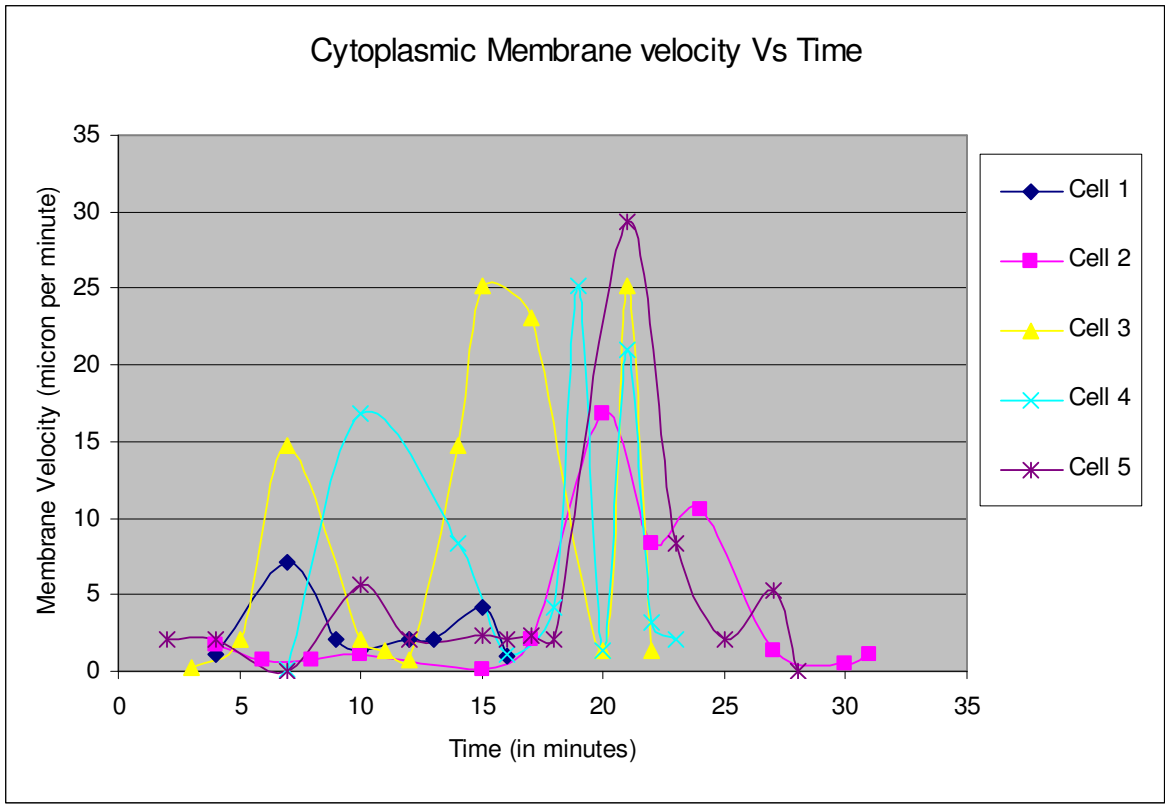


Figure 4.11: Scatter plot of cytoplasmic membrane velocity distribution Vs time for five experimental cells. In presence of UV light with intensity 3.65mW/cm$^2$, the retraction velocity for the cytoplasmic membrane was observed to be about 2.63 to 9.35 µm/min with bursts of high values like 29.4 µm/min.

From the figure, it is seen that no membrane moves at a constant velocity. Sometimes, the velocity is observed to be as high as 29.4 µm/min. This is attributed to a sudden shrinkage in the cell or a sudden release after an accumulation of forces on the membrane. One cell (Cell 1) in the plot shows very little movement and also died the fastest so it may have been unhealthy from the start or had a very small area. The range of average membrane velocity for all cells was calculated to be 2.63 to 9.35 µm/min for a membrane illumination at intensity of 3.65mW/cm$^2$.

*4.3.2 Discussion*

Local illumination of cytoplasmic membranes shows that membranes are affected by UVA light and respond to the UVA induced damage. The cell response to local membrane illumination is cell shrinkage, rounding up and retraction inwards with a varying retraction velocity. A filopodium retraction velocity of about 10 µm/min with bursts of maximum activity up to 25 µm/min has been observed [94]. In presence of UVA light with intensity 3.65mW/cm$^2$, similar values for the retraction velocity for the filopodium and the cytoplasmic membrane were observed, about 2.63 to 9.35 µm/min with bursts of high values like 29.4 µm/min. It had been established that UVA radiation of the cytoplasmic membrane results in generation of reactive oxygen species and this oxidative damage is responsible for membrane damage and cell death [68, 88-90, 95]. Several active oxygen species like singlet oxygen [88, 95], ferrous iron [88] are involved in lipid peroxidation of the membrane. UVA radiation of the cell membrane is also known to change its rigidity and fluidity [89-90]. Beer et al. [87] have previously demonstrated that UVA radiation causes loss of integrity and permealization in the cell membrane and that chromophores absorbing UVA light are present in the membrane along with the cytoplasm. The cytoplasmic membrane as well as the organelles and the cytoplasm are thus definite targets for UVA induced damage [87].

## 4.4 Light directed cell motion studies and optical 'trap' experiments

There are several applications of the nanopatterning system in studies where cells need to be targeted partially. Cell movement can be selectively directed by illuminating a

small portion of the cell such that the cell senses this light and moves away without significant damage caused to the rest of the cell. Optical traps can be laid and cells can be coaxed to enter these by the use of very high intensity light to push them. Such experiments with precise control over the light projection can result in successful manipulation of the cell morphology and the direction of its movement.

Experiments involving targeting UVA light on partial cells were undertaken to investigate cell behavior to damage induced in one portion of its body. In one of the cell experiments conducted to investigate light incidence on a small cell portion, the digital mask projected from the DMD screen was drawn such that only one arm (filopodium) of a cell was illuminated with ultraviolet light. It was observed that at high UVA intensity, the cell seemed to retract from the area of illumination. However, cells having a long filopodium under illumination were observed to actually separate the rest of their body from the filopodium. Consequently, the cell rescued itself from the damaging UVA light at the expense of losing a part of its body, thus demonstrating light dependent movement and contraction. Figure 4.12 shows images taken at 14min, 18min and 20min from an experiment. In this experiment, the UVA pattern was drawn to illuminate a boundary outside the cell and one filopodium was completely illuminated.

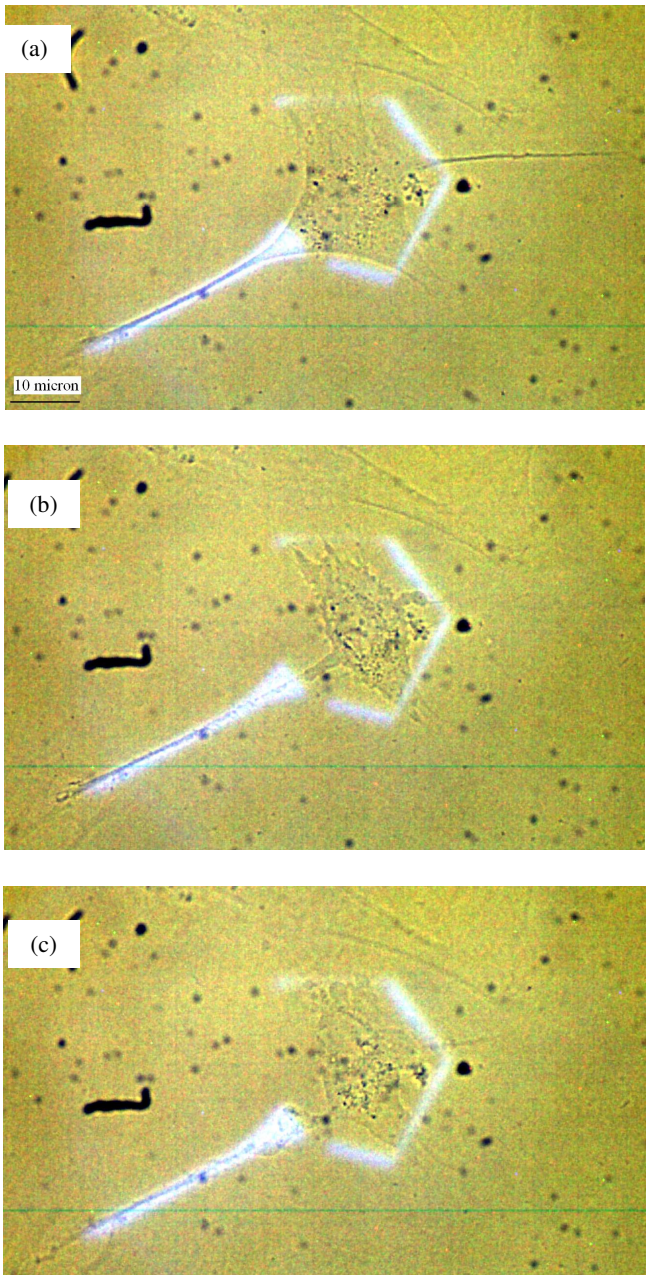


Figure 4.12: Images from a partial cell illumination experiment where a filopodium under UVA illumination was spliced off from the cell body. Figure (a) shows a brightfield image of the cells captured at 60X magnification, was modified by performing 'Autolevels' in Adobe Photoshop for better visualization. Also seen is the digital mask projected from the DMD screen, resized to the capture window dimensions. The mask is a hexagonal structure enveloping the cell perimeter and illuminates one of the cell filopodia (left) completely. This figure was taken at 14min of illumination. Figure (b) shows an image taken at 18min shows the cell responding to the UVA envelope around it by pulling its entire body with one filopodium inside the envelope. The left filopodium which is completely illuminated does not retract inside the UVA envelope and is spliced off by the cell as seen in figure (c). This experiment was performed at 37$^{o}$C with 5% $CO_2$ at 60X magnification. The defined medium was used as the cell medium, no dyes were administered and UVA intensity =3.65mw/cm$^2$ was used. (Scale bar: 10 micron for all figures)

As seen in the figure 4.12 (b), initially the cell retracts its filopodium (seen on the right side) and other tiny extensions inside the UVA boundary. The filopodium which was totally irradiated with the UVA light however is 'cut-off' from the cell at a point and the rest of the cell is contained within the hexagonal UVA boundary. (Figure 4.12(c))

Several optical trap experiments also were performed where blocks of UVA light acting as 'cell traps' were drawn around cells so that the UVA activated damage from one side could trap cells and influence the direction of their motility. The property of the fibroblast cells to sense UVA light and respond to this illumination by moving in a definite direction guided by the light, can be used to direct them to injury sites and promoting wound healing [96,97]. Our optical trap experiments involve the use of UVA light without any external reagents or chemicals, to influence such cell motion and therefore can be powerful tools to direct fibroblast cells to wound sites for proliferation and thereby achieve faster wound healing without any effects of chemicals, etc. Current techniques for designing artificial organs like the skin employ artificial grafts and other biomaterials to host fibroblasts or keratinocytes and recreate the normal architecture of the skin. These cells are expected to grow between the damaged skin layer and the artificial skin layer and aid the proliferation of the patient's own dermal cells. Light directed cell motility capabilities can help preferential proliferation of these cells in the most damaged areas of the skin first and may lead to a faster recovery time for the patient [98].

Cells were observed to splice off filopodia from their body and in some cases, other significant body parts in response to their local UVA illumination. Such cell

experiments established that a fibroblast cell is capable of sensing the UVA light illumination on one of its filopodium and splices it off in order to prevent the damage induced in this portion, from endangering its overall viability. Figure 4.13 shows a picture of an experimental cell and the optical light trap is seen in figure 4.13 (a). Seen in figure 4.13 (b) is the light trap overlaying the cell and the two sacrificed portions of the cell's body are seen in outlined in black squares in figure 4.13 (c), which is an image captured at 44min after the start of the experiment.

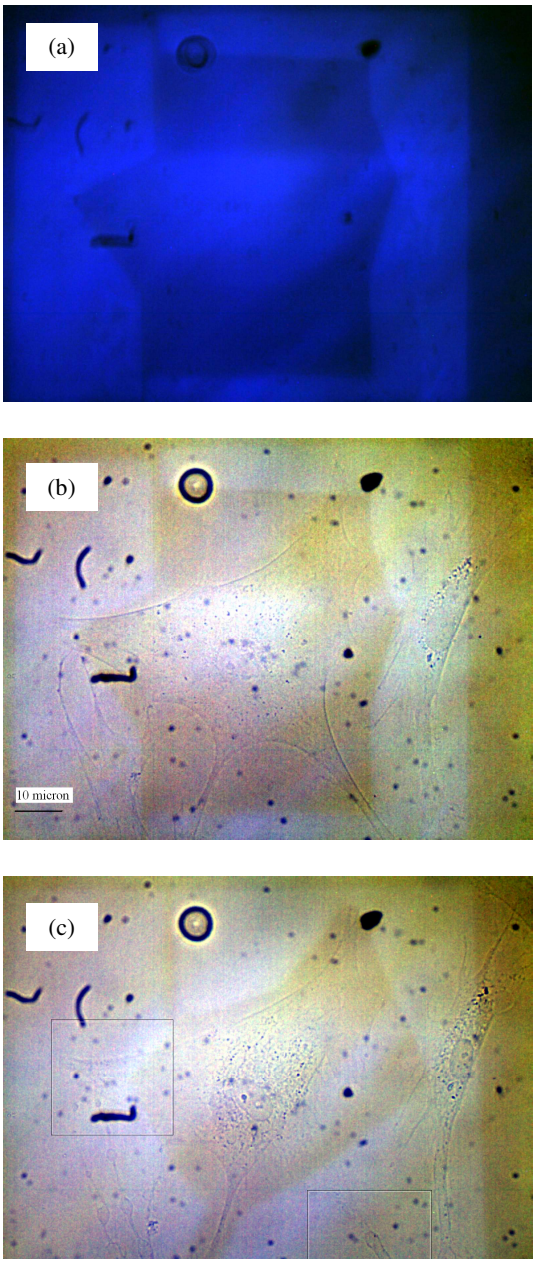


Figure 4.13: Images from a partial cell illumination experiment where portions of cell body were spliced off from the rest of the cell body. Digital mask seen by the camera is seen in figure (a). Figure (b) shows a brightfield image of the cells captured at 60X magnification at 0 min, which was modified by performing 'Autolevels' in Adobe Photoshop for better visualization. Also seen is the digital mask projected from the DMD screen, resized to the capture window dimensions. The mask was originally intended to serve as a light trap for the cell. However, interesting cell behavior was observed when the cell spliced off two parts of its body, which were partially under illumination. Figure (c) shows an image taken after 44min of illumination shows the two spliced portions of the cell in square boxes on the left and the right. The cell appeared to sacrifice those portions of its body which were UV illuminated in order to escape the illumination and survive. This experiment was performed at 37$^{o}$C with 5% $CO_2$ at 60X magnification. The defined medium was used as the cell medium, no dyes were administered and UVA intensity =3.65mw/cm$^2$ was used. (Scale bar: 10 micron for all figures)

In this experiment, the optical trap was drawn so as to trap the cell and manipulate its shape. However, the tip of one of the filopodia of this cell was accidentally illuminated. In response, it was observed that instead of the entire cell retracting itself away from the UVA light, this cell spliced off its one filopodium which was under direct UVA light after 25minutes into the experiment. This portion of the cell was totally detached from the main body of the cell and the cell retracted slightly as though it was experiencing a recoil effect. The cell was still alive and therefore the optical trap experiment was continued. Another interesting splicing effect was observed at 44 minutes when the cell sacrificed another portion of its body that was irradiated and escaped the harmful radiation on the rest of its body, instead of escaping the UVA radiation in its entirety. After splicing off two of its 'arms', the cell was still alive. Clearly, the cell's inherent property is to prevent damage induced in any part of its body from affecting its function and survival, by splicing off all the existing injury sites from its body. These experiments demonstrate that the human fibroblast cells can sense high intensity UVA radiation incident even on a small area of their body and respond to these optical signals either by retraction, splicing of body parts or a change in their orientation. Figure 4.14 is another illustration of an optical trap experiment. It shows the cell, the light trap used and an image of the light trap overlaying the cell. A small portion of the cell on the left side was illuminated with UVA light such that the cell would move towards the right. On the right side of the cell is seen the UVA block serving as the optical trap.

Attempts were also made at altering the cell size and shape so as to condense the cell into a desired shape by splicing off all its arms. These studies are still in their initial

stage and require more experiments to understand the cell behavior in response to local illumination of a portion of the cell.

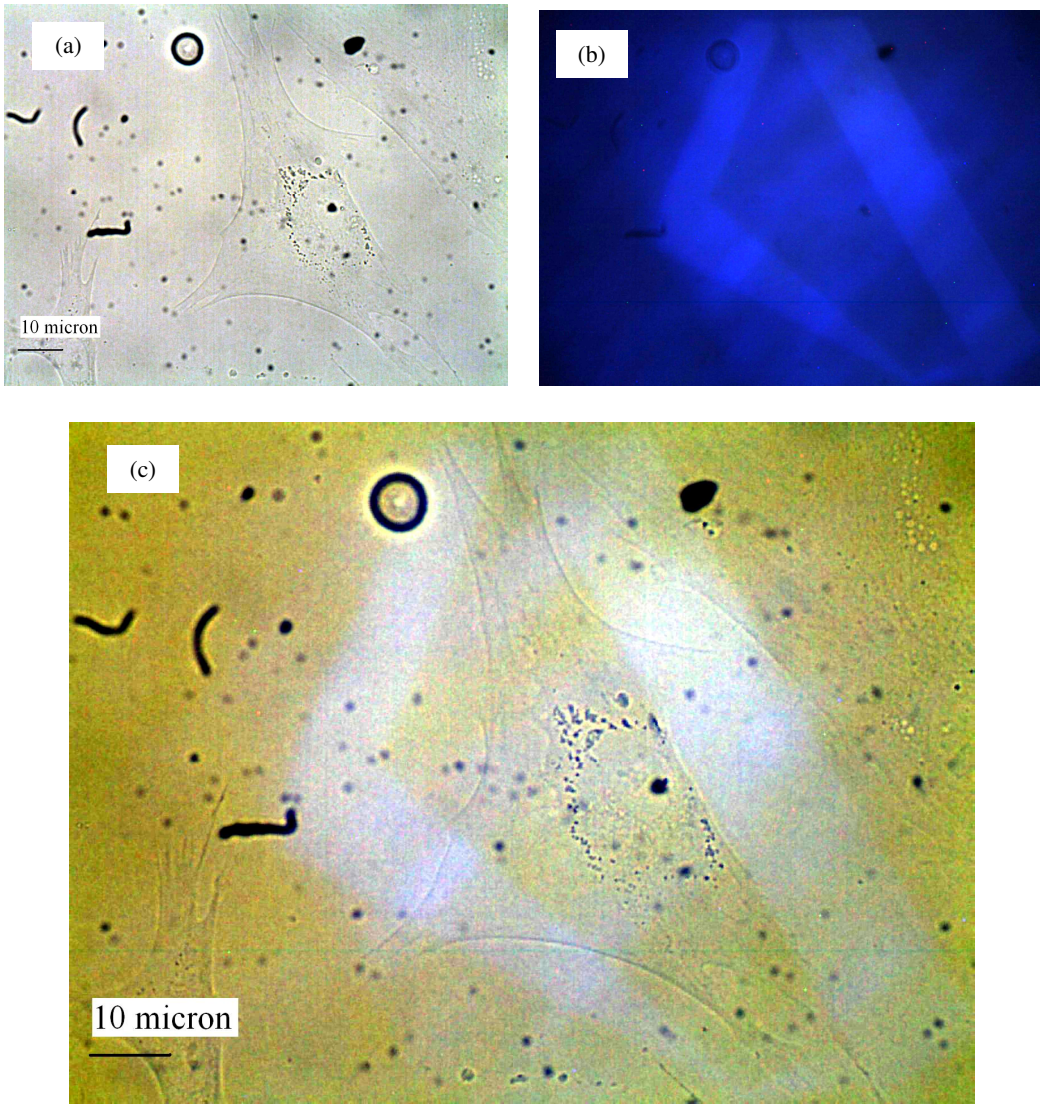


Figure 4.14: Images from a optical cell trap experiment showing the blocks of UVA light drawn to trap the cell. Figure (a) shows a brightfield image of the cells captured at 60X magnification at 0 min, which was modified by performing 'Autolevels' in Adobe Photoshop for better visualization. Also seen in figure (b) is the digital mask projected from the DMD screen, resized to the capture window dimensions. The mask was as a light trap for the cell. Figure (c) shows an image of the cell with the light trap. A small portion of the cell on the left side is illuminated with UVA light such that the cell would move towards the right. On the right side of the cell is seen the UVA block serving as the optical trap. This experiment was performed at 37$^{o}$C with 5% $CO_2$ at 60X magnification. The defined medium was used as the cell medium, no dyes were administered and UVA intensity =3.65mw/cm$^2$ was used. (Scale bar: 10 micron for all figures)

# CHAPTER 5

# CONCLUSIONS AND FUTURE WORK

A nanopatterning system was constructed with the goal of enabling submicron perturbation of biological materials in their optimum environmental conditions. The use of the DMD for precise light targeting coupled with the incorporation of a microscope in the body of the system to access the nanoscale manipulation capabilities is the most unique feature of the nanopatterning system. This instrument also offers temperature and humidity control of the samples which is not only suitable for live cell imaging but can also be useful when working with other biomolecules that require specific environmental conditions for their stability. Once the system was engineered, its parameters were studied and various experiments were undertaken to optimize its performance.

In order to evaluate the system performance and successfully demonstrate its organelle manipulation abilities, subcellular components such as the nucleus, cytoplasm and the cytoplasmic membrane were locally illuminated. Various cell survival data was obtained and it was concluded that the cell cytoplasm is about three times more sensitive to UVA radiation than is the cell nucleus. Several experiments enabling local cytoplasmic membrane illumination yield interesting observations and results about the inward membrane retraction as the membrane's response to high intensity UVA light. Several partial cell manipulation experiments too, were performed and these presented

very promising results. Cells were observed to make an attempt to escape the UVA illumination by splicing off portions of their bodies in order to survive. Various 'cell trap' experiments are on their way where attempts are being made to lay optical traps for cells and cause them to orient themselves relative to the light trap. These results clearly demonstrate the cell's ability to move, change its shape, size and orientation, and perform subcellular operations with an aim to survive, in response to UVA light.

The nanopatterning system currently relies on the capture of images by a user at regular intervals and also requires a manual update of the target's position in order to manipulate it using light. Complete automation of the nanopatterning system can enable rapid switching of patterns and filter cubes, and can improve the system performance by granting a subsecond time resolution to all experiments. The system throughput can also be improved by use of quartz optical components in the optical pathway.

The results obtained using the nanopatterning system can open up new opportunities to study cell behaviour for tissue engineering purposes and for mimicking design of artificial organs. The nanopatterning system can be influential for several partial cell studies where it is desired to investigate only specific cell portions and study the cell response. For example, it can project light patterns on cells to illuminate ion channels that get turned on and off in response to light pulses. This can create a 'light switch' and perhaps grant an optical control over the cell's ion concentration. It can be used to study the primary cellular targets of light activated drugs and reagents, and to deliver photoactivable drugs to specific nanoscale targets. The automated nanopatterning system can be instrumental in many biomedical research areas, for

example, in directing fibroblast cells to injury sites to promote rapid wound healing. Velocities of cell motion can be controlled by changing the UVA illumination intensities used. With a resolution as high as 0.45micron, the nanopatterning system has many potential applications in biology and medicine.

REFERENCES


**(1)** F. Rosso, A. Giordano, M. Barbarisi and A. Barbarisi, "From Cell-ECM interactions to tissue engineering," *Journal of Cellular Physiology* **199,** 174-180 (2004).

**(2)** P. Friedl and E. B. Brocker, "The biology of cell locomotion within three-dimensional extracellular matrix," *Cellular and Molecular Life Sciences* **57,** 41-64 (2000).

**(3)** R. Langer, "Tissue Engineering: Status and Challenges," *e-biomed: The Journal of Regenerative Medicine* **1(1),** 5-6 (2000).

**(4)** R. Langer and J. P. Vacanti, "Tissue Engineering," *Science* **260,** 920-926 (1993).

**(5)** E. E. Hui, and S. N. Bhatia, "Micromechanical control of cell-cell interactions," *Proceedings of the National Academy of Sciences* **104(14),** 5722-2726 (2007).

**(6)** J. E. Trosko, C. C. Chang and B. V. Madhukar, "Modulation and Intercellular Communication during Radiation and Chemical Carcinogenesis," *Radiation Research* **123,** 241-251 (1990).

**(7)** http://en.wikipedia.org/wiki/Cell_signaling

**(8)** J. Seiffer, A. Ratner and D. Sloane, "Concepts in medical physiology," Book pp24-25.

**(9)** P. DeCamilli and M. A. DeMatteis, "Membranes and organelles," *Current Opinion in Cell Biology* **18,** 349-350 (2006).

**(10)** P. A. Conrad, E. J. Smart, Y Ying, R. G. W. Anderson and G. S. Bloom, "Caveolin cycles between plasma membrane caveolae and the golgi complex by microtubule-dependent and microtubule-independent steps," *The Journal of Cell Biology* **131(6-1),** 1421-1433 (1995).

**(11)** M. T. Ryan and N. J. Hoogenraad, "Mitochondrial-Nuclear Communications," *Annual Review of Biochemistry* **76,** 701-722 (2007).

**(12)** T. Levine and C. Loewen, "Inter-organelle membrane contact sites: through a glass, darkly," *Current Opinion in Cell Biology* **18,** 371-378 (2006).

**(13)** http://en.wikipedia.org/wiki/Cell_biology

**(14)** http://en.wikibooks.org/wiki/Biology_Cell_biology_Introduction_Cell_size

**(15)** J. M. Tager, "Inborn Errors of Cellular Organelles: an Overview," *Journal of Inherited Metabolic Disease* **10,** 3-10 (1987).

**(16)** Y. Yamada, H. Akita, K. Kogure, H. Kamiya and H. Harashima, "Mitochondrial drug delivery and mitochondrial disease therapy – An approach to liposome-based delivery targeted to mitochondria," *Mitochondrion* **7(1-2),** 63-71 (2007).

**(17)** M. L. Hans and M. L. Lowman, "Biodegradable nanoparticles for drug delivery and targeting," *Current Opinion in Solid State and Materials Science* **6,** 319-327 (2002).
**(18)** R. Savic, L. Lou, A. Edisenberg, and D. Maysinger, "Micellar Nanocontainers Distribute to Defined Cytoplasmic Organelles," *Science* **300**, 615-618 (2003).
**(19)** http://www.cancer.gov/cancertopics/factsheet/Sites-Types/general
**(20)**http://scienceandresearch.homeoffice.gov.uk/animal-research/publications-and-reference/001-abstracts/abstracts2-2007/12jan-2007/52-07?view=Html
**(21)** G. Srinivasa, T. Merryman, A. Chebira, J. Kovacevic and A. Mintos, "Adaptive Multiresolution techniques for subcellular protein location classification," presented at *IEEE International Conference on Acoustics, Speech and Signal Processing* **5,** V1177-V1180 (2006).
**(22)** E. S. Boyden, F. Zhang, E. Bamberg, G. Nagel and K. Deisseroth, "Millisecond-timescale, genetically-targeted optical control of neural activity," *Nature Neuroscience* **8(9),** 1263-1268 (2005).
**(23)**F. Zhang, L. P. Wang, M. Brauner, J. F. Liewald, K. Kay, N. Watzke, P. G. Wood, E. Bamberg, G. Nagel, A. Gottschalk and K. Deisseroth, "Multimodal fast optical interrogation of neural circuitry," *Nature* **446(7136),** 617-619 (2007).
**(24)** S. Naruse, R. Yatani, and S. Takeda, "Morphological Changes following Ultraviolet Microbeam Irradiation of Parts of Nuclei of Living Cells," *Radiation Research* **32,** 849-860 (1967).
**(25)** T. Cremer, C. Cremer, T. Schneider, H. Baumann, L. Hens and M. Kirsch-Volders, "Analysis of Chromosome Positions in the Interphase nucleus of Chinese Hamster Cells by Laser-UV-Microirradiation Experiments," *Human Genetics* **62,** 201-209 (1982).
**(26)**S. Katsumi, N. Kobayashi, K. Imoto, A. Nakagawa, Y. Yamashina, T. Muramatsu, T. Shirai, S. Miyagawa, S. Sugiura, F. Hanaoka, T. Matsunaga, O. Nikaido, and T. Mori, "In Situ Visualization of Ultraviolet-Light-Induced DNA Damage Repair in Locally Irradiated Human Fibroblasts," *Journal of Investigative Dermatology* **117,** 1156-1161 (2001).
**(27)** V. Vogel and M. Sheetz, "Local force and geometry sensing regulate cell functions," *Nature Reviews Molecular Cell Biology* **7,** 265-275 (2006).
**(28)** A. Revzin, R. G. Tompkins, and M. Toner, "Surface Engineering with Poly(ethylene glycol) Photolithography to Create High-Density Cell Arrays On Glass," *Langmuir* **19,** 9855-9862 (2003).
**(29)** P. K. Chu, J. Y. Chen, L. P. Wang and N. Huang, "Plasma-surface modification of biomaterials," *Materials Science and Engineering* **R 36,** 143–206 (2002).
**(30)** E. A. Roth, T. Xu, M. Das, C. Gregory, J. J. Hickman, T. Boland, "Inkjet printing for high-throughput cell patterning," *Biomaterials* **25,** 3707-3715 (2004).
**(31)** M. J. Dalby, M. O. Riehle1, D. S. Sutherland, H. Agheli and A. S. G. Curtis, "Morphological and microarray analysis of human fibroblasts Cultured on

nanocolumns produced by colloidal lithography," *European Cells and Materials* **9,** 1-8 (2005).

**(32)** N. E. Sanjana, and S. B, Fuller, "A fast flexible ink-jet printing method for patterning dissociated neurons in culture," *Journal of Neuroscience Methods* **136,** 151-163 (2004).

**(33)** S. B. Fuller, E. J. Wilhelm and J. M. Jacobson, "Ink-Jet Printed Nanoparticle Microelectromechanical Systems," *Journal of Microelectromechanical Systems* **11(1),** 54-60 (2002).

**(34)** L. Pardo, W. C. Wilson Jr., and T. Boland, "Characterization of Patterned Self-Assembled Monolayers and Protein Arrays Generated by the Ink-Jet Method," *Langmuir* **19,** 1462-1466 (2003).

**(35)** K. J. Luebke, D. E. Carter, H. R. Garner, and K. C. Brown, "Patterning adhesion of mammalian cells with visible light, tris(bipyridyl)ruthenium(II) chloride, and a digital micromirror array," *Journal of Biomedical Materials Research* **68A,** 696–703 (2004).

**(36)** H. Baac, J. Lee, J. Seo, T. H. Park, H. Chung, S. Lee, S. J. Kim, "Submicron-scale topographical control of cell growth using holographic surface relief grating," *Materials Science and Engineering C* **24,** 209–212 (2004).

**(37)** T. Gabay, E. Jakobs, E. Ben-Jacob and Y. Hanein, "Engineered self-organization of neural networks using carbon nanotube clusters," *Physica A: Statistical Mechanics and its Applications* **350(2-4),** 611-621 (2005).

**(38)** S. N. Bhatia, M. L. Yarmush and M. Toner, "Controlling cell interactions by micropatterning in co-cultures: Hepatocytes and 3T3 fibroblasts," *Journal of Biomedical Materials Research* **34,** 189–199 (1997).

**(39)** W. He, C. R. Halberstadt, and K. E. Gonsalves, "Lithography application of a novel photoresist for patterning of cells," *Biomaterials* **25,** 2055-2063 (2004).

**(40)** R. King, "Gene Delivery to Mammalian Cells by Microinjection," *Methods in Molecular Biology* **245,** 167-174 (2004).

**(41)** J. P. Desai, A. Pillarisetti and A. D. Brooks, "Engineering Approaches to Biomanipulation," *Annual Review of Biomedical* Engineering **9,** 35–53 (2007).

**(42)** http://en.wikipedia.org/wiki/microinjection

**(43)** C. M. Green and G. Almouzni, "Local action of the chromatin assembly factor CAF-1 at sites of nucleotide excision repair in vivo," *The EMBO Journal* **22(19),** 5163-5174 (2003).

**(44)** T. Muller, A. Pfennig, P. Klein, G. Gradl, M. Jager, and T. Schnelle, "The Potential of Dielectrophoresis for Single-Cell Experiments," *IEEE engineering in medicine and biology magazine* November/December 51-61 (2003).

**(45)** C. Ho, R. Lin, W. Chang, H. Chang and C. Liu, "Rapid heterogeneous liver-cell on-chip patterning *via* the enhanced field-induced dielectrophoresis trap," *Lab Chip* **6**, 724-7

**(46)** S. Prasad, M. Yang, X. Zhang, C. S. Oskan, and M. Oskan, "Electric field assisted patterning of neuronal networks for the study of brain functions," *Biomedical Microdevices* **5(2),** 125-137 (2003).

**(47)** J. A. Lundquist, F. Sahlin, M. A. I. Aberg, A. Stromberg, P. s. Eriksson, and O. Orwar, "Altering the biochemical state of individual cultured cells and organelles with ultramicroelectrodes," *Proceedings of National Academy of Science USA* **95,** 10356-10360 (1998).

**(48)** C. Yi, C. Li, S. Ji and M. Yang, "Microfluidics technology for manipulation and analysis of biological cells," *Analytica Chimica Acta* **560(1-2),** 1-23 (2006).

**(49)** A. Hultgren, M. Tanase, C. S. Chen, G. J. Meyer and D. H. Reich, "Cell manipulation using magnetic nanowires," *Journal of Applied Physics* **93(10)**, 7554-7556 (2003).

**(50)** C. Wilhelm, F. Gazeau and J.C. Bacri, "Magnetic micromanipulation in the living cell," *Europhysics News* **33,** 89–92 (2005).

**(51)** M. Boukallel, E. Piat and J. Abadie, "Micromanipulation tasks using passive levitated force sensing manipulator," presented at *Proceedings of the 2003 IEE/RSJ International Conference on Intelligent Robots and Systems* **1,** 529–34 (2003).

**(52)** P. O'B. Montgomery, J. E. Cook and D. Karney, "Ultraviolet Microbeam Irradiation in living cell membranes," *The Journal of Cell Biology* **26(3),** 959-961 (1965).

**(53)** R. B. Uretz and R. P. Perry, "Improved Ultraviolet Microbeam Apparatus," *Review of Scientific Instruments* **28,** 861-866 (1957).

**(54)** R. E. Zirkle, "Ultraviolet-Microbeam Irradiation of Newt-Cell Cytoplasm: Spindle Destruction, False Anaphase, and Delay of True Anaphase[1]," *Radiation Research* **41**, 516-537 (1970).

**(55)** C. Cremer, T. Cremer, C. Zorn, and L. Schoettlltf, "Effects of laser UV-microirradiation (λ=2573 A) on proliferation of chinese hamster cells," *Radiation Research* **66,** 106-121 (1976).

**(56)** T. R. Munro, "The Relative Radiosensitivity of the Nucleus and Cytoplasm of Chinese Hamster Fibroblasts," *Radiation Research* **42,** 451-470 (1970).

**(57)** L. Wu, G. Randers-Pehrson, A. Xu, C. A. Waldren, C. R. Geard, Z. Yu, and T. K. Hei, "Targeted cytoplasmic irradiation with alpha particles induces mutations in mammalian cells," *Proceedings of National Academy of Science USA* **96**, 4959–4964 (1999).

**(58)** H. Liang, T. Do, S. Kasravi, P. Aurasteh, A. Nguyen, A. Huang, Z. Wang and M. W. Berns, "Chromosomes are target sites for photodynamic therapy as demonstrated by subcellular laser microirradiation," *Journal of Photochemistry and Photobiology B: Biology* **54(2-3),** 175-184 (2000).

**(59)** M. J. Mone, M. Volker, O. Nikaido, L. H. F. Mullenders, A. A. van Zeeland, P. J. Verschure, E. M. M. Manders & R van Driel, "Local UV-induced DNA damage in cell nuclei results in local transcription inhibition," *EMBO reports* **2(11),** 1013–1017 (2001).

**(60)** D. I. Pattison and M. J. Davies, "Actions of ultraviolet light on cellular structures," in *Cancer: Cell structures, Carcinogens and Genomic Instability* 131-157 (2006).

**(61)** D. E. Godar, "UVA1 radiation triggers two different final apoptotic pathways," *Journal of Investigative Dermatology* **112,** 3–12 (1999).
**(62)** http://en.wikipedia.org/wiki/photodynamictherapy
**(63)** http://en.wikipedia.org/wiki/PUVA
**(64)** G. M. Halliday and S. Rana, "Waveband and Dose Dependency of Sunlight-Induced Immunomodulation and Cellular Changes," *Photochemistry and Photobiology* **84,** 35-46 (2008).
**(65)** A. R. Young, "Chromophores in human skin," *Physics in Medicine and Biology* **42,** 789-802 (1997).
**(66)** A. Sesto, M. Navarro, F. Burslem and J. L. Jorcano, "Analysis of the ultraviolet B response in primary human keratinocytes using oligonucleotide microarrays," *Proceedings of National Academy of Science USA* **99(5),** 2965-2970 (2002).
**(67)** A. Moysan, I. Marquis, F. Gaboriau, R. Santus, L. Dubertret and P. Morlière, "Ultraviolet A – Induced Lipid Peroxidation and Antioxidant Defense Systems in Cultured Human Skin Fibroblasts," *Journal of Investigative Dermatology* **100**, 692–698 (1993).
**(68)** A. W. Girotti, "Photosensitized oxidation of membrane lipids: reaction pathways, cytotoxic effects, and cytoprotective mechanisms," *Journal of photochemistry and photobiology B: Biology* **63,** 103-113 (2001).
**(69)** R. M. Tyrrell, C. A. Pourzand, J. Brown, V. Hejmadi, E. Kvam, S. Ryter and R. D. Watkin, "Cellular Studies With UVA Radiation: A Role For Iron," *Radiation Protection Dosimetry* **91(1–3),** 37–39 (2000).
**(70)** M. A. Bachelor and G. T. Bowden. "UVA-mediated activation of signaling pathways involved in skin tumor promotion and progression," *Seminars in Cancer Biology* **14(2),** 131-138 (2004).
**(71)** D. E. Godar, S. A. Miller and D. P. Thomas, "Immediate and delayed apoptotic cell death mechanisms: UVA versus UVB and UVC radiation," *Cell Death Differentiation.* **1(1),** 59-66 (1994).
**(72)** G. S. Trindade, M. A. M. Capella, L. S. Capella, O. R. Affonso-Mitidieri and V. M. Rumjanek, "Differences in sensitivity to UVC, UVB and UVA radiation of a multidrug-resistant cell line overexpressing P-glycoprotein," *Photochemistry and Photobiology* **69(6),** 694-699 (1999).
**(73)** http://www.epa.gov/sunwise/uvandhealth.html#cat
**(74)** http://en.wikipedia.org/wiki/Ultraviolet
**(75)** E. Mirowski, J. Moreland, A. Zhang, S. E. Russek and M. J. Donahue, "Manipulation and sorting of magnetic particles by a magnetic force microscope on a microfluidic magnetic trap platform," *Applied Physics Letters* **86,** 243901-243903 (2005).
**(76)** L. J. Hornbeck, "Digital Light ProcessingTM for High-Brightness, High-Resolution Applications," in *Electronic Imaging, EI '97,Projection Displays III.* Feb. 10-12, 1997, San Jose, CA.
**(77)** L. J. Hornbeck, "Digital Light Processing™: A New MEMS-Based Display Technology," *Technical Digest of the IEEJ 14th Sensor Symposium* **6,** 297-304 (1996).

**(78)** M. L. Huebschman, B. Munjuluri and H. R. Garner, "Dynamic holographic 3-D image projection," *Optics Express* **11(5),** 437-445 (2003).
**(79)** N. Marthandan, S. Klyza, L. Shuwei, K. Yong-Uk, T. Kodadek and H. R. Garner, **"**Construction and Evaluation of an Automated Light Directed Protein-Detecting Microarray Synthesizer," *IEEE Transactions on NanoBioscience* **7(1),** 20 – 27 (2008).
**(80)** Motic 2000 camera manual and datasheet
**(81)** K. Luby-Phelps, D. L. Taylor and F. Lanni, "Probing the structure of cytoplasm," *The Journal of cell biology* **102,** 2015-2022 (1986).
**(82)** G. B. Zamansky and I. Chou, "Environmental wavelengths of ultraviolet light induce cytoskeletal damage," *The Journal of Investigative Dermatology* **89(6),** 603-606 (1987).
**(83)** http://heliocare.com/picture.htm
**(84)** W. Malorni, G. Donelli, E. Straface, M. T. Santini, S. Paradisi, P. U. Giacomoni, "Both UVA and UVB induce cytoskeleton-dependent surface blebbing in epidermoid cells," *Journal of photochemistry and photobiology B: Biology* **26(3),** 265-270 (1994).
**(85)** P. U. Giacomoni, J. F. Nadaud, E. Straface, G. Donelli, M. Heenen and W. Malorni, "Morphological alterations and cell blebbing in UV-irradiated human epidermis," *Archives of Dermatological Res*earch **290,** 163-166 (1998).
**(86)**Z. Somosy, "Radiation response of cell organelles," *Micron* **31,** 165-181 (2000).
**(87)** J. Z. Beer, K. M. Olvey, S. A. Miller, D. P. Thomas and D. E. Godar, "Non-nuclear damage and cell lysis are induced by UVA, but not by UVB or UVC, radiation in three strains of L5178Y cells," *Photochemistry and Photobiology* **58(5),** 676-681 (1993).
**(88)** G. F. Vile and R. M. Tyrrell, "UVA radiation-induced oxidative damage to lipids and proteins in vitro and in human skin fibroblasts is dependent on iron and singlet oxygen," *Free Radical Biology and Medicine* **18(4),** 721-730 (1995).
**(89)** Y. Ibuki, A. Suzuki and R. Goto, "UVA Irradiation Induces Energy-independent Phospholipid-flip in Mammalian Plasma Membrane," *Photochemistry and Photobiology* **73(5),** 513-517 (2001).
**(90)** F. Gaboriau, P. Morliere, I. Marquis, A. Moysan, M. Goegze and L. Dubertret, "Membrane damage induced in cultured human skin fibroblasts by UVA irradiation," *Photochemistry and Photobiology* **58(4),** 515-520 (1993).
**(91)** W. Wamer and R. R. Wei, "*In vitro* Photooxidation of Nucleic Acids by Ultraviolet A radiation," *Photochemistry and Photobiology* **65(3),** 560-563 (1997).
**(92)** E. Fritsche, C. Schafer, C. Calles, T. Bernsmann, T. Bernshausen, M. Wurm, U. Hubenthal, J. E. Cline, H. Hajimiragha, P. Schroeder, L. Klotz, A. Rannug, P. Furst, H. Hanenberg, J. Abel and J. Krutmann, "Lightening up the UV response by identification of the arylhydrocarbon receptor as a cytoplasmic target for ultraviolet B radiation," *Proceedings of National Academy of Science USA* **104(21),** 8851-8856 (2007).

**(93)** D. Kulms, B. Poppelmann, D. Yarosh, T. A. Luger, J. Krutmann and T. Schwarz, "Nuclear and cell membrane effects contribute independently to the induction of apoptosis in human cells exposed to UVB radiation," *Proceedings of National Academy of Science USA* **96,** 7974-7979 (1999).
**(94)** A. Jacinto and L. Wolpert, "Filopodia," *Current Biology* **11,** R634 (2001).
**(95)** E. Gaboriau, N. Demoulins-Giacco, I. Tirache and R. Morlibre, "Involvement of singlet oxygen in ultraviolet A-induced lipid peroxidation in cultured human skin fibroblasts," *Archives of Dermatological Res*earch **287,** 338-340 (1995).
**(96)** M. G. Lampugnani, "Cell migration into a wounded area in vitro," *Methods in Cell Biology* **96,** 177-182 (1999).
**(97)** E. Khain, L. M. Sander and C. M. Schneider-Mizell, "The role of cell-cell adhesion in wound healing," *Journal of statistical physics* **128(1/2),** 209-218 (2007).
**(98)** P. Shakespeare, "Burn wound healing and skin substitutes," *Burns* **27,** 517-522 (2001).

# BIOGRAPHICAL INFORMATION

Amruta Rajiv Joshi received the B.E. degree in Instrumentation Engineering from University of Mumbai in 2005. She enrolled in the Joint program in Biomedical Engineering between University of Texas at Arlington and University of Texas Southwestern Medical Center at Dallas in Fall 2005 and received her M.S. degree in August 2008. During her graduate degree, she won the First Runner-up award in Poster Presentation at the University level UT Metroplex Day Series of programs for Nanomedicine, Biological Sciences and Engineering. Her current research interests include Tissue Engineering, Bioinstrumentation and Biomedical Optics.